Colloidal Monolayers on Quasiperiodic Laser Fields

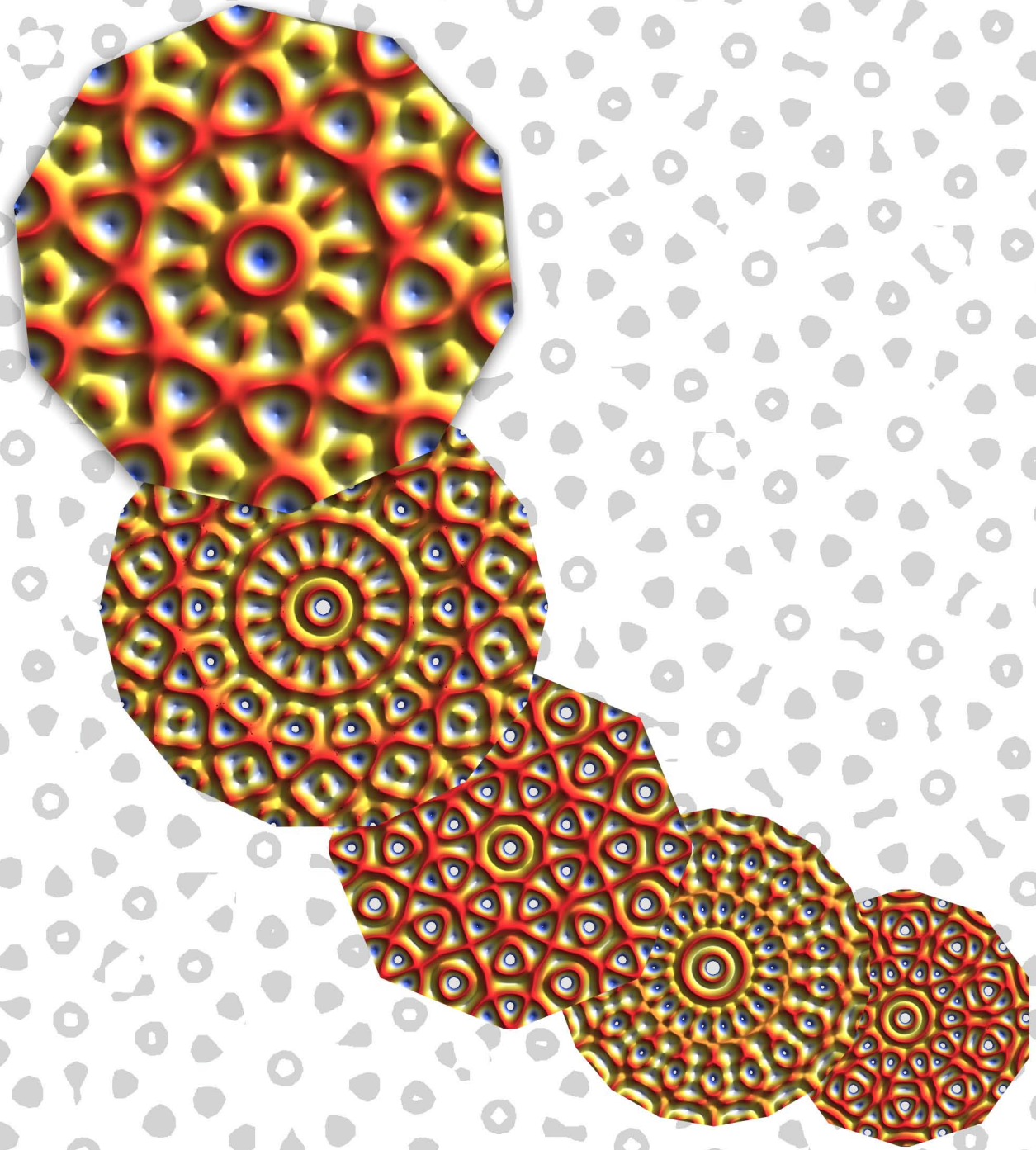

Dissertation

Jules Mikhael

Colloidal Monolayers on Quasiperiodic Laser Fields

Von der Fakultät Mathematik und Physik der Universität Stuttgart
zur Erlangung der Würde eines Doktors der Naturwissenschaften (Dr. rer. nat.)
genehmigte Abhandlung

vorgelegt von

Jules Mikhael
aus Kfarhatna (Libanon)

Hauptberichter: Prof. Dr. Clemens Bechinger
Mitberichter: Prof. Dr. Ulrich Stroth

Tag der mündlichen Prüfung: 08. März 2010

Physikalisches Institut der Universität Stuttgart

2010

CONTENTS

ZUSAMMENFASSUNG

Quasikristalle sind faszinierende und in vielerlei Hinsicht paradoxe Strukturen, die sich durch ungewöhnliche Eigenschaften von gewöhnlichen, periodischen Kristallen unterscheiden. Obwohl sich die Abstände zwischen den Atomen nicht periodisch wiederholen, besitzen Quasikristalle doch eine perfekte Fernordnung. Bis in die frühen 1980er Jahre wurde angenommen, geordnete Materie sei immer periodisch, woraus sich ableiten läßt, dass Rotationssymmetrien im realen Raum auf n = 2,3,4 und 6 beschränkt sind. Heutzutage sind jedoch mehr als hundert komplexe Metall-Legierungen bekannt, die diese kristallographischen Regeln verletzen. Ikosaedrische AlPdMn oder dekagonale AlNiCo Kristalle mit ihren diskreten Beugungsspektren sind prominente Beispiele für Quasikristalle. Die Mehrheit der bekannten Quasikristalle sind komplexe Metall-Legierungen. In neuere Experimenten konnte jedoch gezeigt werden, dass quasiperiodische Ordnung nicht auf Metalllegierungen beschränkt ist. Wie bei Mizellensystemen, Block-copolymeren und sogar Kristallen aus bidispersen Nanopartikeln beobachtet, kann Materie auch auf größeren Längenskalen selbstorganisiert eine quasikristalline Struktur annehmen. Aus der besonderen Struktur resultieren viele interessante makroskopische Eigenschaften, die hohes technologisches Potential z.B. als Oberflächenbeschichtungen, thermische Barrieren, Katalysatoren oder photonische Kristalle bieten. Um dieses Potenzial in Zukunft besser ausnutzen zu können, ist es nötig, die Bedingungen, unter denen sich Quasikristalle bilden, genauer zu untersuchen.

Quasikristalline Strukturen wurden auch in Systemen mit einem einzigen Typ von Teilchen theoretisch vorhergesagt. Ihre spontane Bildung wurde jedoch nur in binären, ternären oder sogar noch komplexeren Legierungen experimentell beobachtet. Dementsprechend zeigen quasikristalline Oberflächen eine hohe strukturelle und chemische Komplexität. Um den Ursprung dieser Merkmale zu verstehen, ist es hilfreich, die strukturellen und chemischen Aspekte zu trennen. Dies kann durch Aufbringen von nur aus einem Element bestehenden Adsorbatschichten auf Quasikristallen erreicht werden. Nur wenige Elemente zeigen dabei pseudomorphes Wachstum, bei dem sich die quasikristalline Symmetrie auf die Adsorbatschicht überträgt. Bei der Heteroepitaxie auf dekagonalen und ikosaedrischen Oberflächen konnten Pb, Sb und

Bi Monoschichten mit einem hohen Maß an quasikristalliner Ordnung hergestellt und durch LEED (low-energy electron diffraction) sowie HAS (elastische Heliumstreuung) nachgewiesen werden. Im Vergleich zu Studien im reziproken Raum, wurden erst vor kurzem atomar aufgelöste Rastertunnelmikroskopie-Untersuchungen der Adsorbate möglich. Selbst damit ist es schwierig, die Struktur des Adsorbats und die Struktur des unterliegenden Substrats miteinander in Bezug zu bringen.

In diesem Zusammenhang kann die hier durchgeführte Studie des Phasenverhaltens von kolloidalen Partikeln unter dem Einfluss von quasiperiodischen Laserfeldern neues Licht auf diese grundlegenden Fragestellungen im Bereich der Quasikristalle und Festkörperphysik werden. Ausgenutzt wird dazu, dass sich Kolloidale Systeme hervorragende Modellsysteme für das Verhalten atomarer Festkörper sind. Die mesoskopische Größe (nm-µm) und die typischen Zeitskalen (ms-s) ermöglichen ferner die videomikroskopische Beobachtung der Systeme und die Verfolgung der einzelnen Trajektorien aller Partikel direkt im Ortsraum. So erhält man deutlich mehr Information über die Entwicklung des Systems als es z.B. in Beugungsexperimenten möglich ist, die über einen größeren Probenbereich mitteln. Die Technik der Videomikroskopie hat sich insbesondere bei der Untersuchung zweidimensionaler Systeme als vorteilhaft erwiesen. Diese können zusätzlich durch optische Pinzetten beeinflusst werden, so dass z.B. eine Monolage kolloidaler Partikel mit einem als Potentiallandschaft wirkenden Lichtgitter wechselwirkt. Das so generierte und in seiner Stärke über die Laserintensität einstellbare Potential kann als Analogie zum Substratpotential einer Festkörperoberfläche betrachtet werden.

In dieser Arbeit wird das Phasenverhalten von geladenen kolloidalen Monolagen, unter dem Einfluss von dekagonalen und tetradekagonalen quasikristallinen Lichtgittern, die durch Interferenz von fünf bzw. sieben Laserstrahlen erzeugt werden, untersucht. Verschiedene Ausgangskonfigurationen, wie z. B. dichte Flüssigkeiten und triangulare Kristalle mit unterschiedlichen Dichten, wurden präpariert. Bei niedrigen Intensitäten des Lichtgitters und hoher Teilchendichte dominiert die elektrostatische Abstoßung der Kolloide untereinander über die Kolloid-Substrat-Wechselwirkungen und die kristalline Struktur bleibt im Wesentlichen intakt. Bei sehr hohen Intensitäten dominieren - wie zu erwarten - die Kolloid-Substrat-Wechselwirkungen und eine quasiperiodische Ordnung wird beobachtet. Der interessante Parameterbereich liegt bei mittleren Laserintensitäten. Hier beobachten wir zunächst die Ausrichtung von kristallinen Bereichen entlang der 5 Richtungen des quasikristallinen Substrates. Dies ist in Übereinstimmung mit Beobachtungen von Xenon-Atomen adsorbiert auf einer dekagonalen Al-Ni-Co-Oberfläche und der numerischen Simulation von schwach adsorbierten atomaren Systemen. Für stärkere Kolloid-Substrat-Wechselwirkungen ergibt sich eine interessante Zwischenphase, bei der Reihen des triangulären Kristalls in Reihen mit quadratischen Kacheln umgewandelt werden. Überraschenderweise, kann diese Phase für bestimmte Teilchendichten (bei denen die Kolloid-Substrat-Wechselwirkungen minimiert sind) mit einer neuartigen pseudomorphen Ordnung identifiziert werden. Diese Zwischenphase, die kristalline und quasikristalline strukturelle Aspekte in sich vereinigt, kann durch eine archimedische Kachelung mit charakteristischen Defekten beschrieben werden. Die berechneten Beugungsmuster die-

ser Phase sind in Übereinstimmung mit den neuesten Beobachtungen von Kupfer adsorbiert auf ikosaedrischen AlPdMn Oberflächen. Interessanterweise haben wir die Bildung einer ähnlichen Phase auch für tetradekagonale Substratpotentiale beobachtet. Auch für diese wird die potentielle Energie des kolloidalen Systems minimiert, indem sich Reihen quadratischer Kacheln bilden. Allerdings sind hier große Gebiete mit nahezu periodischer Anordnung zu finden. Wir zeigen, dass dieses Verhalten in engem Zusammenhang mit der geringen Dichte von hoch symmetrischen lokalen Motiven in dem Substratpotential verbunden ist. Dies kann Hinweise darauf geben, welche atomaren Quasikristalle gebildet werden können.

Im zweiten teil dieser Arbeit wird untersucht unter welchen bedingungen sich Quasikristalle ausbilden. Derzeit ist nicht klar, warum die meisten Quasikristalle 5- oder 10-zählige Symmetrie besitzen, aber kein einziges Beispiel mit 7 oder 9-zähliger Symmetrie beobachtet wurde. Da die Eigenschaften von Quasikristallen stark von ihrer atomaren Struktur abhängen, ist ein besseres Verständnis der Mechanismen unter denen sie wachsen, von großer Bedeutung. Im Gegensatz zu Kristallen, die in allen drei Dimensionen periodisch sind, ist Quasiperiodizität immer (außer ikosaedrischen Quasikristalle) auf zwei Dimensionen beschränkt. Dementsprechend sind diese dreidimensionale Quasikristalle als ein periodischer Stapel von quasiperiodischen Schichten zu verstehen. Jede Hürde bei der Bildung von quasiperiodischer Ordnung innerhalb einer einzelnen Schicht wird schließlich ein Kristallwachstum entlang der periodischen Richtung verbieten. Daher diskutieren wir in dieser Arbeit auch die geometrischen Beschränkung, die die Bildung von Quasikristallen mit bestimmten Symmetrien behindern und verifizieren dies exemplarich durch Experimente mit entsprechenden kolloidalen Modellsystemen. Unsere Ergebnisse zeigen eindeutig, dass sich quasikristalline Ordnung für n = 5 im Vergleich zu n = 7 um vieles leichter auf die nächste Adsorbatebene übertragen lässt. Mit zunehmender Intensität des Substratpotentials beobachten wir, dass die Kolloide die aufgeprägte quasikristalline Ordnung zunächst in lokalen Bereichen annehmen, die durch hochsymmetrische Motive des Substrats gegeben sind, und dass diese Bereiche dann lateral wachsen, bis eine zusammenhängende quasikristalline Schicht entsteht. Die Dichte der hochsymmetrischen Motive variiert stark mit der 5,7,8,9,10,11 oder 12-fachen Symmetrie von idealen Quasikristallen und ist gerade für die Quasikristalle, die nie in atomaren Systemen beobachtet wurden, am kleinsten. Es liegt die Vermutung nahe, dass das Fehlen der hochsymmetrischen Motive der Grund für die nicht-Existenz dieser z.B. 7-zähligen Quasikristalle ist.

Schließlich wird ein anwendungsorentierter Aspekt behandelt. Da Quasikristalle höhere Punktsymmetrie besitzen als gewöhnliche Kristalle wird erwartet, dass quasikristalline Materialien isotrope photonische Bandlücken aufweisen und dass diese für kolloidale Quasikristalle im sichtbaren Wellenlängenbereich liegen. Deshalb wurde in dieser Arbeit versucht, ausgedehnte quasiperiodische kolloidale Schichten in eine Polymer-Hydrogel-Matrix einzubetten. Dabei wurden die durch die Laserinterferenzgitter erzeugten kolloidalen Quasikristalle durch UV-induzierte Polymerisation in der Matrix festgehalten. Die so erhaltenen mehrere Millimeter großen Strukturen zeichnen sich durch eine gute optische Homogenität und klare Beugungsmuster aus.

Zudem können wegen der Elastizität der Polymermatrix die Längenskalen auch in situ variiert werden.

INTRODUCTION

Quasicrystals are somewhat paradoxical structures which exhibit many amazing properties distinguishing them from ordinary crystals. Although the atoms are not localized at periodic positions, quasicrystals posses perfect long-range order. Until the early 1980s it was unanimously established that ordered matter is always periodic. Accordingly, the rotational symmetry in real space was thought to be limited to n=2,3,4 and 6. However more than a hundred complex metal alloys, for instance the discretely diffracting icosahedral AlPdMn or decagonal AlNiCo, have defied these crystallographic rules and self-organized into quasicrystals. Although the majority of the identified quasicrystals are complex metal alloys synthesized in the laboratory, recent experimental results proved that quasiperiodic order is not limited to metals. Matter also organizes itself aperiodically at larger length scales where thermal fluctuations play an important role. Recent experiments have shown that quasiperiodic order is also oberved in soft matter systems, such as micellars, polymers, and binary nanoparticles. Quasicrystals show many interesting properties which are quite different from that of periodic crystals. Accordingly, they are considered as materials with high technological potential e.g. as surface coatings, thermal barriers, catalysts or photonic materials.

Quasicrystalline structures have been theoretically predicted also in systems with a single type of particles. Nevertheless, experimentally their spontaneous formation has been only observed in binary, ternary or even more complex alloys. Accordingly, their surfaces exhibit a high degree of structural and chemical complexity and show intriguing properties. In order to understand the origin of those characteristics it would be helpful to disentangle structural and chemical aspects which can be achieved by growing single-element monolayers to quasicrystalline surfaces. Apart from understanding how quasicrystalline properties can be transferred to such monolayers, this approach might allow fabrication of materials with novel properties. First heteroepitatic growth experiments on decagonal and icosahedral surfaces indeed demonstrate the formation of Pb, Bi and Sb monolayers with a high degree of quasicrystalline order as determined by low-energy electron diffraction and elastic helium atom scattering experiments. Compared to reciprocal space studies, only

recently atomically resolved scanning tunneling microscopy investigations of the adsorbate morphology became possible. Even then, however, it is difficult to relate the structure of the adsorbate to that of the underlying substrate.

In that respect, the study of the phase behaviour of colloidal particles interacting with quasiperiodic laser fields can throw new light on fundamental problems of broad interest in the physics of quasicrystals and in condensed matter physics. In fact colloidal systems are meanwhile established as excellent model for atomic systems and colloidal physics have demonstrated that such systems can give answers to many basic physics questions. Depending on the pair-interaction and the concentration, colloidal systems show analogues of all the states of atomic systems: gas, liquid and solid states. The mesoscopic size (nm-μm), the time scales (ms-s) and the tunability of the pair interaction in colloidal systems make them a convenient model system for experimental and theoretical studies. As a consequence, real space analysis by means of video microscopy allows tracking the trajectories of the individual particles and makes the time evolution of the system accessible in detail. Such information is inaccessible in systems investigated by diffraction experiments, as the scattering information is available only averaged over the scattering area. Because in a colloidal system there is direct access to real space information, the strength and nature of the different interactions, the origins of the complex phase behavior could be in different examples identified. In conclusion, the study of the rich phase behavior of colloidal suspensions provides ideal conditions for experimental and theoretical studies.

In this Thesis, we report on a real-space investigation of the phase behaviour of charged colloidal monolayers interacting with quasicrystalline decagonal or tetradecagonal substrates created by interfering five or seven laser beams. Different starting configurations, such as dense fluid and triangular crystals with different densities, are prepared. At low intensities and high particle densities, the electrostatic colloidal repulsion dominates over the colloid-substrate interaction and the crystalline structure remains mainly intact. As expected, at very high intensities the colloid-substrate interaction dominates and a quasiperiodic ordering is observed. Interestingly, at intermediate intensities we observe the alignment of crystalline domains along the 5 directions of the quasicrystalline substrate. This is in agreement with observations of Xenon atoms adsorbed on the ten-fold decagonal Al-Ni-Co surface and numerical simulations of weakly adsorbed atomic systems. Intermediate phases are observed for colloid-substrate interactions strong enough to produce defects in the crystal. These defects adapt the form of rows of quadratic tiles. Surprisingly, for specific particle densities (at which the colloid-substrate interaction is minimized) we identify a novel pseudomorphic ordering. This intermediate phase which exhibits likewise crystalline and quasicrystalline structural properties can be described by an Archimedean-like tiling consisting of alternating rows of quadratic and triangular tiles. The calculated diffraction pattern of this phase is in agreement with recent observations of copper adsorbed on icosahedral AlPdMn surfaces. Interestingly, we also observe the formation of the same phase on tetradecagonal substrates also at densities for which the potential energy of the colloidal system is minimized. Although the structure can also be described by rows of triangles and rows of squares, a closer analysis reveals

substantial differences. Here, large domains with almost periodic ordering are found. We show that this behavior is closely related to the low density of highly symmetric local motifs in the substrate potential.

In the second part of this Thesis the conditions under which quasicrystals form are investigated. Currently, it is not clear why most quasicrystals hold 5- or 10-fold symmetry but no single example with 7 or 9-fold symmetry has ever been observed. Since the properties of quasicrystals are strongly connected to their atomic structure, a better understanding of their growth mechanisms is of great importance. In contrast to crystals which are periodic in all three dimensions, quasiperiodicity is always (except for icosahedral quasicrystals) restricted to two dimensions. Accordingly, three-dimensional quasicrystals are comprised of a periodic stacking of quasiperiodic layers and any hurdle in the formation of quasiperiodic order within a single layer will eventually prohibit their growth along the periodic direction. In this Thesis, we also report on geometrical constraints which impede the formation of quasicrystals with certain symmetries in a colloidal model system. This is achieved by subjecting a colloidal monolayer to N=5- and 7-beam quasiperiodic potential landscapes. Our results clearly demonstrate that quasicrystalline order is much easier established for N = 5 compared to N = 7. With increasing laser intensity we observe that the colloids first adopt quasiperiodic order at local areas which then laterally grow until an extended quasicrystalline layer forms. As nucleation sites where quasiperiodicity originates, we identify highly symmetric motifs in the laser pattern. We find that their density strongly varies with n and surprisingly is smallest exactly for those quasicrystalline symmetries which have never been observed in atomic systems. Since such high symmetry motifs also exist in atomic quasicrystals where they act as preferential adsorption sites, this suggests that it is indeed the deficiency of such motifs which accounts for the absence of e.g. materials with 7-fold symmetry.

In addition to the fundamental aspects, we report in this Thesis on the fabrication of large colloidal quasiperiodic layers incorporated in a polymer hydrogel matrix. Because quasicrystals have higher point group symmetry than ordinary crystals, micrometer-scale quasicrystalline materials are expected to exhibit large and isotropic photonic bandgaps in the visible range. In our case, the quasiperiodic symmetries are induced using extended light fields. The reported gelled colloidal quasicrystals are unique in that they have large sizes as well as good optical uniformity. With laser diffraction the in situ variable length scale of such materials is demonstrated.

In conclusion, we have studied the phase behavior of charged colloidal particles interacting with quasiperiodic laser fields. We showed that novel pseudomorphic growth can lead to the formation of a phase which exhibits likewise crystalline and quasicrystalline structural properties. We also performed unconventional measurements in order to understand why the formation of quasicrystals is limited to specific rotational symmetries. We have found that geometrical hurdles play a crucial role in the proliferation of quasiperiodicity and that such hurdles can hindered or even prohibited the formation of e.g. 7- or 9-fold symmetry. And finally, we have shown that the combination of extended light fields and hydrogel matrices leads to the for-

mation of large quasiperiodically ordered colloidal materials.
Parts of this work have been published elsewhere:

- J. Mikhael, J. Roth, L. Helden C. Bechinger. Archimedean-like tiling on decagonal quasicrystalline surfaces. Nature (2008) 454: 501-504.
- J. Mikhael, M. Schmiedeberg, S. Rausch, J. Roth, H. Stark C. Bechinger. Proliferation of anomalous symmetries in colloidal monolayers subjected to quasiperiodic light fields. PNAS (2010) doi: 10.1073/pnas.0913051107.
- M. Schmiedeberg, J. Mikhael, S. Rausch, J. Roth, L. Helden, C. Bechinger H. Stark. Archimedean-like colloidal tilings on substrates with decagonal and tetradecagonal symmetry. Submitted to EPJ E (2010).

CHAPTER 1

INSIGHT INTO QUASIPERIODIC ORDER

The discretely diffracting quasicrystals, discovered in the early 1980s, have led to an interdisciplinary activity involving crystallography, mathematics, materials science, surface science, and lately soft condensed matter. The first part of this chapter is intended to give an overview on the discovery of quasiperiodic order, its mathematical description in higher dimensional space, the characteristics of the orientational order for different tilings and its manifestation in the Fourier space. We also consider the origins of phonon and phason-strain fields leading to different types of disorder in quasiperiodic lattices. The new understanding of the surface structure of quasiperiodic metals and how adsorbed atoms can arrange pseudomorphically on it are considered. Finally, the exciting discoveries of dodecagonal order in mesoscopical systems are presented and the difficulties obstructing the formation of colloidal crystals with quasiperiodic order are discussed.

1.1 Historical overview on quasicrystals

Conventional crystals are ordered structures constructed by periodically repeating unit cells. Their macroscopical symmetry, i.e. external shape, is the result of this periodic internal order. These well established ideas were developed back in the 17th and 18th century, and are considered as the basis of modern crystallography. In 1619, Johannes Kepler wrote his famous book 'Harmonices Mundi' and discussed the congruence of regular figures. He showed that there are only three ways in which a plane could be filled perfectly without gaps or overlaps using one type of regular polygons. Accordingly each point or vertex could be surrounded by only six triangles or four squares or three hexagons [1]. This means that periodicity is only compatible with 2-, 3-, 4- and 6-fold rotational symmetries (figure 1.1). Based on this, the French mineralogist René Just de Haüy started in 1801 formulating the mathematical theory of crystallography in the 'Traité de minéralogie'. He described the construction of regularly shaped crystals out of smaller symmetric units, i.e. cubes, octahedra, te-

trahedra, and he omitted the icosahedra since it was widely believed that crystals can not have the five-fold symmetry. Later, Bravais, then Schoenflies and Fedorov developed independently the mathematical theory of periodic patterns on the basis of purely geometrical reasoning. Only with the discovery of X-ray diffraction in 1912 by Max von Laue, the existence of the atomic periodicity was experimentally proved by X-ray diffraction. In the following years, the internal structure of many crystals was determined based on the work of Bragg. At that time it was a common belief that the ground state of ordered matter was a periodic arrangement and as a consequence each crystal structure can be described by one of the 230 space groups resulting from 14 Bravais lattices and 32 point groups.

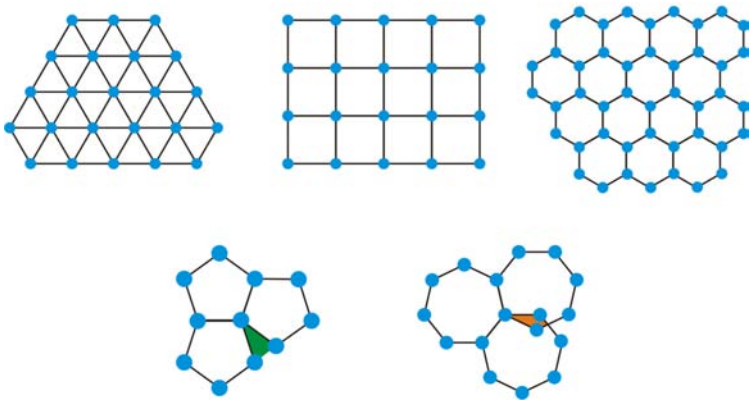

Figure 1.1: Different structures each based on one type of regular polygons. Using triangles, squares, and hexagons, a uniform periodic tiling is achieved. On the contrary, the use of pentagons leads to the occurrence of gaps (in green) and using heptagons leads to overlaps (in orange). This illustrates the incompatibility between periodicity and rotational symmetries like five-fold, seven-fold or higher.

In the sixties, this conviction started to weaken with the discovery of some materials with diffraction patterns indicating the presence of aperiodicity. In 1972, de Wolf developed a description of such incommensurate modulated phases. For these aperiodic crystals, the positions of the atoms deviates in a aperiodic way from the positions of a conventional periodic crystal (figure 1.2).

In 1982, Dan Shechtman made a revolutionary and controversially discussed discovery. While investigating the structure of an alloy of AlMn produced by rapid quenching, he observed an electron diffraction pattern showing the non-crystallographic five-fold symmetry. The first reactions of the most eminent metallurgists and physicists were negative. Among them, the double Nobel prize Laureate Linus Pauling who kept believing that this is only an apparent icosahedral symmetry and it is due to multiple twinning of periodic cubic crystals. Nevertheless, Shechtman and coauthors were able to show that the symmetry is indeed a real property of the solid

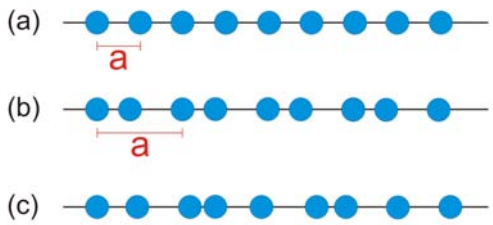

Figure 1.2: Periodic chain of atoms (a) transforming into another periodic chain with larger period due to a commensurate modulation (b) and transforming into an aperiodic chain due to an incommensurate modulation (c).

and published their result two years after the discovery [2]. Only six weeks later, Levine and Steinhardt published the first theory of these quasicrystals, i.e. solids having long range order without periodicity. In 1992, the International Union of Crystallography abandoned the old definition of a crystal which was based on the lattice periodicity and adapted a new definition where a crystal is any solid having essentially discrete diffraction diagram, i.e. including quasicrystals. To conclude, the discovery of quasicrystals showed that the microscopic periodicity is a sufficient but not a necessary condition for giving sharp diffraction spots meaning that crystals could have long range order without periodicity. Nowadays, hundreds of materials synthesized in the labs are known to be quasiperiodic and other non-crystallographic symmetries have been found such as the eight-, ten- and twelve-fold [3]. Moreover, quasicrystals can also form under geological conditions. Lately, Bindi et al. have reported the discovery of a natural mineral (alloy of aluminum, copper, and iron) occurring as micrometer-sized grains with several fivefold symmetry axis [4].

It is true that quasicrystals were discovered only in 1982, but in fact quasiperiodicity was known and unfortunately overseen even before. In fact, it was lately reported that Islamic tilings made in the 15th century and used as decoration show nearly perfect quasiperiodicity [5]. Even Johannes Kepler in the 16th century was very close in discovering quasiperiodicity when he presented well-ordered tilings of a plane consisting of pentagons and decagons. This same tiling, which will be later discussed in details, was then rediscovered by Sir Roger Penrose in 1974 and this time using only two rhombus tiles. Yet even the mathematical description of quasiperiodic functions did not emerge after the discovery of Dan Shechtman. Back in the 30's, the mathematician Harald Bohr (brother of Niels Bohr) introduced in his book 'Almost Periodic Functions' a very important concept, called the hyperspace, for quasiperiodicity. Since this concept is very useful in capturing many features of quasicrystals, we will dedicate the next section to its description.

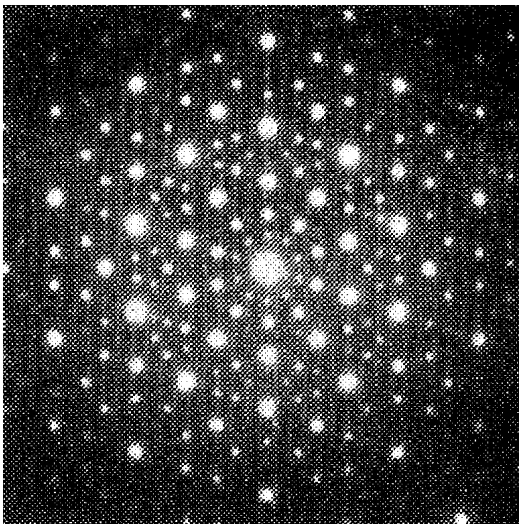

Figure 1.3: First diffraction pattern observed by Shechtman in 1982 and later published in 1984 with the non-crystallographic icosahedral symmetry. The solid is a complex metal alloy including Al and Mn [2].

1.2 Mathematical description

1.2.1 Crystallographic restriction

In order to understand the impact of the discovery of materials having long range order without periodicity one should recall what non-crystallographic symmetries are. A perfect crystal is a periodic structure possessing a translation symmetry meaning that there is a group of atoms that can build up the whole crystal simply by translations. The smallest of such groups is called the elementary cell. Mathematically this translational symmetry is described by means of vectors a_i $(i = 1, ..., D)$ where D is the number of space dimensions, such that the structure remains invariant under translations by any vector which is the sum of integral multiples of these vectors. The vectors R_i with n_{i_j} integers are called lattice vectors and define a Bravais lattice, while a_i are the basis vectors.

$$R_i = \sum n_{i_j} a_i, (j = 1, ..., D,) \tag{1.1}$$

Apart from translational symmetry, there are other structural symmetries that transform a crystal into itself. These are *point group* symmetries; i.e. all operations that transform the lattice into itself and leave a given point invariant. These operations are rotations, reflections and inversions. The *space group* symmetries are the point group operations plus the translations.

The possible rotation symmetries of a periodic set of points, also called the *crystallographic* set of points, are not infinite. This obstruction is called the crystallographic restriction [6]. Consider two nearest neighbor atoms A and B, with the distance in between the unit of length. By performing a rotation by $2\pi/n$, of the line joining

both atoms around A (figure 1.4 (a)), the distance between the new position B' and the atom nearest neighbor B, becomes:

$$L = 2\sin\pi/n \tag{1.2}$$

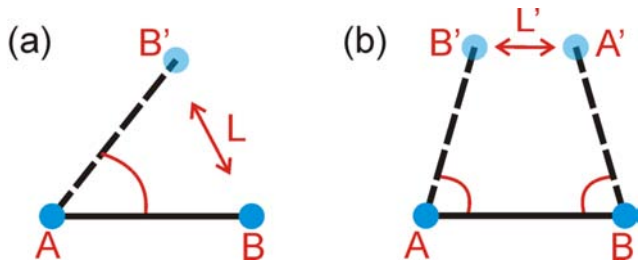

Figure 1.4: Illustration of the crystallographic restriction in two dimensions. (a) Assuming that A and B are nearest neighbors atoms, L is then the distance between B and B' after a rotation of $2\pi/n$. (b) L' is the distance between A' and B' after a rotation of $2\pi/n$ around A and B in different directions.

Since by definition, L must be larger than the unit length ($L > 1$), a contradiction results for $n \geq 7$, as $sin(\pi/n) < 1/2$ for $n \geq 7$. On the other hand, if one considers the case where $n = 5$ and performs the rotation around one point in one direction and around the other point in the other direction (figure 1.4 (b)), the distance between the new points becomes:

$$L' = 1 - 2\cos 2\pi/5 \tag{1.3}$$

This means that L' is also smaller than unity, leading again to a contradiction.

The crystallographic restriction illustrated above in two dimensions, also holds for three dimensions. In three dimensions a rotation of angle $2\pi/n$ is a symmetry operation with a transformation consisting of an orthogonal matrix. Due to the discreteness of the lattice, the trace of this matrix given by $\pm(1+2\cos(2\pi/n))$ must be an integer [6]. This implies that $2\cos(2\pi/n)$ must also be an integer and n is restricted to 2, 3, 4 and 6.

1.2.2 Higher dimension crystallography

The most outstanding features of the experimentally observed quasicrystals are the observation of crystallographically forbidden symmetries in their diffraction pattern and the absence of any translation symmetry. This means that the picture in which the crystal structure is recovered by a simple translation of its unit cell breaks down. In order to theoretically construct such structures, an elegant method was developed based on the fact that quasiperiodic functions, e.g. mass density of a quasicrystal, could be derived from periodic functions embedded in a higher dimension space. This

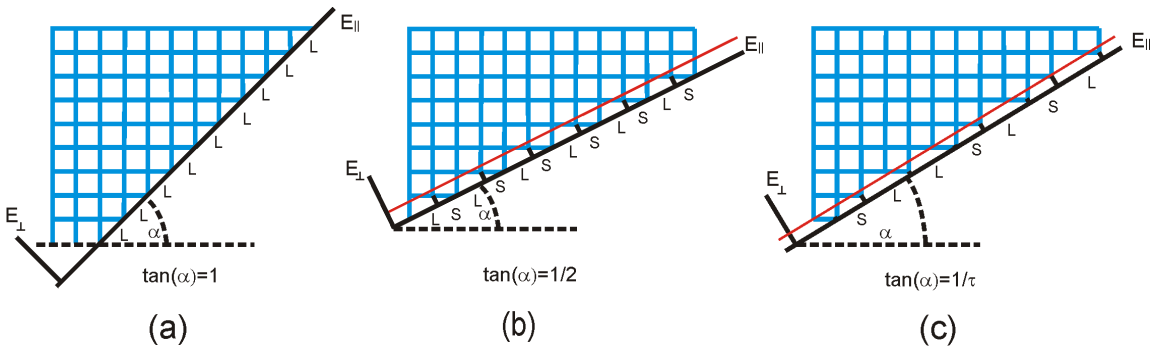

Figure 1.5: Construction by the cut and projection method. Two dimensional square lattice projection on a one dimensional subspace $E_{\parallel}$ at different angles α with the horizontal. $E_{\parallel}$ and $E_{\perp}$ are the two axis embedding the hyperspace. For a rational slope ((a) and (b)) the projected structure is a periodic set of sites with a repeating unit L in the first case and LS in the second. For an irrational slope the projected structure is an aperiodic Fibonacci sequence with an infinitely repeating unit (c).

rather hard to visualize description is best illustrated by producing a 1D quasiperiodic sequence by slicing a two dimensional square lattice. Consider the following function:

$$\rho(x,y) = \sum_{n,m} \delta(x - na) + \delta(y - ma), \tag{1.4}$$

ρ is the distribution of lattice sites at the vertices of a square lattice with a lattice constant a. This structure is embedded in a two dimensional space, also called the hyperspace, with axes $E_{\parallel}$ (physical space) and $E_{\perp}$ (perpendicular space). α is the angle between the horizontal rows of the square lattice and $E_{\parallel}$. When α is rational, $E_{\parallel}$ passes repeatedly through lattice sites of the square lattice and the resulting projected structure is then periodic where almost every site has the same global environment (figure 1.5 (a) and (b)). For $\tan\alpha = 1$, the sequence is represented by LLLLL..., consisting of just one segment L which is the repeating unit. For $\tan\alpha = 1/2$, the resulting structure turns into a high density of projected points. In order to overcome this problem, a projection window should be defined limiting the number of projected lattice sites to those belonging to a strip with a certain width (in red). In this case, the periodicity is not lost but the size of the repeating unit becomes larger and consists of two segments, a short one called S and a long one called L. For $\tan\alpha = 1/\tau$ ($\tau = (1+\sqrt{5})/2$ the golden ratio), the resulting structure becomes aperiodic. It is then characterized by two length scales $L = a\cos\alpha$ and $S = a\sin\alpha$ with $L/S = \tau$. Contrary to the periodic case, here no sites have the same global environment although there is an infinite number of sites with the same local environment. This is called *local indistinguishability* or also known as *isomorphism*.

Using this same method, one can also explain the idea of a *rational approximant*. As shown in table 1.1 the slope of $E_{\parallel}$ can be defined as the ratio of two successive Fibonacci numbers F_n/F_{n+1}, with $F_n = F_{n-2} + F_{n-1}$ and $F_0 = 0$ and $F_1 = 1$. In this

case the value of $\tan\alpha$ is given by the increasing rational approximants of inverse of the golden ratio τ. In the limit of $n \to \infty$, the rational approximant approaches the irrational value of $1/\tau$ and the basic unit becomes the infinite quasiperiodic Fibonacci sequence. In practice, many intermetallic alloys like, the Al-Pd-Mn for example, adapt structures which are very similar to quasiperiodic structures but still periodic. Small adjustments in the chemical composition or temperature lead to such periodic approximants with unit cells including hundreds of atoms.

Table 1.1: Sequence of long and short segments produced by the cut and projection method from two dimensions to one dimension for cut angles whose tangent is the ratio of successive Fibonacci numbers F_n/F_{n+1}.

n	$\tan\alpha = F_n/F_{n+1}$	basic unit	Unit length
1	1/1	L	1
2	1/2	LS	2
3	2/3	LSL	3
4	3/5	$LSLLS$	5
5	5/8	$LSLLSLSL$	8
6	8/13	$LSLLSLSLLSLLS$	13
7	13/21	$LSLLSLSLLSLLSLSLLSLSL$	21

The concept of cut and projection is not only valid for projections from two dimensional to one dimensional. It can be generalized in a way to produce two dimensional or three dimensional quasiperiodic structures. Icosahedral quasicrystals are structures which are quasiperiodic in three dimensions. They can be interpretated as a three dimensional slice through a periodic mass density function at least of dimension six. For planar quasicrystals, i.e. periodically stacked quasiperiodic layers, the minimal dimension of the embedding space is easily predicted using the so called *Euler's totient function* $\phi(n)$ [7]. This statement is a direct consequence of the structure of the so-called cyclotomic polynomials. For creating a planar quasiperiodic point set with n-fold symmetry, a lattice of at least dimension $\phi(n)$ is needed (figure 1.6). $\phi(n)$ is *Euler's totient function* defined as the number of positive integers less than n which are coprime to n. Two integers are coprime if their greatest common divisor is 1. The number 1 is coprime to every integer.

1.2.3 Quasiperiodic tilings and orientational order

Quasiperiodic structures do not have a finite unit cell. They are spatially ordered, and comprise more than one building block. These building blocks are called tiles, and the patterns that they form are called tilings. The most famous aperiodic tilings were discovered by Roger Penrose in 1973 and 1974. The P3-Penrose tiling consists of just two rhombus tiles. It is built out of a skinny rhombus with angles of 36°and 144°, and a fat rhombus with angles of 72°and 108°(figure 1.7). These two tiles are not placed

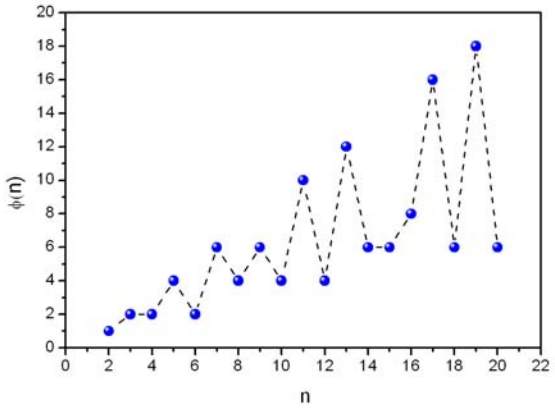

Figure 1.6: Euler's totient function $\phi(n)$. $\phi(n)$ is the number of positive integers less than n which are coprime to n.

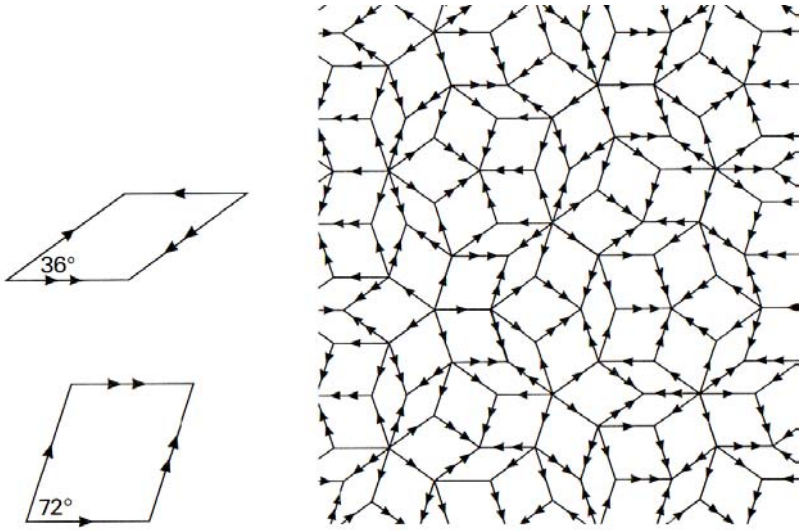

Figure 1.7: Perfect Penrose tiling consisting in two rhombus tiles: skinny and fat with characteristic angles 36°and 72°, respectively. The arrows on the edges are required to match each other in the tiling in order to ensure the quasiperiodic order.

randomly next to each other. In order to ensure a perfect long range quasiperiodic order without gaps or stacking faults, matching rules are applied. Exemplary, we show here in figure 1.7 a perfect tiling with matching rules represented by arrows. The edges of the tiles that are allowed to touch each other are those decorated with the same arrows.

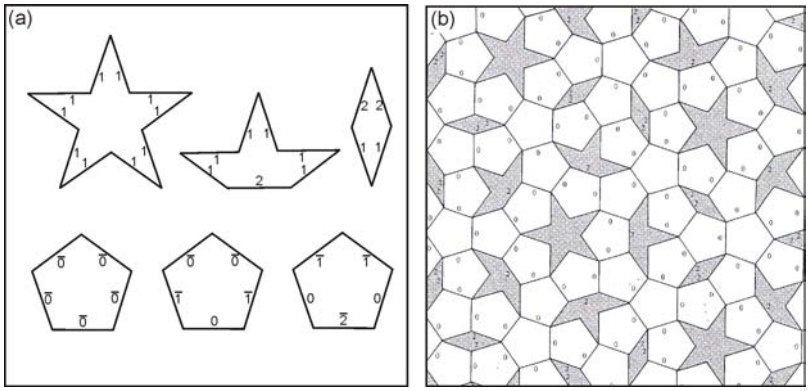

Figure 1.8: P1 Penrose tiling consisting in four different tiles: pentagonal stars, crowns, rhombuses and pentagons. Due to the matching rules one can distinguish three different pentagons. Here the matching rules are labeled by numbers (0, 1, 2,..). On adjacent tiles numbers without the bar must fit against numbers with the bar, e.g. 1 must fit with $\bar{1}$. For clarity numbers other than 0 and 2 are omitted.

Another important and widely used tiling also discovered by Penrose is the P1-Penrose tiling (figure 1.8). High resolution scanning tunneling microscopy (STM) of the fivefold surface of the icosahedral $AlPdMn$, the most studied quasicrystal, can be tiled with this tiling [8, 9]. As shown in figure 1.8, it consists of pentagonal stars, crowns, rhombuses and pentagons. The edges are labeled by 0, 1, 2 and $\bar{0}$, $\bar{1}$, $\bar{2}$ corresponding to the matching rules. On adjacent tiles numbers without the bar must fit against numbers with the bar.

As stated in the previous subsection, any quasiperiodic structure could be understood as periodic but in a higher dimensional space including an orthogonal space (parallel space). For the Penrose tilings, Bruijn showed in 1981 that they can be derived by a projection from a five dimensional cubic lattice.

By now other methods for constructing quasiperiodic tilings have been developed. Among them the substitution method based on the inflation and deflation of the tiles or the dual grid method [11]. The latter has the advantage of being able to create tilings with arbitrary real space orientational symmetries. The method is based on rotating equidistant parallel lines by angles of $2\pi k/n$ with $k = 0, 1, ..., n-1$ where n is a positive integer. The yield is a n-fold grid which dualization gives an n-fold tiling. Each vertex of the tiling corresponds to a polygon in the grid.

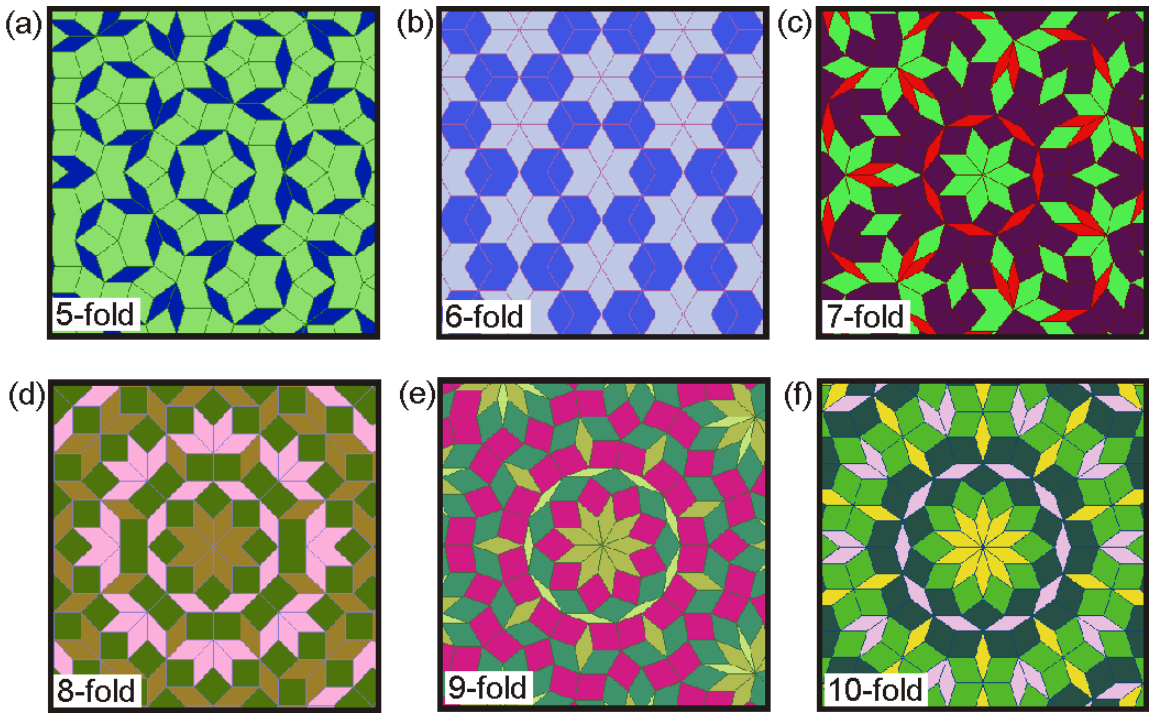

Figure 1.9: n-fold grids created by the dual grid method with n= 5, 6, 7, 8, 9 and 10. The construction principle is based on overlapping a n-set of equidistantly spaced lines, whereby every other grid is rotated by an angle of $2\pi k/n$ with $k = 0, 1, ..., n-1$. The rhombic tiles are generated by a dual transformation. The tiles are colored randomly. A shift of the individual grids with respect to the origin will result in different tilings [10].

1.2.4 Two dimensional structure factor

The two dimensional structure factor, or diffraction pattern, of a set of atoms contains many valuable information not only on the structure and symmetry but also on the different types of disorder that can occur [12, 13]. Diffraction on periodically ordered crystals gives sharp periodically spaced Bragg peaks, but diffraction on liquids gives only diffuse scattering because of the lack of long range order. The question is how the absence of periodicity in quasicrystals would affect the diffraction pattern.

Although it might be not very intuitive, quasicrystalline structures can have diffraction patterns with discrete and dense Bragg peaks. Experimentally, many high quality quasiperiodic diffraction patterns have shown sharp Bragg peaks, sometimes better than those emerging from perfect conventional periodic crystals such as silicon. The mathematical clue to understand this is based on the high dimensional crystallography approach with the difference that it should be carried out in the reciprocal space. The idea is also clarified if we simply consider once again the one dimensional Fibonacci sequence and look at its diffraction pattern using simple intuitive arguments. Because of its aperiodicity, the sequence can be understood as a sum of two periodic functions with two incommensurate periods. Thus, in reciprocal space the full pattern consists of two sets of Bragg peaks corresponding to two functions and their linear combinations. Because of the incommensurability, the peaks will fill densely the reciprocal space. Even though the structure is one dimensional, the diffraction peaks are indexed with two integers and this is due to the fact that the Fibonacci sequence is periodic in a two dimensional space.

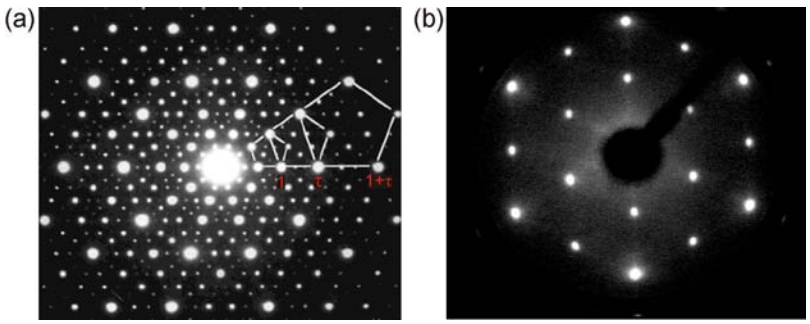

Figure 1.10: (a) X-ray diffraction pattern from a icosahedral quasicrystal oriented along the fivefold axis. The white lines connecting the spots show the aperiodic spacing. (b) Electron diffraction pattern from a Fe_3O_4 sample oriented along the (111) surface. The spacing between the spots is periodic.

Figure 3.4 shows a diffraction pattern taken from a quasicrystal oriented along the fivefold surface and a diffraction pattern from a periodic crystal (Fe_3O_4) oriented along the (111) surface. In (a) the spacing between the discrete diffraction spots along a radial is related to the golden ration τ and the diffraction pattern has a 10-fold rotational symmetry. In (b) the spacing is periodic and the diffraction pattern has a 6-fold symmetry. Since a quasiperiodic reciprocal lattice includes a dense set of peaks, one can observe in (a) the high and dominant peaks and in between an

infinite number of smaller ones. Such a feature does not occur in periodic reciprocal lattices. Experimental diffraction patterns have usually a finite number of peaks due to the finite resolution of the detectors.

Crystals are typically characterized by the minimum number Δ of incommensurate wave vectors, called the rank, which is required to span the reciprocal space with spatial dimension D. The rank of two dimensional lattices is given by the Euler totient function introduced in section (1.2.2). As a consequence, periodic structures have $\Delta = D$ and quasiperiodic ones $\Delta > D$. Accordingly, two dimensional periodic lattices have rank $\Delta = 2$. Interestingly, for all experimentally observed axial quasicrystals $\Delta = 4$. In contrast, structures with $\Delta = 6$, e.g. 7-fold tilings, or with $\Delta > 6$ have not yet been found.

1.2.5 Symmetry of quasiperiodic structures

The symmetry nomenclature of quasicrystals is not unified in the literature. A two-dimensional periodic crystal contains more than a single point about which an n-fold rotation brings it into perfect coincidence with itself. For quasicrystals the real space orientational order is defined by the unique n-fold star of vectors located at the center of the tiling (figure 1.9). For most experimental studies, the symmetry is only accessible by diffraction (Laue symmetry). But the point group symmetry of the diffraction pattern is not neccessary the same as the real space symmetry. The diffraction patterns, can exhibit n- or 2n-fold symmetry. All n-fold symmetric two-dimensional structures have in fact 2n-fold diffraction patterns for n odd, and n-fold for n even [14]. The two-dimensional Penrose tiling, for instance, is pentagonal (5-fold) because in real space it includes only one vertex of exact 5-fold symmetry and its diffraction pattern is decagonal (10-fold).

1.2.6 Phonons and phasons

The structure of periodic or quasiperiodic crystals is not simply consisting of atoms resting at their lattice sites without dynamic or even static defects. Due to thermal energy, atoms oscillate around the equilibrium position and can also jump from one position to another. Such effects have of course a major importance on many properties of materials such as mechanical, optical, thermal, acoustic, or other. The legitime question that we are interested in discussing here is whether the special features of quasiperiodic symmetry have any influence on the nature of static defects or the low energy excitations independently from the details of the interatomic interactions.

As shown previously, even if a solid structure is quasiperiodic in the D dimensional real space (parallel space) one can always lift it to a higher dimension space (d dimensional) in which the aperiodic structure becomes periodic (refer to section 1.2.2). The mass density $\rho(r)$ at a position r can be expressed by a Fourier series

$$\rho(r) = \sum_G \rho_G \exp(iG.r), \tag{1.5}$$

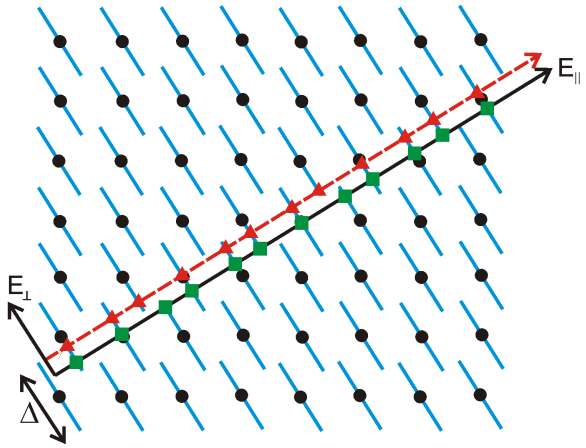

Figure 1.11: Uniform phason shift produced by a translation of $E_{\parallel}$ (black full and red dashed lines). The black dots represent the atom positions on the square lattice, the blue lines (δ) define the projection window, the green squares form the first projected structure and the red triangles the projection after translation of $E_{\parallel}$.

where G represents the reciprocal lattice vectors. ρ_G is the Fourier component of the ordered structure and is a complex number with an amplitude $|\rho_G|$ and a phase ϕ_G. When the atoms are at their equilibrium positions, the phase ϕ_G has a specific value ϕ_G^0. If the atoms are displaced from their equilibrium positions by a vector u, the phase ϕ_G becomes:

$$\phi_G = \phi_G^0 + G.u, \tag{1.6}$$

For periodic crystals, the d dimensional space is nothing but the parallel space [15], i.e. d=D. A spatial variation in u leads to phononic excitations. For quasicrystals, d is larger than D. The mass density description written above only corresponds to the periodic structure embedded in the high dimension space. The physics that occurs in the parallel space should be derived from the high dimension space. One can refer to the cut-projection theorem [16], which states that a cut in the real space corresponds to a projection in the reciprocal space. As a result, the Fourier component $\rho_{G_{\parallel}}$ of the density in the parallel space is then equal to ρ_G with $G_{\parallel}$ the component of G in the parallel reciprocal space. Since amplitudes and phases are preserved in a projection procedure, the density wave can be written in the parallel space as

$$\rho(r_{\parallel}) = \sum_{G_{\parallel}} \rho_{G_{\parallel}} \exp(iG_{\parallel}.r_{\parallel}), \tag{1.7}$$

and the displacement vector u describing the shift of the atoms from their equilibrium positions has now two components, $u_{\parallel}$ and $u_{\perp}$. As a consequence the phase can be written as

$$\phi_{G_{\parallel}} = \phi_G^0 + G_{\parallel}.u_{\parallel} + G_{\perp}.u_{\perp}. \tag{1.8}$$

As in the case of periodic crystals, the vector field $u_{\parallel}$ leads to atomic displacements in the parallel space. One speaks here about propagating phononic modes. The $u_{\perp}$ vector field leads to modes only characteristic to quasicrystals. Since the displacements take place in the complementary space, the corresponding strain field exclusive to quasicrystals is called phason-strain field.

Although it may sound non-intuitive, the mathematical cut and projection method allows us to look at such diffusive modes [13]. A uniform translation of the cut space to a different position leads to structural changes in the quasicrystal without any change in the total free energy of the system. The effect of a spatially varying $u_{\perp}$ vector field is shown in figure 1.11. As in figure 1.5(c), we perform here a projection of a two dimensional square lattice but this time followed by a translation of $E_{\parallel}$ which corresponds to the uniform translation of $u_{\perp}$. Although the resulting projected structure remains a part of the Fibonacci sequence, one can notice that many atom positions have vanished while others were created. In fact, (S, L) or (L, S) bound pairs were reversed.

At low temperatures, spatially varying vector fields can lead to two types of frozen disorder in quasicrystals. In the conventional periodic crystals the $u_{\parallel}$ field leads to a distortion in the unit cell. In quasicrystals this is translated into a distortion in the tiles by a continuous displacement of the lattice sites without any rearrangement. A spatially varying $u_{\parallel}$ field has a different effect on the quasilattice. It leads to rearrangements of the tiles and consequently a disruption of the quasiperiodic order. These effects are observed in figure 1.12 on the Penrose tiling. The distortion due to the phonon-strain can be exemplarily seen in figure 1.12(b) on the red decagonal tile. The dots in (c), point out the positions in the Penrose tiling where the matching rules are isolated. It is important to mention that these violations are localized and do not affect the surroundings. Since such strain fields depend only on the symmetry and not the specific interatomic interactions, in a later section their relevance and occurrence in quasiperiodic light lattices will be discussed.

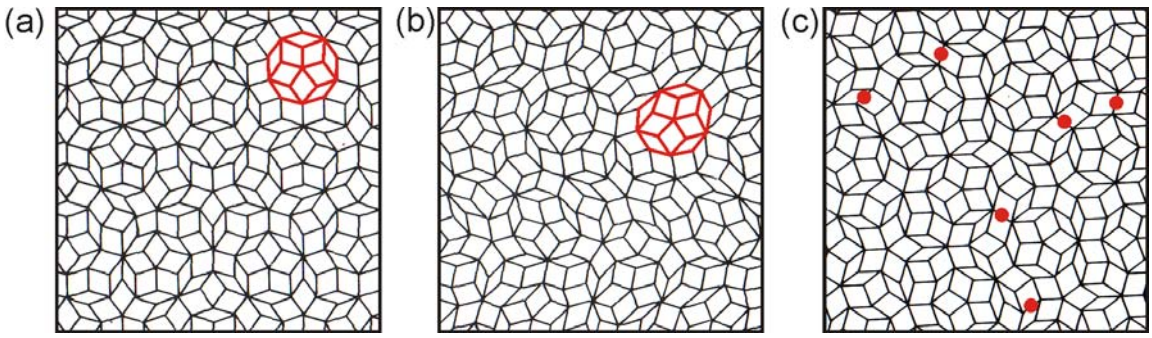

Figure 1.12: (a) Perfect Penrose tiling. (b) Tiling with phonon-strain. The red tiles give an example on the distortion due to the strain field. (c) Tiling with phason-strain. The red dots point the positions where the matching rules are violated [17].

1.3 Surfaces and interfaces

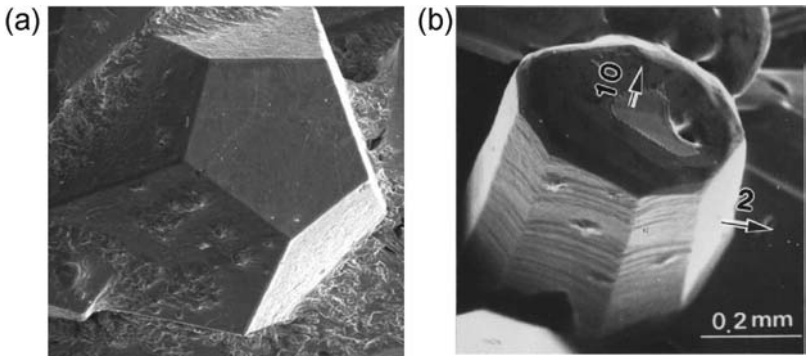

Figure 1.13: Scanning electron microscopy micrographs of a large single grain of icosahedral (a) and decagonal (b) quasicrystals. The arrows in (b) correspond to the high symmetry axes [18].

More than a hundred quasicrystalline systems have been identified since the discovery of quasiperiodic materials. They are mostly Aluminum based and are composed out of three or in rare cases two chemical elements with specific stoichiometry (ternary or binary alloys) [19]. Due to the structure complexity and the elaborated chemical composition of quasicrystals, the exact bulk structure is still not perfectly known. Nevertheless, the growth techniques and the quality of the samples have improved a lot and large single-grain samples are now available. These advances have opened the way for a large and interesting research field which is the study of the surfaces of these materials as well as the adsorption of atomic overlayers.

1.3.1 Surface structure

Table 1.2: List of available quasicrystal samples and their most studied surfaces by various techniques. "$i-$" stands for icosahedral and "$d-$" for decagonal. The nomenclature of the surfaces refers to the high symmetry axis of the bulk to which the corresponding surface is orthogonal [18].

Sample	$i-AlPdMn$	$i-AlCuFe$	$i-AlCuRu$	$d-AlNiCo$	$d-AlCuCo$
Surfaces	5f, 2f, 3f	5f	5f	10f, 2f	10f, 2f

To date, a limited number of clean and flat quasiperiodic surfaces are available for surface studies. Table 1.2 lists the most common ones [18]. The structures were characterized using different diffraction techniques such as: LEED (low energy electron diffraction), XPD (X-ray photoelectron diffraction) and HAS (helium atom scattering). The long range order and the symmetry were identified using the first two techniques while XPD gives information on the short range order. But due to the

lack of periodicity and information about the phase, the diffraction techniques are not enough to reveal the exact atomic ordering. Usually in addition to diffraction, a combination of TEM (transmission electron microscopy), STM (scanning tunneling microscopy) and ab-initio calculations are required.

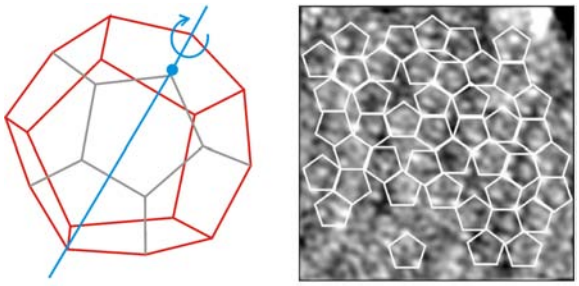

Figure 1.14: Fivefold rotation axis in a dodecahedron and tiling of the high resolution STM pictures of the corresponding surface of an i-Al-Pd-Mn sample. The tiling is a P1-Penrose tiling [8].

The icosahedral quasicrystals (like i-AlPdMn) lack periodicity along any direction. They posses three types of high symmetry axes: fivefold, threefold and twofold axes. The symmetry is also reflected on the macroscopic scale by the dodecahedral shape and the fivefold facets of the samples. The orthogonal surface to the fivefold axis, called fivefold surface (5f-surface), is the most studied quasiperiodic surface because of its high stability. STM studies of this surface showed large and flat terraces in the order of several hundreds of nanometers separated by stair-like steps. The step heights were often found to be related by the golden ratio τ and appear in a Fibonacci sequence (LSLLSLSL...). From the first atomic resolution STM pictures, fivefold stars with two orientations were identified [20]. Later, using Fourier transform pass filters two features of the surface were highlighted: the dark pentagonal stars and the white flowers (figure 1.15). The pentagonal stars correspond to truncated building blocks of the bulk called Bergman clusters and in some cases they are created by surface vacancies. The white flowers correspond to a central truncated pseudo-Mackay cluster surrounded by five Bergman clusters [21]. Ledieu et al. were also successful in tiling this surface with the P1- Penrose tiling consisting of four different tiles: pentagon, star, crown and a rhombus [8]. It is very important to mention that this surface do not show reconstruction [22] therefore it can be considered as a cut of the bulk and each atomic layer can be a termination layer.

Decagonal quasicrystals are different than the icosahedral ones. They lack periodicity only in one direction. The samples have the shape of a decagonal rod with a unique tenfold high symmetry axis and two twofold axes (figure 1.13). It consists of quasiperiodic layers stacked periodically along the third dimension (axial symmetry). Because this sample has both periodic and quasiperiodic surfaces with the same chemical composition, it was used in many studies in order to investigate whether the physical properties are more influenced by the structure or the chemistry [23, 24]. Depending on the composition and temperature, different phases of the decagonal

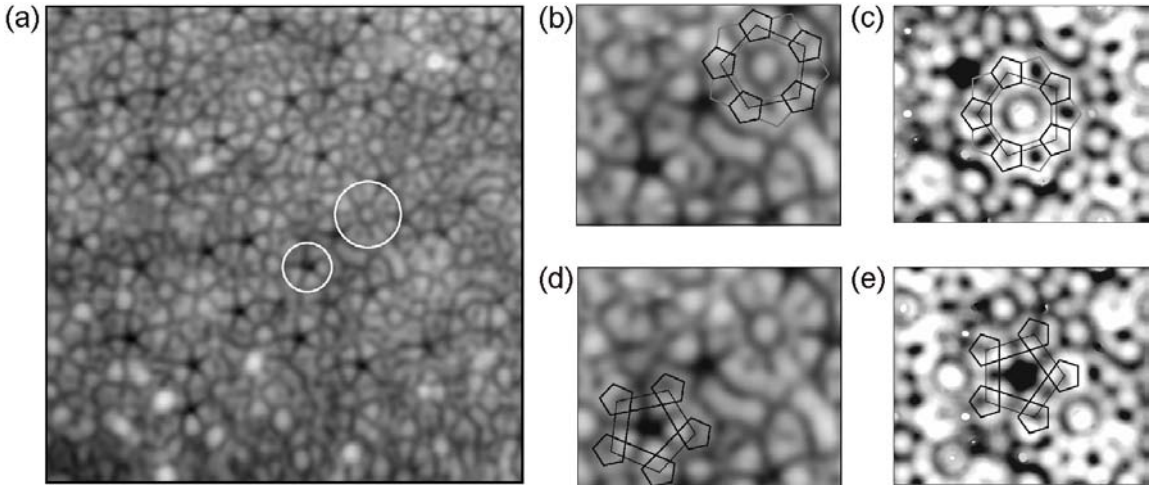

Figure 1.15: (a) Experimental STM picture of the fivefold surface of the i-AlPdMn showing two typical features: "White Flower" and "Dark Star" highlighted with circles. (b-c) Zoomed STM pictures showing a white flower. (b) is taken from (a) and (c) is calculated using ab initio density functional methods. (d-e) same as (b-c) but for the dark star [21].

AlNiCo were observed. The atomic structure of the surface differs in details from one phase to the other. However, there are many common features. Each plane has a pentagonal symmetry and is rotated by an angle of 36° with respect to the next neighboring plane. Characteristic pentagonal-star shaped motifs were identified, all of which have the same orientation within a terrace layer and the opposite orientation in adjacent terraces in agreement with bulk structure models. Since the diffraction techniques (as LEED) average over several planes, the global or overall symmetry is then decagonal. The tiling is also different for different phases. STM studies have shown that also this surface has a step-like morphology, with rough steps. Also pentagonal features are to be observed in the high resolution STM pictures. Here all the pentagons have the same orientation.

1.3.2 Growth of atomic overlayers

Monolayers on crystalline surfaces often form complex structures having physical and chemical properties strongly differing from those of their bulk phases [25]. Such hetero-epitactic overlayers are currently used in nanotechnology and understanding their growth mechanism is important for the development of novel materials and devices. Compared to crystals, quasicrystalline surfaces exhibit much larger structural and chemical complexity leading to e.g. unusual frictional [23], catalytical [26] or optical properties [27]. Accordingly, deposition of thin films onto such substrates can lead to novel structures which may even exhibit typical quasicrystalline properties.

Because quasicrystalline order does not occur in single element systems but only in binary [28] or even more complex ternary metal compounds, their surfaces exhibit

a high degree of structural and chemical complexity and show intriguing mechanical, electrical and optical properties [29]. In order to understand the origin of those characteristics it would be helpful to disentangle structural and chemical aspects which can be achieved by growing single-element monolayers to quasicrystalline surfaces [30, 31]. Apart from understanding how quasicrystalline properties can be transferred to such monolayers, this approach might allow fabrication of materials with novel properties.

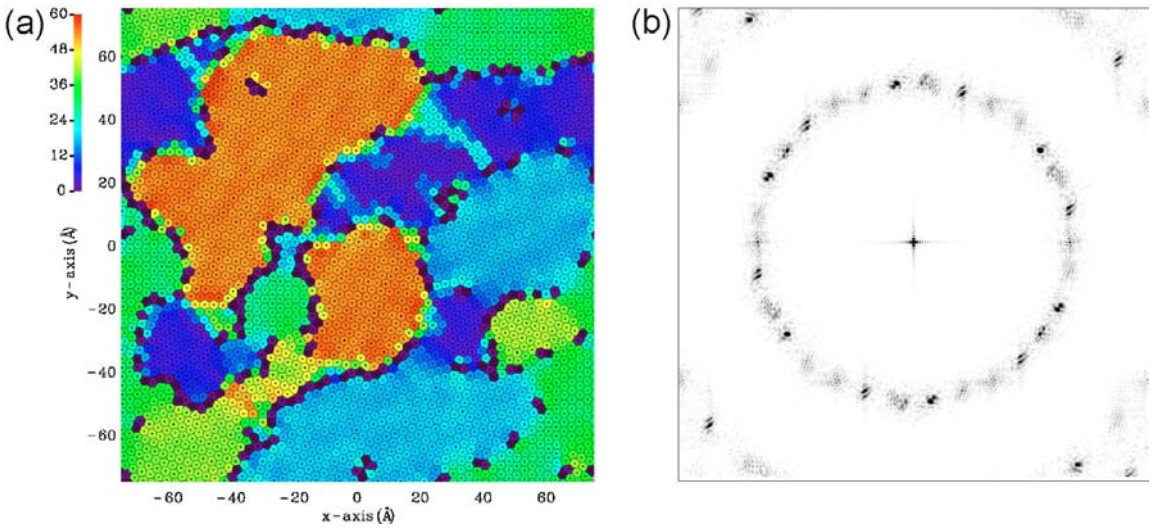

Figure 1.16: Molecular dynamics calculations of adatoms on quasiperiodic substrate potentials [32]. (a) Voronoi construction of the real space configuration of the adatoms. The hexagons have been color coded with respect to their orientation relative to the x axis. The sharp boundaries consist of topological defects. One can also see continuous transitions between domains whose orientation differs by 12°. (b) The corresponding diffraction pattern showing 30 peaks attributed to the five different spacial orientations of hexagonal domains.

Now that the surface structure is well understood [33], a number of hetero-epitaxial growth experiments on quasicrystalline substrates are performed and mainly common crystalline adsorbate structures were observed [30, 34]. Shimoda et al. investigated the adsorption of two transition metals, Gold (Au) and Platinum (Pt), on the fivefold i-AlPdMn and the tenfold d-AlNiCo [35]. A two dimensional growth of several face-centered cubic (fcc) $AuAl_2$ domains, multiply twinned, was observed. However, the directional order of the adsorbate proved to be in accordance with the directional order of the substrate. Similar phenomena have been also observed for Silver (Ag) on different substrates [30]. Here the hexagonal islands were observed to grow vertically at higher coverage while keeping five different orientations, rotated by $2\pi/5$, thus reflecting the symmetry of the substrate. Maybe it is more astonishing to know that even the noble gas Xenon (Xe) did not adapt at high coverages the surface's

quasiperiodic ordering. Instead, an fcc structure was reported in both experiments and simulations [36, 31].

Bilki et al. investigated these phenomena by performing molecular dynamics calculations [32, 37]. They modeled the multilayer adsorbate configuration by a single layer with an adjustable relative strength of interactions between adatoms. Despite the simplifications, their results captured many of the features mentioned above (figure 1.16).

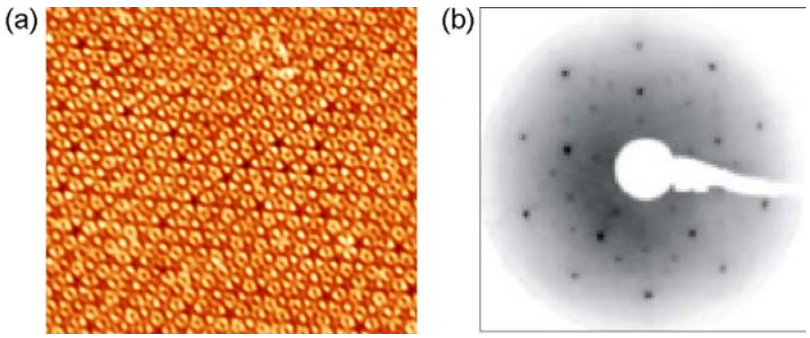

Figure 1.17: Epitaxial growth of lead (Pb) atoms on the fivefold i-AlPdMn. (a) STM image of the surface after deposition. (b) LEED pattern after deposition. The spot positions are related by a τ scaling within experimental error [38, 39].

Long range ordered quasicrystalline monolayers of Silicon (Si), Bismuth (Bi), Antimony (Sb), Tin (Sn) or Lead (Pb) were also studied by LEED, HAS and STM [40, 41, 42, 38, 39]. However, atomic resolution STM images were not always achieved thus the structural relationship between the substrate and the adsorbate was not accessible. For some of these experiments structural models based on ab initio calculations were developed calculating the preferred adsorption sites within the pentagonal tiles on the quasicrystal surface [43]. The proliferation of the quasiperiodic order in the overlayers showed to be depending on the preferential absorption sites. Depending on the specific interactions between the adsorbate and the quasicrystalline surface, two preferential adsorption sites have been identified. In the case of Si, Bi and Pb, which showed an epitaxial growth, it is the white flowers corresponding to a truncated pseudo-Mackay cluster [39, 44, 45]. While Al, Ag, Sn and for e.g. C60, which preferably adsorbed at the dark stars did not show any epitaxial growth at monolayer coverages [18].

The reduced chemical complexity of the lead monolayer which adapted the structure of the quasiperiodic surface showed an electronic behavior that could be only assigned to the quasiperiodic structure. Measurements of the electronic structure of the system using scanning tunneling spectroscopy and ultraviolet photoemission spectroscopy revealed that the Pb monolayer displays a pseudogap at the Fermi level which is directly related to its quasiperiodic structure.

1.4 Quasiperiodicity in the mesoscopic scale

To date, the majority of identified quasicrystals are metal alloys synthesized in the laboratory under controlled conditions mostly with icosahedral or decagonal point-group symmetry. Lately, one example of naturally occurring icosahedral AlCuFe was reported [4]. This finding suggests that metallic quasicrystals can form and remain stable even under geologic conditions. But is quasiperiodic order exclusive to metals?

1.4.1 Self-assembled quasicrystals

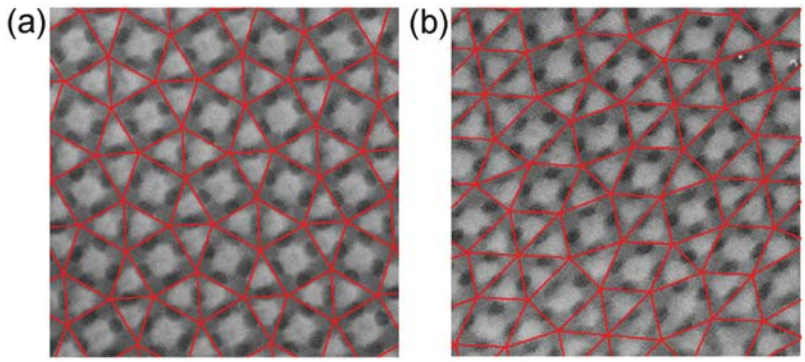

Figure 1.18: Transmission electron micrographs of ABC star polymers. (a) Triangle-square tiling superimposed on the micrograph image showing the formation of a periodic (3.3.4.3.4) Archimedean tiling. (b) Here a different polymer ratio is used and no periodicity is observed in the arrangement of the square-triangle tiling [46].

Matter organizes itself also at larger length scales [47]. In soft condensed matter, characterized by weak interactions and important thermal fluctuations, a rich range of mesoscopical structural behaviors is observed. In these systems, the thermal energy k_BT is defining the energy scale (k_B is the Boltzmann's constant and T the absolute temperature), and the structure and symmetry emerge from the interplay between interactions and geometry. Quasiperiodic order is indeed found in several soft systems. Micellelar systems, polymers, and even binary nanoparticles violate the crystallographic rules and form quasicrystals with long-range positional order but lack periodicity [48, 46, 49]. In the first case, dendrimers having a conical shape self-assemble into micelles and form a perfect dodecagonal quasicrystal (12-fold). In the other case, three arm block copolymers made of polyisoprene, polystyrene and poly(2-vinylpyridine) mixed with a polystyrene homopolymer assemble into a two dimensional columnar structures with dodecagonal symmetry. Previously this system has been shown to form a periodic (3.3.4.3.4) Archimedean tiling structure, with every vertex surrounded by three triangles and four squares (figure 1.18). The transition from periodicity to quasiperiodicity was achieved upon changing the ratio of the three constituents, i.e. change in the ratio of triangles to squares, which

shifted the structure from the Archimedian tiling to a dodecagonal quasicrystal. Numerically, Dotera et al. reproduced this phase using Monte Carlo simulations [50]. The characteristic length in these systems ranges from $10nm$ to $50nm$, i.e. several orders of magnitude greater than the atomic length scales found in metal alloys quasicrystals. Only lately, binary mixtures of inorganic nanoparticles were shown to self-assemble into binary dodecagonal superlattices. These experiments suggest that the formation of quasiperiodicity does not require a unique combination of interparticle interactions, but is a general sphere packing phenomena governed by entropy and simple interparticles phenomena. These results confirm the universal nature of dodecagonal quasicrystals over several hierarchical length scales. The route to the formation of dodecagonal quasicrystals is definitely simplified by the existence of equilateral triangles and squares within a structure but also the existence of two natural length-scales along with three-body interactions may constitute the underlying source of their stability [51].

1.4.2 Artificial quasicrystals

The interest in investigating quasiperiodic order in artificial materials originates from two important features distinguishing them from periodic crystals. The first feature is the ability of producing arbitrarily high rotational symmetries; for periodic crystals the 6-fold symmetry is the maximum achievable. The second feature is the relaxation of any constraints on the positions of Bragg peaks in their diffraction diagrams, a prior condition for the construction of isotropic band gaps in photonic materials [52, 53]. In addition, artificial systems can provide useful information regarding different fundamental aspects in quasiperiodicity such as dynamics of defects or phasons.

In order to measure the photonic properties of icosahedral quasicrystals, Man et al. constructed a photonic quasicrystal with centimetre-scale cells and performed microwave transmission measurements [53]. Although the lattice points in their sample were connected with thin rods, it turned out that such a three dimensional icosahedral quasicrystal exhibits sizable stop gaps and such structures are excellent candidates for photonic bandgap materials.

An example of an artificial system which is used as a model system is the optically induced nonlinear photonic quasicrystal [54, 13]. In this system a certain number of laser beams interact nonlinearly by changing the index of refraction of a photorefractive material. The typical distance between crystal sites is 15μm to 30μm. Here, the dynamics are governed by the so-called nonlinear Schroedinger equation. Taking advantage of the fact that internal wave dynamics can be locally excited and directly imaged, Freedman et al. observed directly dislocation dynamics such as creation and healing as well as structural rearrangements due to phason flips [13].

1.4.3 Feasibility of colloidal quasicrystals

Colloids are micron-scale particles suspended in a liquid. Due to the tunability of the interactions in such systems, a topic that we will discuss in details in the next chapter,

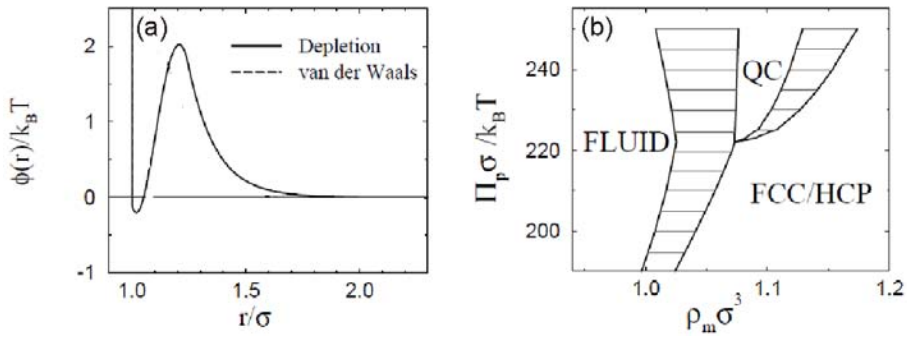

Figure 1.19: Stability of colloidal quasicrystals using thermodynamic perturbation theory. (a) Effective pair potential combining electrostatic repulsion with depletion interaction. (b) Phase diagram of polymer osmotic pressure vs macroion density showing the region where quasiperiodic ordering is predicted. The horizontal lines connect corresponding points on coexistence curves [55].

a rich variety of phases (gas, liquid, crystal, and glass) has been experimentally observed [56]. The quasicrystalline phase was found in a binary mixture of nanometer sized organic particles [49]. Nevertheless, in large micron sized systems, aperiodicity seems to be an exception, since to date it has not yet been experimentally reported. Colloidal quasicrystals, if created, could be used not only as a model system to study fundamental properties of the quasicrystalline phase but also they have a number of potential applications, e.g. photonics since typical length scales are comparable with the wavelength of visible light.

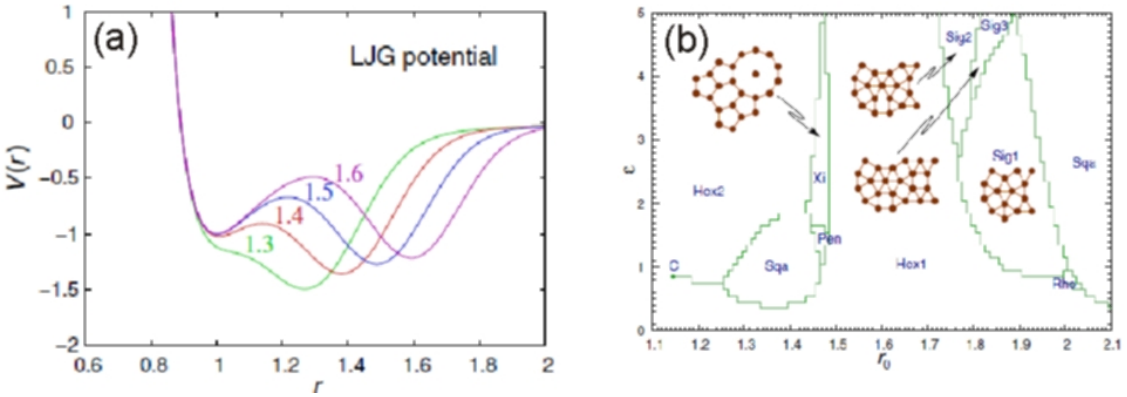

Figure 1.20: Self-Assembly of two dimensional monatomic quasicrystals using double-well interaction potential. (a) Lennard-Jones-Gauss (LJG) potentials for different positions of the second well (r_0). (b) Phase diagram showing the occurrence of four approximants, the decagonal approximant (Xi) and three dodecagonal approximants (sigma phases) [57].

Denton et al. have investigated a one-component colloidal system using thermodynamic perturbation theory and have identified the occurrence and stability of a quasiperiodic phase at certain ranges of packing fractions and polymer osmotic pres-

sures [55]. In their work they have considered an effective pair potential combining electrostatic repulsion with depletion interaction induced in the system by adding non-adsorbing depletion polymers (figure 1.19).

Independently, Engel et al. investigated the occurrence of complex phases, like periodic structures with large unit cells or also approximants [58]. In their two dimensional simulation, they have considered a double well interaction potential between monoatomic particles and observed the self assembly of many phases among them a decagonal, and a dodecagonal quasicrystal (figure 1.20).

Experimentally, such pair-potentials seem to be hard to achieve. Typical depletion potentials usually have for high depletant concentrations a deep first potential well followed by an oscillating part. In order to achieve for instance a decagonal quasiperiodic ordering, it is crucial to set a length scale in the systems related to the golden ratio τ. But, the depth of this first potential cannot be tuned independently from the length scale. That forces the occurrence of a deep well followed by a repulsion barrier leading to rare escapes out of the first minimum. The existence of such a deep well always favors the occurrence of hexagonal crystals with a lattice constant given by the first potential well or glass states rather than aperiodic structures.

CHAPTER 2

COLLOIDS: INTERACTIONS AND PHASE BEHAVIOR

Particles suspended in a liquid are considered to belong to the colloidal domain if their size ranges between several nm and several μm. Because such particles are large enough, the solvent can be described as a continuous and homogeneous background yet they are still small enough that the incessant bombardment of the solvent molecules is sufficient to keep them in motion. Colloids and colloidal principles are widespread in daily life, in nature and technical applications. They have a long history of importance in a broad range of applications in technology and material processing. Used as building blocks for engineering new materials, they found application in high precision filters, controlled porosity substrates or photonic devices [59]. Less well known is that they can illuminate basic physics questions.

Motivated by their potential use as models for atomic systems due to the thermodynamic analogy, the study of colloids is throwing new light on fundamental problems of broad interest in condensed matter physics, statistical physics and other fields of research [60]. Depending on the pair-interaction and the concentration, colloidal systems show analogues of all the states of atomic systems: gas, liquid and solid states. The mesoscopic size (nm-μm), the time scales (ms-s) and the tunability of the pair interaction in colloidal systems make them a convenient model system for experimental and theoretical studies.

Important advances in different experimental techniques, for example, optical video microscopy and confocal scanning microscopy that enable direct observation of individual colloidal particles and also scattering of X-rays, neutrons and light, allow improved measurements and increased understanding of the structure, properties and behavior of colloidal suspensions [61].

In this chapter a short introduction to the basic principles of colloidal physics is given. The fundamental properties of a particle suspended in a fluid is introduced, its motion is characterized and the relevant time scales are defined. Since the focus of this work is the phase behavior of highly charged particles interacting with quasi-periodic light fields in two dimensions, the mechanism of particle-light interactions is

presented. The pair interaction between charged colloids in a solvent is also discussed and the principles of charge screening is introduced. The melting in two-dimensional systems and a brief sketch of the KTHNY-theory are also discussed. Finally, several examples illustrating the rich phase behaviour of colloidal monolayers interacting with strong light field are presented.

2.1 Colloids as model system

Colloidal systems mimic the thermodynamics of atomic crystals [60]. The control of interparticle interactions in colloids gives rise to rich phase behaviours as well as crystal structures with nanoscale and micron-scale lattice spacings [62]. This provides model systems for studying fundamental problems in condensed matter physics, such as the dynamics of crystal nucleation, the nature of the glass transition, melting, and many other examples. The main advantages of such model systems are the experimental accessibility of lengthscales and timescales, and the tunability and control of the interactions. This allows quantitative investigations of phase transitions as well as the creation of advanced materials with novel functionalities and properties.

2.2 Brownian motion, energy distribution and timescales

Colloids are small particles dispersed in a solvent exerting a permanent random motion called Brownian motion. The colloidal thermodynamic analogy with atoms is based on the importance of the Brownian motion which is attributed to the kinetic energy of the fluid molecules. Brownian motion forces the colloidal particles to sample the configuration space efficiently and leads to a velocity distribution obeying the Boltzmann distribution:

$$p(E_{kin}) \propto \exp\left[-\frac{E_{kin}}{k_B T}\right] \tag{2.1}$$

with $k_B = 1.38 \cdot 10^{-23} J/K$ the Boltzmann constant and T the temperature in units of Kelvin.

In the presence of an external potential V(x) the positional distribution becomes (due to equipartition theorem or virial theorem):

$$p(x) \propto \exp\left[-\frac{V(x)}{k_B T}\right] \tag{2.2}$$

The thermal motion makes an important contribution to the total free energy, therefore all energies involved are usually measured in units of thermal energy $k_B T$ rather then in *Joule*. At room temperature $T = 25°C = 298°K$, therefore $1 k_B T$ is equal to 4.115×10^{-21}J.

At timescales longer than the decay time of the velocity autocorrelation function (ensemble average of the product of the velocity at time zero and at time t), the particle's motion is in equilibrium with the solvent and its displacement changes on average proportional to $\sqrt{t}$. This introduces a characteristic timescale called self diffusion time $\tau_D = \sigma^2/6D$ which is the time it takes for a particle to diffuse over its own diameter (σ) in a fluid with a diffusion coefficient D. In our experiments we typically use polystyrene particles with $\sigma = 3\mu m$ in water leading to $\tau_D \approx 0.33s$ much larger than the self diffusion time of atoms ($\approx 1ps$). From these large time scales one can infer that non-equilibrium behavior is accessible in experiments. In order to avoid it, we always made sure to give the system enough time to reach its equilibrium state.

As a consequence, real space analysis by means of video microscopy allows tracking the trajectories of the individual particles and makes the time evolution of the system accessible in detail. Such information is inaccessible in systems investigated by diffraction experiments, as the scattering information is available only averaged over the scattering area.

2.3 Interactions in colloidal systems

Colloidal particles can interact with each other via many types of interaction, for example, long-range electrostatic interactions controlled by the number of charges on the spheres, short-ranged van der Waals interaction and dipole-dipole interaction [62]. And they also interact with external fields such as electromagnetic fields and gravitational field. In the presence of only the steric interaction, i.e. absence of all others, colloids behave like perfect "hard spheres".

The ability of controlling and tuning the interactions gives a major advantage of colloidal systems compared to atomic systems. Most of the interactions stated above can be varied continuously. Magnetic interactions for example can be tuned by applying an external magnetic field which induces magnetic dipoles within the paramagnetic colloids, and the strength of the interaction is proportional to the external magnetic field [63].

In our experiments we use aqueous suspensions of polystyrene spheres with 3μm diameter. They are confined between two horizontally aligned parallel glass surfaces with a spacing of 200 μm. Due to sulfate-terminated surface groups which partially dissociate when they are in contact with water, the suspended particles are negatively charged and experience a partially screened electrostatic repulsion. These dielectric colloids also interact with strong light fields which can be generated by using highly focused laser beams. Accordingly, in the following subsections the colloid-colloid interaction and the colloid-light interaction are presented.

2.3.1 Van-der-Waals Interaction

Especially at small distances ($< 100nm$), the van der Waals (vdW) interaction plays an important role in colloidal systems. The origin of this induced dipole-dipole interaction lies in the instantaneous dipole moment generated by the fluctuation of the electron cloud surrounding the nucleus of electrically neutral atoms. In our experiments these forces can emerge among the colloids or between single particles and the substrate. For different geometries, different analytical expressions for the potential of this interaction were derived by integrating the atomic dipole-dipole interaction [64]. In the case of two spherical particles it is given by:

$$V_{vdW}(r) = -\frac{Aa}{6}\left(\frac{2a^2}{r^2-4a^2}+\frac{2a^2}{r^2}\right)-\frac{A}{6}\ln\left(\frac{r^2+4ra^2}{r^2}\right), \tag{2.3}$$

where a ($a = \sigma/2$) is the radius of the sphere, r the center-to-center distance of the particles and A the Hamaker constant. For particle-wall geometry:

$$V_{vdW}(r) = -\frac{Aa}{6}\left(\frac{1}{r}-\frac{1}{r+h}\right)-\frac{A}{6}\ln\left(\frac{r}{r+h}\right), \tag{2.4}$$

with h the thickness of the wall and r the particle-wall distance. The Hamaker constant is given by:

$$A = \frac{3k_BT}{4}\left(\frac{\epsilon_1-\epsilon_3}{\epsilon_1+\epsilon_3}\right)\left(\frac{\epsilon_2-\epsilon_3}{\epsilon_2+\epsilon_3}\right)+\frac{3h\nu_e}{8\sqrt{2}}\frac{(n_1^2-n_3^2)(n_2^2-n_3^2)}{\sqrt{(n_1^2+n_3^2)(n_2^2+n_3^2)}\left[\sqrt{n_1^2+n_3^2}+\sqrt{n_2^2+n_3^2}\right]}, \tag{2.5}$$

where n_1, n_2 and n_3 are the refractive indices of the particle, substrate, solvent respectively and ϵ_1, ϵ_2 and ϵ_3 are the corresponding dielectric constants. υ_e is an effective resonance frequency for electronic excitations. Some values for the Hamaker constant for typical material combinations are listed in [65].

This equation shows that when the refractive indices of the substrate (or particle) and the solvent have the same value, the vdW forces vanish because $n_2^2 - n_3^2 = 0$. In our system (described later) the Hamaker constant will always be positive and the vdW interaction will always be attractive.

In order to avoid any aggregation of particles or irreversible sticking on the substrate our suspensions are almost always stabilized by means of a repulsive interaction, i.e. typical distances between the particles and the substrate and also among the particles are always much larger than 200 nm. This repulsive pair interaction arises in charged colloidal suspensions and will be described in the next section.

2.3.2 Electrostatic Interaction

In contact with a polar solvent (e.g., water, DMF,...), polystyrene particles and glass surfaces acquire a negative surface charge density. The principle mechanism for that

is the dissociation of surface groups. In the case of sulfonate end-groups, typical for the polystyrene particles, a proton is transferred between the colloid and the solution:

$$X - SO_4H \rightarrow X - SO_4^- + H^+$$

Whereas for glass surfaces, the ionization process is established through the dissociation of terminal silanol groups:

$$X - SiOH \rightarrow X - SiO^- + H^+$$

X symbolizes the rest part of the colloid matrix.

The degree of these processes is related to the H^+ ions present in the solvent given by the pH value. As a consequence, the electrostatic interaction in our system among the particles and between a particle and the substrate is repulsive. Furthermore, counterions left from the dissociation process form an electrical cloud near the surfaces of the particle and the substrate. This charged zone is called double layer. The double layer consists of an inner region of counterions strongly attached to the surface and a diffuse region containing the excess of counterions. The double layer leads to a damping in the electrical field known as electrostatic screening. In fact, free ions reduce the overall amplitude of the Coulomb interactions and change the shape of the potential energy, making it decay exponentially to zero with a characteristic distance called the Debye screening length. A rough derivation of this will be given in the following.

Assuming that the surface charge is continuous and uniform and that the ions in the solution can be treated as point charges we can express the ion concentration using the Boltzmann distribution function:

$$n_i = n_{i0}\, exp\left(-\frac{Z_i e\phi(r)}{k_B T}\right), \tag{2.6}$$

where n_i is the concentration of ions of kind i at a point where the electrical potential is $\phi(r)$; n_{i0} is the concentration in the bulk of the solution; Z_i is the valency for cations and anions. The sum of both charge density distributions of the cations and anions in the solution is then given by:

$$\rho(r) = \sum Z_i\, e\, n_i = \sum Z_i\, e\, n_{i0}\, exp\left(-\frac{Z_i e\phi(r)}{k_B T}\right), \tag{2.7}$$

The electrostatic potential $\phi(\overrightarrow{r})$ is related to the charge density distribution $\rho(r)$ by the Poisson equation:

$$\nabla^2\left[\phi(r)\right] = \frac{\rho(r)}{\varepsilon k_B T}, \tag{2.8}$$

where ε is the dielectric constant of the solvent.

Combining 2.7 and 2.8 gives the Poisson-Boltzmann equation which is a differential equation for the potential as a function of the coordinates:

$$\nabla^2 [\phi(r)] = \frac{1}{\varepsilon k_B T} \sum Z_i \, e \, n_{i0} \, exp \left(-\frac{Z_i \, e\phi(r)}{k_B T} \right), \tag{2.9}$$

Equation 2.9 has no exact analytical solution. To simplify the problem one would consider the special cases:

- small surface potential $\rightarrow Z_i exp \left[\frac{\phi(r)}{k_B T} \right] \ll 1$, allowing linearization of equation 2.9
- a symmetrical electrolyte

In the so-called Debye-Hückel approximation the exponential is expanded and, only the second term of the series is retained which leads to the linear equation:

$$\nabla^2 [\phi(r)] = \kappa^2 \phi(r), \tag{2.10}$$

where

$$\kappa = \sqrt{\frac{e^2}{\varepsilon k_B T} \sum n_{i0} Z_i^2}, \tag{2.11}$$

The associated length κ^{-1} is the Debye length. In our experiments it varies from about 1 to 300 nm. The summation in equation 2.11 is proportional to the ionic strength of the solution. The solution $\phi(r)$ of equation 2.10 describes the potential for the point charges and through equation 2.8 the ions distribution. Based on the knowledge of $\phi(r)$ the particle-particle potential V(r) can be calculated and yields the following expression:

$$U(r) = \frac{(Z^* e)^2}{4\pi \varepsilon_0 \varepsilon_w} \left(\frac{\exp(\kappa a)}{1 + \kappa a} \right)^2 \frac{\exp(-\kappa r)}{r}, \tag{2.12}$$

The pair interaction is the electrostatic part of the Derjaguin-Landau-Vervey-Overbeek (DLVO) theory [66] called screened Coulomb potential. It is proportional to the square of the charge of the particle and decreases exponentially with distance $\frac{\exp(-\kappa r)}{r}$. The prefactor depends on the radius of the particle a, the effective surface charge Z*, the vacuum permittivity $\varepsilon_0 = 8.85 \cdot 10^{-12} As/Vm$, and the permittivity of water $\varepsilon_W = 81$. e is the elementary charge ($e = 1.6 \cdot 10^{-19} C$) and r the center to center distance.

Experimentally, the Debye screening length is a tunable parameter because it depends on the molarity of the aqueous solution in the sample cell (figure 2.1). The range of electrostatic interaction is different for different salt concentrations. The increase in ion concentration leads to a screening of the electrostatic repulsion which brings the particle closer to each other. The slope of the repulsive part of the

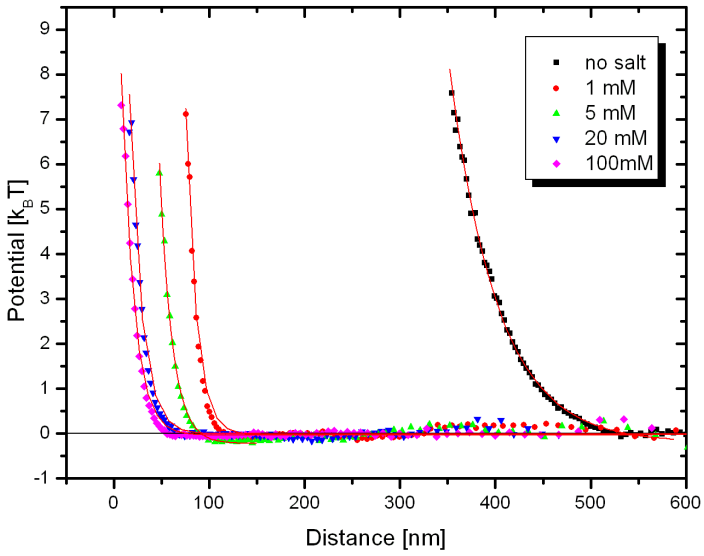

Figure 2.1: Electrostatic part of the interaction potential measured with TIRM between a colloidal particle ($a = 1,8\mu m$) and a plain substrate for salt concentrations (ions) up to 100 mM. Solid lines are first order exponential decay fits [67].

potential increases and the decay length, which corresponds to the Debye screening length, becomes smaller indicating screening on a shorter length scale.

A direct measurement of U(r) is possible by measuring the distance probability distribution of two colloidal particles using digital video microscopy [68]. For dense and highly charged colloidal systems many-body effects are encountered [69]. The pair interaction is directly related to the overlap of the double layers which can extend over large distances. Once, more than two particles are close enough to be within the range of the double layer, many-body interactions arise and deviations from pairwise additive interaction energies are expected. In such a case, the effective $colloid - colloid$ pair potentials can be extracted by means of inversion routines based on the $Ornstein - Zernike$ equation or the inverse Monte Carlo method [70]. These standard inversion procedures determine U(r) by inverting the pair distribution function g(r) of semi-dilute suspensions.

2.3.3 Gradient forces and light pressure

Optical tweezers is a powerful and yet quite useful technique to move and control mesoscopic particles. Using light forces one can trap and levitate micron sized colloidal particles without the prerequisite that they are charged or magnetic. The only necessity is that the particles should have a refractive index different than the index of refraction of the embedding fluid and that they are transparent at the wavelength

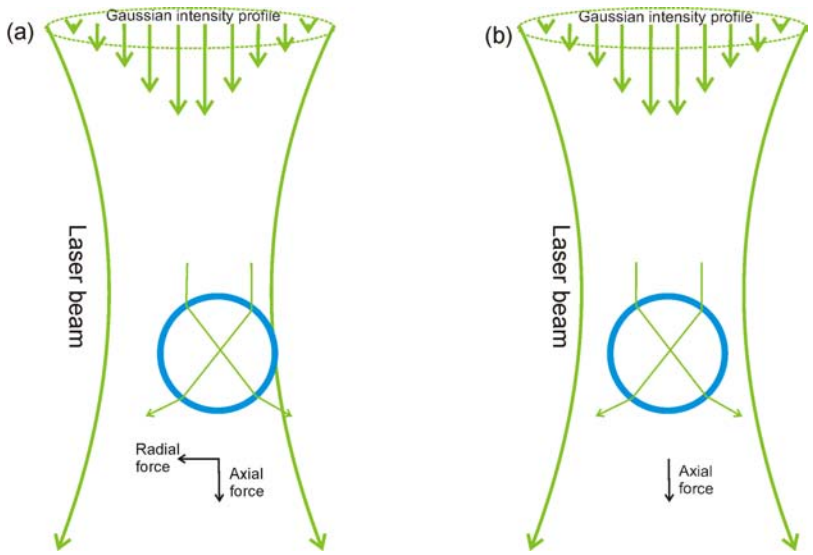

Figure 2.2: Illustration of the origin of the light forces acting on a microsphere in the vicinity of a focused gaussian laser beam. (a) For a particle located near the focus, both axial (scattering force) and radial (gradiant force) forces take place. (b) Once the particle reaches the focus, the radial force cancels and only the axial force acts on it.

of the laser light to avoid thermal effects. This tool was introduced in the early 70s by Arthur Ashkin and his co-workers [71].

Optical traps have found application in many fields of physics and biology. In addition to their use in colloid science, scientist have found that with optical tweezers one can cool neutral atoms [72, 73] or manipulate biological systems. The strength of these light forces acting on typical colloidal probe particles is in the range of some femto to pico Newton.

A three dimensional optical trap is formed when a laser beam is tightly focused with an objective lens of high numerical aperture (NA). The forces acting on the particle that is trapped in the focus, are due to the momentum transfer from the scattering incident photons. These forces are decomposed into two components, a gradient force, acting in the direction of the light gradient (radial force) and a scattering force acting in the direction of the light propagation (axial force). In the following, the origin of the gradient force and the radiation pressure are discussed.

Gradient forces

For particles, with size much smaller than the wavelength of the used monochromatic source ($\sigma \ll \lambda$), the operation of optical tweezers can be explained by using an electromagnetic approach. For $\sigma \gg \lambda$ it can be explained by a momentum transfer associated with the reflection and refraction of light. In the electromagnetic approach the electric field of the incident laser beam polarizes the particle and induces a dipole

moment $\vec{P}$. $\vec{P}$ is proportional to the electric field $\vec{E}$ and the total energy of the induced dipole in the field is:

$$U = -\vec{P}\vec{E} \propto -\vec{E}\vec{E} \propto -I \tag{2.13}$$

where I is the intensity. The energy of the particle is minimized where the intensity is a maximum. For a focused light beam with a gaussian intensity distribution the intensity maximum is at the focus. The particles are then attracted into the region with the highest electric field, i.e. highest laser intensity. Since the potential is proportional to -I, the associated force is proportional to ∇I. This is the gradient force which is responsible for the trapping.

For very large particles, the calculations are based on a vectorial summation of the contributions of single rays which are reflected and refracted by the particle. For a dielectric sphere with refractive index greater than the surrounding medium, one should consider the momentum change between two incident rays and their first reflected and refracted rays, respectively. This results in a force dragging the particle towards the focus of the rays. The predicted force is independent of the particle size, and usually agrees with experimental results for $\sigma \geq 10\lambda$ [74].

The theoretical calculations applicable for $\sigma = 3\mu$m and $\lambda = 532nm$ (intermediate regime corresponding to our experiments) were developed by Tlusty et al. who showed that the dipole approximation is valid for any particle size [75]. In the electromagnetic approach, one decomposes the fields into plane waves and the interaction is determined by a sum over the entire volume of the particle. They used an approach based on the strong localization of the fields where the main contribution to the interaction arises from the steep variations in the amplitude of the fields. This strongly reduces interference effects and renders this approach applicable to particles of any size. The force is expressed as the change in the dipole interaction with respect to the change of the particle's coordinates. The dipole interaction energy of the particle is given by [75]:

$$U = -\alpha \int I dV \tag{2.14}$$

with $\alpha = \frac{\epsilon_p}{\epsilon_0} - 1$, accounting for the relative difference of the dielectric constants of the particle (ϵ_p) and the surrounding medium (ϵ_0) and V the volume of the particle. The optical gradient force is then given by the change of U in response to a change of the particle's coordinates.

Light pressure

The scattering of light by the particle results in another force usually referred to as radiation pressure which drives the particle along the direction of propagation of the light. This radiation pressure is due to the momentum transfer between scattered photons and scattering particle. The momentum of a propagating laser beam G is proportional to the energy E and inverse proportional to the velocity of light v ($G = E/v$). When the beam hits the interface between the medium and the particle

(optically different media), a reflected and transmitted beam will be produced. The combined momentum of these two beams will differ from that of the incident beam and to satisfy the conservation of momentum a force is exerted on the interface. The magnitude of the radiation pressure depends on the sizes of the beam and the particle, the wavelength of incident light, and the refractive indices of both the sphere and surrounding medium and it scales like [75]:

$$F_{scat} \cong 2\pi\alpha^2 I w^2 \tag{2.15}$$

where w is the beam waist.

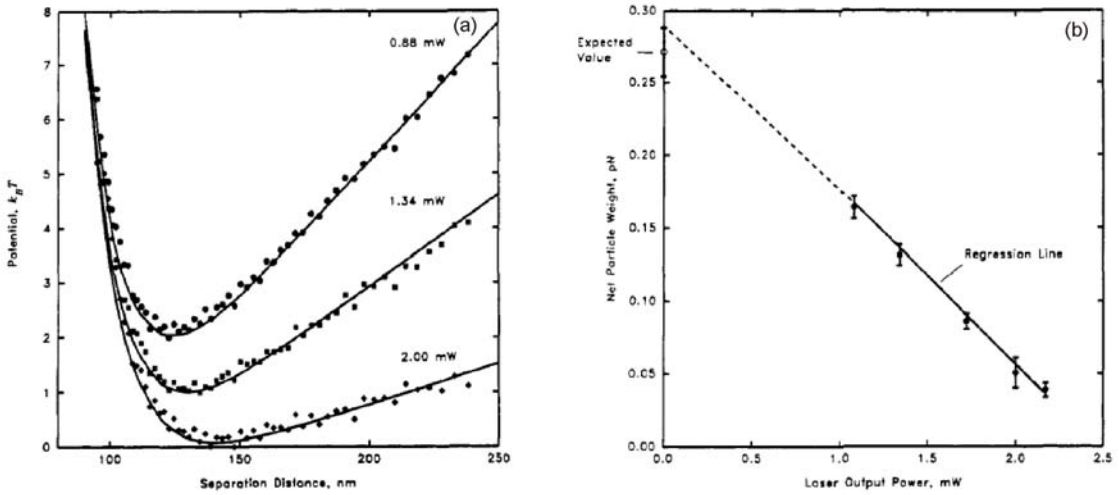

Figure 2.3: (a) Potential energy profiles measured from a 10 μm polystyrene sphere in a aqueous solution at three different levels of radiation pressure acting against gravity. (b) Net weight of the particle as a function of output power of the laser beam [76].

Walz et al. used a highly sensitive technique, Total Internal Reflection Microscopy (TIRM), to measure the radiation force acting on a single microscopic sphere suspended in an aqueous solution next to a wall. Due to Brownian motion the sphere diffuses around an equilibrium position. By monitoring the separation distances between the particle and the wall, a histogram of elevations is measured and a probability density is deduced. This is then converted to a potential energy profile using Boltzmann's equation. Typical potential energy profiles show a repulsive part due to an electrostatic interaction and an attractive part resulting from the gravitational force (figure 2.3). Using a radiation pressure acting on the particle from below, the net weight of the particle can be changed. Here, a 50 mW argon ion laser ($\lambda = 514.5nm$) was used to form the radiation pressure beam striking the particle from below and by that reducing the net weight of the particle. At various laser output levels, the potential profiles were measured and by subtracting the real weight of the particle the radiation pressure was measured. Typical values range between fN to pN. In the experiments that will be described later, a broadened laser beam ($\lambda = 514nm$) is adjusted to

be vertically incident on the sample cell from above pushing the colloids towards the negatively charged substrate and reducing the vertical particle fluctuations to less than 5% of the particle radius. This increases the two dimensional confinement without playing any other role.

2.4 Melting of colloidal crystals in two-dimensional systems

Melting is an active research field in solid-state physics and in numerous domains. Three dimensional melting occurs via a first order transition when the thermal vibrations of atoms make them collide with each other. In contrast the two dimensional counterpart is predicted by the theory developed by Kosterlitz, Thouless, Halperin, Nelson, and Young (KTHNY) to occur via two sequential defect-driven continuous phase transitions [77, 78]. The origin of this fundamental difference lies in the fact that two dimensional lattices do not display true long range translational order at finite temperatures (Mermin-Wagner theorem) [79]. This is also reflected by the density-density correlation function which decays algebraically to zero with distance in a two dimensional crystal, and reaches a finite value in the three dimensional case.

The KTHNY theory is based on fundamental properties of a two dimensional crystals and do not depend on the specific pair-interactions. Therefore it is expected to hold for any two dimensional system. There are several experimental systems such as liquid crystals and Langmuir-Blodgett films which allow the investigations of the two dimensional melting. Nevertheless, thin colloidal suspensions are better suited because they allow direct observation of topological defects [80, 81]. Uniform paramagnetic colloidal microspheres dispersed at a water-air interface proved to be an excellent model system to test the KTHNY theory. Such particles have a Fe_2O_3 core and the presence of an external magnetic field H perpendicular to the interface induces a magnetic moment M proportional to H. This leads to a repulsive dipole-dipole interaction proportional to M^2/r^3, where r is the particle-particle distance. The strength of the interaction could be considered as inverse the effective temperature. By varying the strength of the magnetic field the effective temperature is changed and the phase behavior of the particles is monitored in real space by means of video microscopy.

These experiments showed that a monocrystalline system melts in two stages (figure 2.4). Near the melting temperature, dislocation pairs disturbing the local ordering are observed by looking at the number of nearest neighbors of each particle by means of Delauney-triangulation. Four particles lose their six-fold coordination and instead two five- and seven- fold coordinated pairs appear. This pair is called a dislocation which disturbs the translational order but not the orientational order. Such defects are usually described by means of the Burger vector. At higher temperatures, the dislocation pairs can dissociate, diffuse in the crystal and form an intermediate hexatic phase characterized by a discrete orientational symmetry. Increasing the

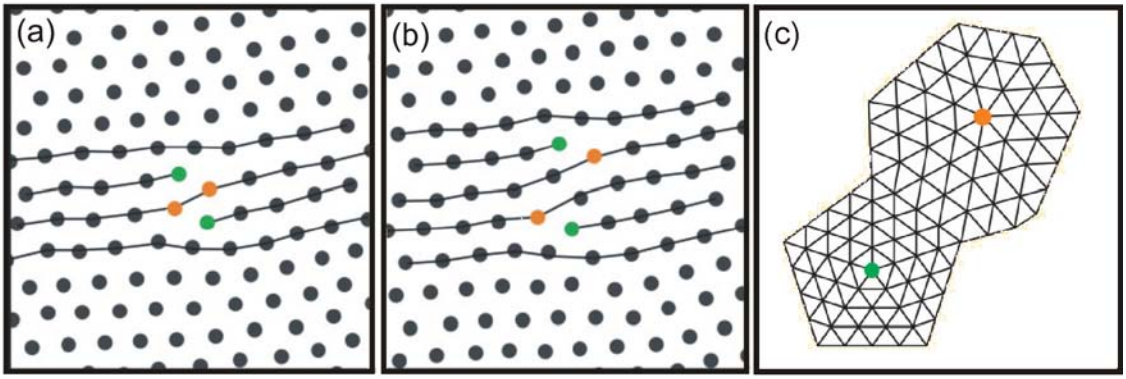

Figure 2.4: Melting of a two dimensional colloidal crystal. (a) Hexagonal crystal with a dislocation pair at low temperature. Particles with five nearest neighbors are colored in green, with seven in orange. (b) At high temperatures the pair can dissociate. (c) Increasing the temperature furthermore, leads to the formation of disclination and consequently to a transition to the isotropic fluid phase [82].

temperature once again can lead to a second transition to the isotropic liquid phase. In this transition the orientational order is disturbed. This is due to the formation of a second type of defects called disclinations. The thermal energy divides the dislocation in a isolated five- and seven- coordinated particles diffusing away from each other. Both first and second transitions are supposed to be continuous phase transitions.

Similar phase behavior was lately reported for an out-of-equilibrium two dimensional crystal of Ferrofluid Spikes [83]. Here also an intermediate hexatic-like phase between the solid and isotropic liquid phases is reported with a melting transition occurring for a critical spike displacement called the Lindemann criterion (10% of the interatomic distance). This and other examples (liquid films, vibrated granular monolayers and vortex lattices in superconductors) give an indication that such behavior is universal.

2.5 Phase transitions on light substrates

In the previous section only the pair-interactions within the system where taken into account. But, two dimensional real systems are usually subjected to potential landscapes. This confinement can be for example a solid crystalline substrate. Accordingly, the phase behavior depends on many properties of the underlying substrate potential. In the case of a crystal, the substrate atoms provide a laterally modulated potential for two dimensional adsorbates. The interplay between the particle-particle interactions and the particle-substrate interactions leads to more complex behavior [25].

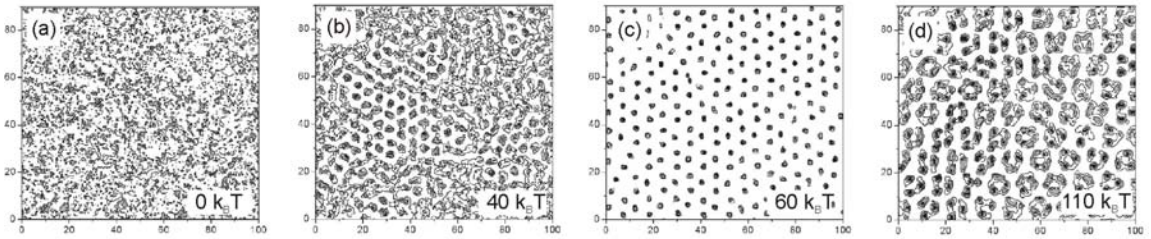

Figure 2.5: Phase behavior of colloidal trimers on a triangular light lattice. (a) Spatially resolved average particle density $\rho(x, y)$ in the absence of the lattice ($0k_BT$) showing the occurrence of a liquid state. (b) At $40k_BT$ the particles start to interact with the substrate potential and the density distribution is no longer homogeneous. (c) Localization of the particles is observed at $60k_BT$. (d) Melting of the orientational order at $110k_BT$ [84].

Highly charged trimers on a triangular substrate potential, for example, have a different phase behavior compared to similar systems interacting with homogeneous substrate potentials. Brunner et al. investigated the phase behavior of such systems by creating an extended triangular interference pattern and adjusted the particle density to three particles per minima by means of optical tweezers [84]. In addition to the postional order, these trimers possess a high degree of orientational order. At a laser power corresponding to a potential depth of $60k_BT$, crystallization and regions with two main orientations were observed (figure 2.5). Increasing the power leads to the growth of one orientation at the expense of the other. When the substrate strength was increased to $110k_BT$, an enhanced positional order occurred. However, the orientational order of the trimers became much weaker. This orientational melting is due to the increase of the radial pressure on the trimers and therefore reduces their mean extent and the lateral fluctuations leading to a reduction of the trimer-trimer interaction.

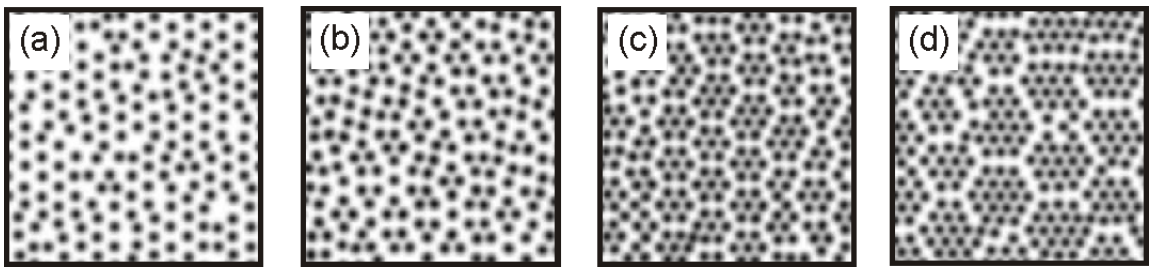

Figure 2.6: Phase behavior of colloidal particles in a triangular light field with potential strength $6.9k_BT$ for filling factors $\eta = 0.34$ (a), 0.48 (b), 0.59 (c) and 0.69 (d). The snapshots are artificially defocused to enhance the visibility of the domain walls [85].

Colloidal monolayers on periodic light substrates have shown to be a good model system for adsorbed atoms on highly ordered surfaces. For instance, the same phase behavior of Xe atoms adsorbed on graphite surfaces was also observed in colloidal monolayers subjected to a triangular substrate [85, 86]. Upon variation of the particle number density a transition from a homogeneous phase to a network of pronounced domain structures was observed (figure 2.6). Because in a colloidal system there is direct access to real space information, the strength and nature of the different interactions, the origins of the transition which is the elastic strain between the adsorbate and the substrate could be identified.

Lately, due to the high interest in investigating quasiperiodic systems Schmiedeberg et al. used Monte Carlo simulations and the Landau-Alexander-McTague theory to study the freezing and melting of a colloidal adsorbate on one dimensional quasiperiodic substrates [87]. They have found that in this case, colloids order in triangular and rhombic periodic phases at low potential strength. By an increase of the strength of the potential, a new type of light-induced melting is observed having its origin in the aperiodicity of the substrate potential. The quasicrystalline substrate melts the crystalline phases even when they already exist at zero potential.

In conclusion, these examples are presented to demonstrate the rich phase behavior of colloidal suspensions interacting with two-dimensional substrate potentials. This proves that colloids provide ideal conditions for experimental and theoretical studies and serve as good model system to investigate the structural behavior of adsorbates in the presence of structured substrates.

CHAPTER 3

EXPERIMENTAL REALIZATION OF TWO-DIMENSIONAL COLLOIDAL QUASICRYSTALS

Colloidal monolayers exposed to periodic light fields show a phase behavior totally different from that of two-dimensional systems on homogeneous substrates. In this chapter we show how colloidal quasicrystals with different symmetries can be created in the lab (Fig. 3.1). By overlapping five or seven coherent laser beams, quasiperodic potential substrates with decagonal or tetradecagonal symmetry are created. Highly charged colloidal suspensions are prepared by appropriate deionization of the aqueous suspension. Using scanned laser tweezers and thermophoretic effects, two-dimensional colloidal monolayers are created with highly precise density control. Digital video microscopy and image processing techniques are implemented in order to track in real space the particle position relative to the substrate potential landscape. The length scales, the potential depth distributions, and the strain fields of the substrate potential are characterized. Finally, the ordering of charged colloidal particles on such substrates is presented.

3.1 Sample cell and deionization circuit

The amount of dissolved ions in the water suspension is a crucial parameter influencing the electrostatic interaction acting on charged stabilized colloidal particles. At very high salt concentrations, the pair-potential is hard-sphere like and the particles can come very close to each other. In this case, the van-der-Waals interaction can lead to irreversible sticking. Therefore, it is necessary to keep the ion concentration in the sample cell as low as possible. The Debye screening length κ^{-1} depends on the concentration of all dissolved ions n_{i0}:

$$\kappa = \sqrt{\frac{e^2}{\epsilon k_B T} \sum n_{i0} Z_i^2} \tag{3.1}$$

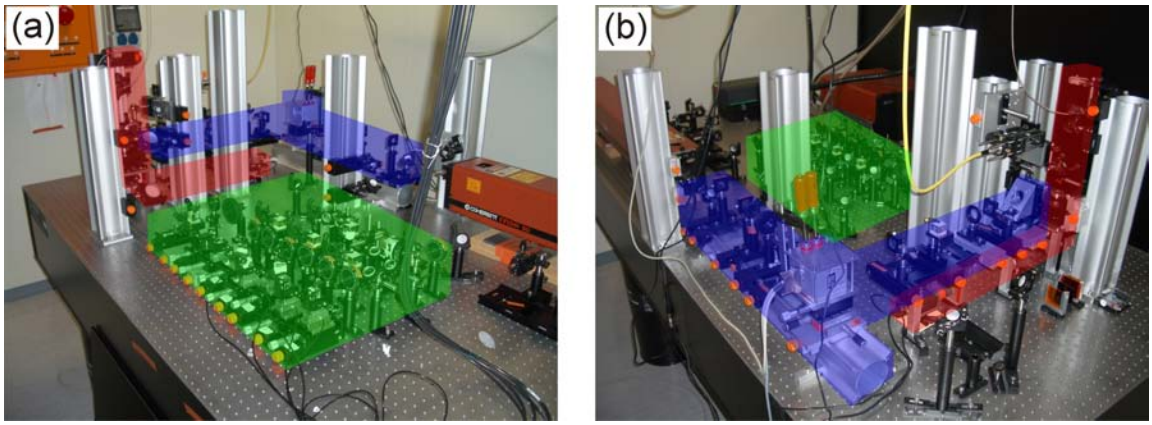

Figure 3.1: Pictures of the experimental setup taken from two different perspectives (a-b). The different optical elements and the lasers are set on a optical table. The spatial ordering is highlighted using three colors: green, blue and red. The optical components belonging to the interferometer are located below the green box. The scanned optical tweezers are highlighted in blue and the red path corresponds to the optical components of the video microscopy. In addition, a fiber coupled infrared laser (seen in b) is focused in the sample cell from above (yellow fiber) and the optical path of the pressing down tweezers is set next to the interferometer.

For increasing κ^{-1}, the range of the interaction also increases. In order to reach high values of κ^{-1}, we inject the colloidal particles in the experiments in a silica cuvette (Fig.3.2). In such a sample cell highly deionized dense colloidal systems can be prepared. The cuvette is commercially available and has an inner height of 200 µm (QS-137, Hellma, Germany). Therefore the flow resistance is low, and the cuvette can be connected to a closed circuit for continuous deionization of the water solvent [88].

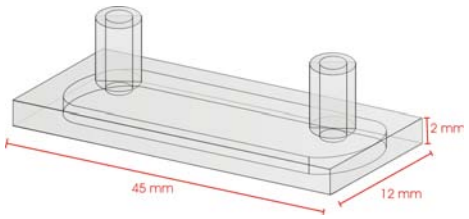

Figure 3.2: Silica cuvette used in the experiments as sample cell. It is commercially available from *Hellma* with a inner height of 200 µm.

The deionizing circuit consists of vessels and tubes made of Plexiglas, Teflon, and Tygon, materials that poorly contaminate the solvent with additional ions. As described in Fig. (3.3), the sample cell is connected to a water reservoir connected to a stream of nitrogen. This stream ensures that the dominant ionic contamination of the circuit, CO_2^- ions, are not dissolved into the water of the reservoir. The tubing connecting the cuvette to a conductivity measuring vessel is attached to a peristaltic

pump. In the measuring vessel an electrode is inserted to monitor the conductivity of the water σ. After twenty to thirty minutes of continuous deionization a conductivity of 0.06 μS/cm can be reached. Due to the self dissociation of water the lowest possible value is $\sigma_{water} = 0.55$ μS/cm (3.2).

$$2H_2O \rightleftharpoons H_3O^+ + OH^- \tag{3.2}$$

The water is then pumped through a container filled with ion-exchange resin which promotes the desalination of the system. Two small and fine nets prevent the inflow or outflow from the vessel of the resin granules into the circuit. The colloidal suspension is also deionized before pumping it into the sample cell. This procedure consisted in mixing the suspension with highly deionized water, centrifuging, removing the water above the sedimented particles, and replacing it once again by highly deionized water. It can be repeated several times. Then the colloids are injected into the circuit via the water reservoir and pumped into the sample. The sample cell is finally sealed with clamps. The high quality of such sample cells is previously checked by measuring the increase of the inverse Debye screening length. It showed that κ increases by approximately 17 $\mathrm{nm}^{-1}\mathrm{hour}^{-1}$. This corresponds to a small diffusion rate of 6.5 nMol/hour [89]. The screening length for dilute systems is determined by inversion of the pair correlation function $g(r)$ and evaluation of the pair interaction $u(r)$ using a closure relation [90].

3.2 Density adjustment

For phase transitions in general and the experiments that will be described later, a precise control of the density of the colloidal system is crucial. Before applying the quasiperiodic potential (described later), the density of the particles in the field of view has to be adjusted. In order to avoid high concentrations of counterions, the amount of particles pumped in the sample cell is much lower than the amount needed for the required high densities in the field of view. The latter is increased in the field of view by inducing convection flows in the sample cell using a fiber coupled infrared laser with a wavelength of $\lambda = 1070$ nm and maximum output power $P_{max} = 5$ W (IPG). The combination of the toroidal convection flow lines and a laser tweezer suppressing the vertical fluctuations (later described in details) leads to the formation of a circular monolayer in the field of view on the lower surface with a diameter of about 500 μm (Fig. 3.4). After reaching the desired particle density, the infrared laser is turned off and the water temperature cooled down until it reached the lab temperature (about 300 K).

The high particle density is kept constant using a scanned optical tweezer ($\lambda =$ 488 nm, $P_{max} = 7$ W). Around the central region of the system, the laser is set to form a boundary box. This also allows to create well defined boundary conditions for our measurements. A focused laser spot is deflected by a galvanometer scanner to draw a circular corral in the sample cell.

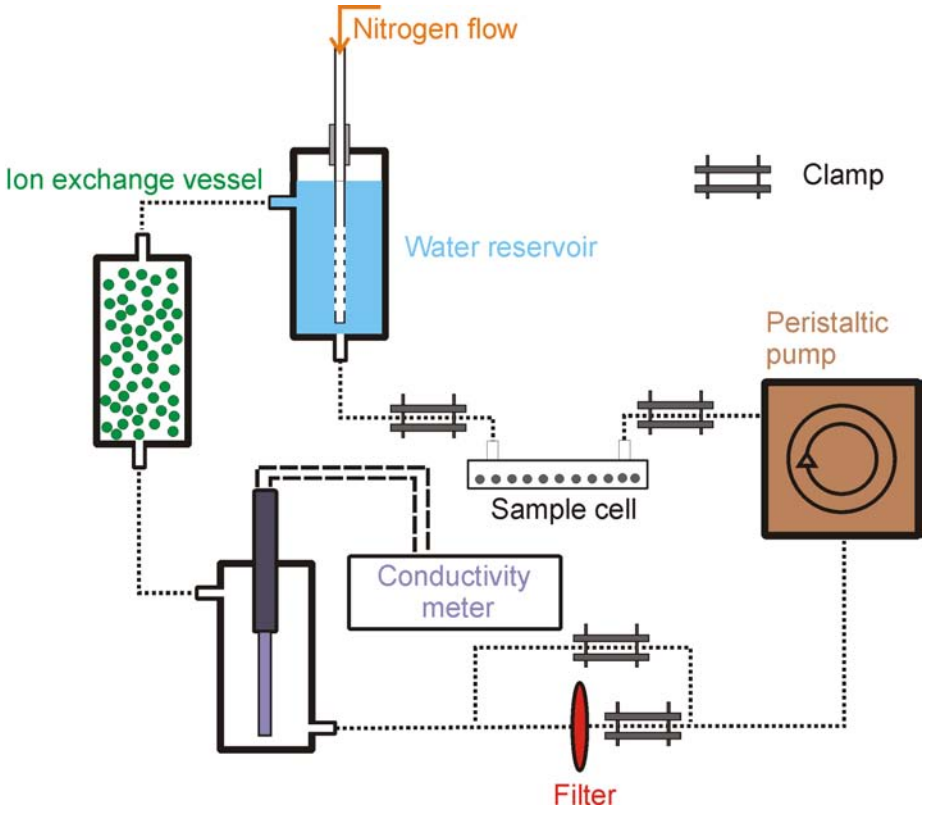

Figure 3.3: Scheme of the deionization circuit. The water is pumped through a vessel filled with ion-exchange resin and the conductivity σ is monitored via a conductivity meter.

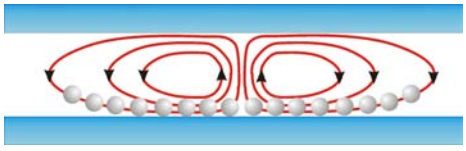

Figure 3.4: Theoretically predicted flow lines in a vertical cross section due to temperature gradients. In combination with pressing down tweezers, this leads to very high particle concentrations in the field of view at the lower surface of the sample cell [91].

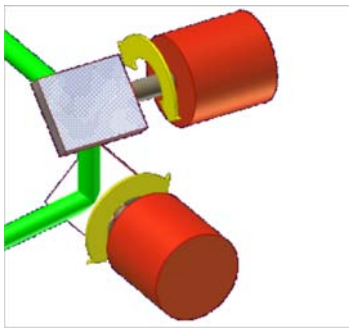

Figure 3.5: Two-dimensional scan system. It includes two galvoscanned mirrors set perpendicular to each other deflecting the laser beam.

The beam of an Argon-Ion laser (Innova 90, $\lambda = 514\,\text{nm}$, Coherent, USA) is deflected by a two axis galvanostatic driven mirror system (SCANcube, Scanlabs, Germany) (Fig. 3.5). It is able to deflect the outgoing beam within a range of $\pm 0.35\,\text{rad}$, with frequencies up to 200 Hz, and has a very small long-time drift. The control of the scanning velocity, step size, and scan shape is executed using a home written program. It allows drawing patterns with different shapes, such as circles, ellipses, rectangles and triangles. After the scanning system, the deflected beam is collimated by a beam expander and projected onto the back aperture of a long-distance microscope objective (Nikon, 20x, NA=0.4, WD=24mm)(Fig. 3.6). Scanning the beam leads to a fast motion of the focus (trap) in the focal plane which is adjusted to be in the sample cell. The focused beam is coupled to the sample cell by a dichroic mirror (BSP488/514) to enter the sample cell from the top and without blocking the lattice-forming laser beams. The spot size of the laser tweezers inside the sample cell is comparable to the size of the used particles (about 3 μm). The repetition rate of the pattern is much faster that the relaxation time of the particles, and the trap is considered to be quasi-static. Its potential depth is increased ($> 20\,k_BT$) until the particles cannot escape from the trap. Another feature is also implemented in the controlling program, allowing a continuous and slow change of the size of the corral. With this feature very precise real time control of the density is possible.

In addition to the scanned-tweezer manually controlled tweezers are also implemented. This provides a convenient method for dragging out of the field of view coagulated or large particles.

3.3 Two-dimensional confinement

Using the above discussed scanned optical tweezers, it is possible to increase the system density and, it is also possible to define the system boundaries (Fig. 3.7). However, this does not lead necessarily to two-dimensional confinement of the system. One way to reduce the out of plane thermal fluctuations is the use of thin sample cells.

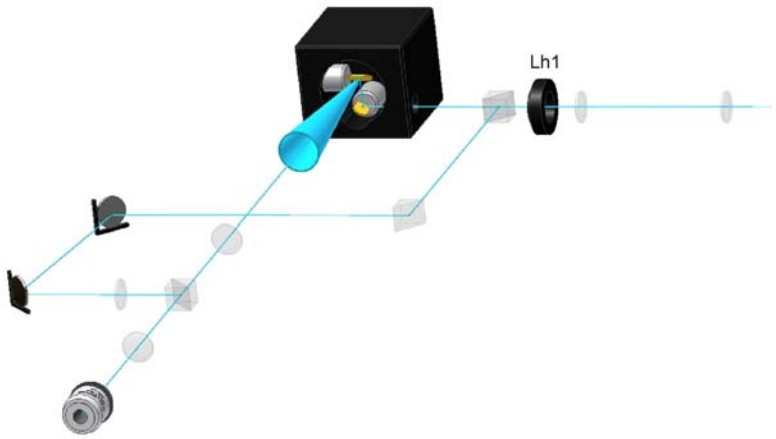

Figure 3.6: Scanned laser-tweezers setup. The beam is deflected by a scanning system. The change in the incident angle on the rear aperture of the microscope objective leads to a motion of the focus inside the sample cell, and creates a corral keeping the density of the particles in the field of view constant. In addition, in front of the scanning system a polarizing beam splitter is placed in order to create manually controlled tweezers.

In this case the confinement of the colloidal system is achieved geometrically; i.e. the spacing between the two glass plates of the cell should be slightly larger than the particle's diameter. Nonetheless, in such thin sample cells high levels of deionization of the suspension cannot be reached and strong pair interactions cannot be achieved. Instead, we use the light pressure of an incident laser beam to confine the particles. The system is regarded two-dimensional, when the out of plane fluctuations of the particles are orders of magnitude smaller than their in plane movement.

Due to the difference between the density of the polystyrene particles ($\rho_{PS} = 1.05\text{g/c}$) and the aqueous suspension ($\rho_{H_2O} = 0.998\text{g/cm}^3$), the particles sediment to the bottom plate of the cell due to gravity,

$$F_G = \frac{4}{3}\pi r_K^3 g(\rho_{PS} - \rho_{H_2O}). \tag{3.3}$$

For the particles used in the experiments this force is estimated to be about 30 fN. Near the wall, the repulsive electrostatic force acting on the particles arises from the overlapping double layers. The gravitational force alone is not enough to suppress the out of plane fluctuations. Due to the thermal energy, the particle fluctuations perpendicular to the wall are in the order of their diameter (about 3 μm). Therefore, this motion must be suppressed by the radiation pressure of a laser beam.

In this setup, we use the vertical light pressure of an incident Argon-Ion beam to confine the particles into a two-dimensional plane. For high laser intensities, the light pressure is in the order of hundred picoNewton and the out of plane fluctua-

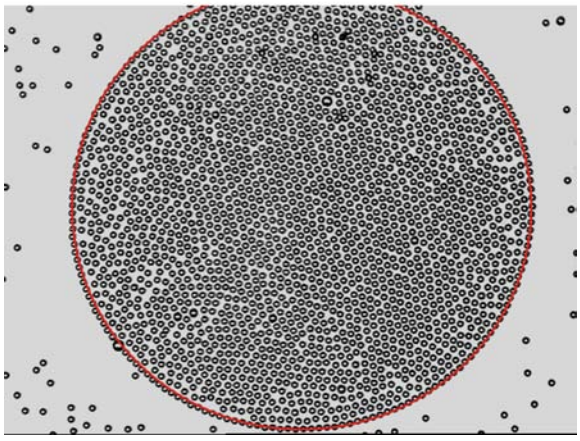

Figure 3.7: An optical tweezers is scanned along a circle in the sample plane trapping the colloidal particles (red). It serves as a boundary box for the system. With the help of manual optical tweezers coagulated particles can be removed from the region of interest.

tions become smaller than 200 nm, which is less than 2 % of the particle radius. Consequently, the system can be regarded as two-dimensional.

3.4 Digital video microscopy and data acquisition

The typical size of the colloids used in this experiment is in the micrometer range. The time which it takes for a particle to diffuse over its own diameter (self diffusion time) is in the order of a second. For such large size and time scales, it is possible to directly observe the system using digital video microscopy. To image the colloidal particles and simultaneously the interference pattern, we use a long working distance (WD) microscope objective from the company Nikon (WD = 24 mm). The objective has a magnification of 20x, and its numerical aperture is 0.4. In combination with a $f = 250$ mm tubus lens, the dimensions of the field of view become 356×264 μm^2; large enough to contain up to 4000 particles. The microscope is used in the transmitted light bright-field mode, with the sample cell illuminated by a red light emitting diode ($\lambda \approx 650$ nm) from above (Fig. 3.8). The red light is collected with a lens and focused on the sample cell. It homogeneously illuminates an area whith a diameter of 6 mm, about 15 times larger than the region of interest. As seen in Fig. (3.8), using a reflecting mirror and a dichroic mirror only the image of the particles is projected onto the chip of the first charge-coupled device camera (CCD). The chip size is 8.8 mm x 6.6 mm including 752 x 582 pixels (Tokyo Electronic Industry). 99 % of the intensity of the laser beams with wavelengths $\lambda = 532$ nm, 488 nm, and 514 nm used to produce the substrate potential, the boundary box, and the pressing down tweezers are back-reflected by a dichroic filter infront of the microscope objective to avoid

any damage. The remaining intensity of the $\lambda = 532$ nm beams is used to image the substrate potential using a dichroic mirror deflecting the image to a second CCD camera. In front of the first camera, filters are placed to absorbe any remaining light intensities with wavelengths smaller then 600 nm and infront of second camera an interference filter allows only the imaging of intensities with wavelength 532 nm.

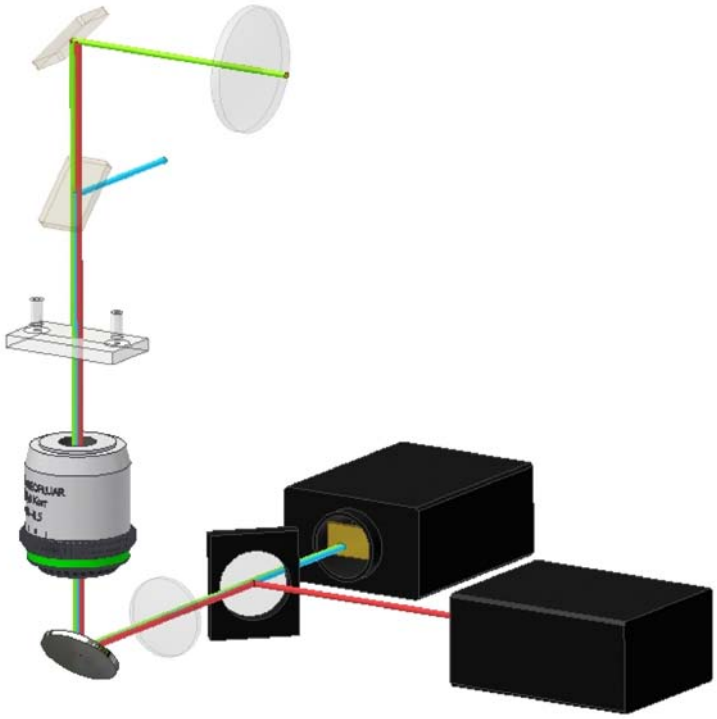

Figure 3.8: Scheme of the video microscopy setup. It includes two CCD cameras and several optical components, allowing the simultaneous detection of the particles and the substrate potential.

To observe the colloidal system and the substrate potential, the CCD cameras are connected to two monitors. In addition, the camera's signals are digitalized using a frame grabber and saved on a computer hard disk. These images are considered as raw data and to extract the coordinates of each particle a program called "IPS" developped by the company "Visiometrics" is used.

The software is based on an algorithm which analyses the brightness of each pixel in the image and relates it to the particle coordinates. For a typical snapshot, a pixel intensity histogram is calculated. These intensities are usually spread over a wide range (Fig. 3.9). The high values are associated to the bright white background and the low values are associated to the dark particles. With two markers an upper and lower thresholds are adjusted in order to set the pixel brightness belonging to

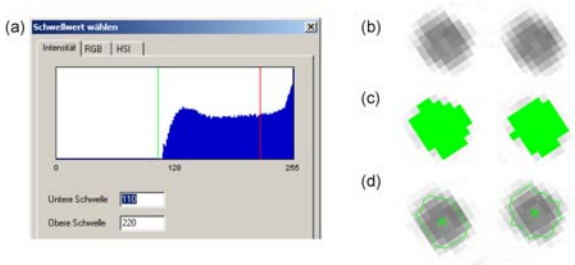

Figure 3.9: (a) Intensity histogram of a typical snapshot. With two markers (green and red lines) an upper and lower threshold are adjusted in order to set the pixel brightness belonging to a particle (object). (b) Picture of two particles in the raw image. (c) Identification of the particles as objects after setting the thresholds. (d) The center of mass of the object is then calculated and marked with a cross. This gives the coordinates of the object.

a particle. The center of mass of the object is then calculated and the particle is traced over all the snapshots.

The accuracy of the method depends on the magnification of the objects and the size of a pixel on the chip of the CCD camera. The more pixels the CCD chip has, the more pixels a single object obtains. The number of pixels per object is higher for increasing magnification. However, by increasing the magnification the size of the region where the system can be studied decreases. A compromise between a large viewing area and a good accuracy should be achieved. For the colloids used in the experiments about 9 pixels are detected for each particle. This leads to a resolution of about 150 nm.

3.4.1 Particle tracing and phase identification

The particle coordinates registered for a sequence of snapshots are used to evaluate the temporal evolution of the particles. In this thesis, we mainly used an algorithm developed by Neser and Bubeck (Visiometrics Trace) which allows tracing the particles and calculating different quantifiers. In Fig. (3.10), an illustrative example of the data evaluation is shown. The trajectory of every single particle can be constructed if the time interval between two recorded images is small (Fig. 3.10b). A careful analysis of the trajectories shows whether the system (particles) is drifting along any preferential direction or not. The density distribution of the particles $\rho(x, y)$ calculated for a measurement shows the spatial distribution of the particles (Fig. 3.10c). $\rho(x, y)$ is a matrix whose z-values are the probability to find a particle at the position (x,y). The matrix is averaged over all images. It is also possible to monitor the particle number density during a measurement, an important parameter that needs to be controlled while investigating phase transitions in such systems (Fig. 3.10d).

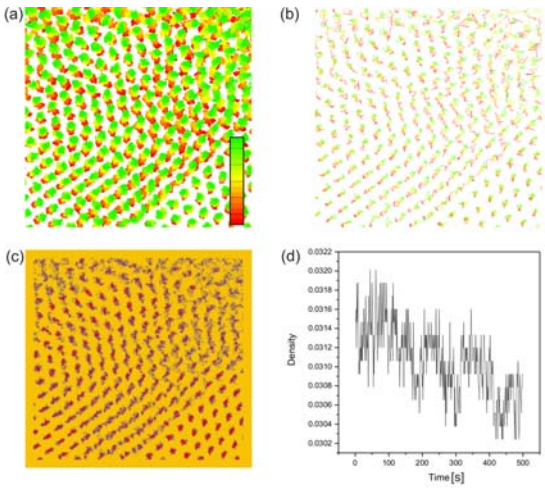

Figure 3.10: Illustrative example of temporal tracing of the particle coordinates. (a) Particle coordinates as registered over 500 seconds. The color coding, increasing from red to green, is associated to the time evolution. (b) Particle trajectories constructed using (a). (c) The density distribution of the particles over the whole period of the measurement. (d) Particle number-density plotted with respect to time.

Other physical quantities are used to identify the phase of a colloidal configuration. $S(q_x, q_y)$ calculates the two-dimensional structure factor of the particle coordinates. It is given by the following expression:

$$S(q_x, q_y) = \frac{1}{N} \sum_{j,k=1}^{N} \exp(iqr_{jk}) \tag{3.4}$$

with N the total number of particles. The pair correlation function $G(x, y)$ is an averaging over all particles and all images. It is related to the probability of finding the center of a particle at a given distance from the center of another particle. For short distances, this is connected to how the particles are packed together.

For identifying the bonds connecting two neighboring particles we use a method called Delaunay triangulation which constructs a network of non-overlapping triangles. The Delaunay triangulation of a point set is a collection of edges satisfying the "empty circle" property, i.e. for each edge one can find a circle containing the edge's endpoints but not containing any other points. We also use Voronoi diagrams which are the dual graphs of the Delaunay triangulation.

Since translational order parameters are not suitable for quasiperiodic structures, we use the bond orientational order parameter Ψ_m given by the following expression [92]:

$$\Psi_m = \left\langle \left| \frac{1}{N} \sum_{j=1}^{N} \frac{1}{n_j} \sum_{k=1}^{n_j} e^{im\Theta_{jk}} \right| \right\rangle \tag{3.5}$$

where the inner sum is over all n_j nearest neighbors of colloid j, N is the total number of particles, and θ_{jk} is the angle of the bond connecting colloids j and k given with respect to some arbitrary reference direction. In the next chapters, Ψ_m will be calculated for m = 6, 10, or 14, in order to characterize the different phases with nearest neighbor bonds that point, respectively, along 6, 10, or 14 equally distributed directions around the central particle. Ψ_m is a measure of the prevailing rotational symmetry.

3.4.2 Tiling algorithm

In the experiments described in the next chapters, particle positions are observed in real space with digital video microscopy. This allows the determination of their positions relative to the substrate potential with a high precision.

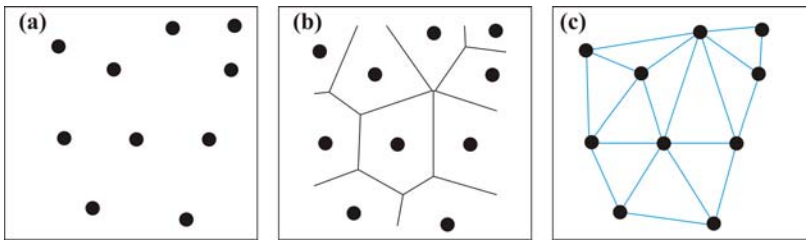

Figure 3.11: Illustrative example of the Voronoi tessellation and the Delaunay triangulation. (a) Coordinates of 10 random particles. (b) Voronoi tessellation dividing the plane into adjacent cells. (c) Connecting all the adjacent pairs of points leads to the Delaunay triangulation which consists of triangular tiles.

For the identification of the local particle configurations we have developed a tiling algorithm which can identify triangular, quadratic, pentagonal and higher order polygonal tiles. It is based on the Voronoi tessellation and the Delaunay triangulation which are widely used routines for the identification of the neighbors of a point in a point set (Fig. 3.11). The Voronoi tessellation in two-dimension is the division of a plane into cells. The cells contain the part of the plane which is closer to that point than any other. Thus every Voronoi cell contains precisely one point. The cells fit side by side without overlaps and without unfilled space. A boundary is shared by the adjacent cells thus one can define adjacent points by saying that points x and y are adjacent precisely if their Voronoi cells share a common edge. Connecting all the adjacent pairs of points one derives the dual or Delaunay triangulation. The vertices of one tile in a Delaunay triangulation are those points whose Voronoi tiles share a common vertex. This vertex is the center of the excircle of the Delaunay tile.

In the colloidal systems investigated in this thesis, the particles (even at high laser intensities) are not fixed at one point. Due to the thermal energy, they fluctuate around their equilibrium position. For the determination of the stable local configurations, i.e. stable tiles, we remove the bonds in the Delaunay triangulation which are not stable against these fluctuations. This is achieved by eliminating the short

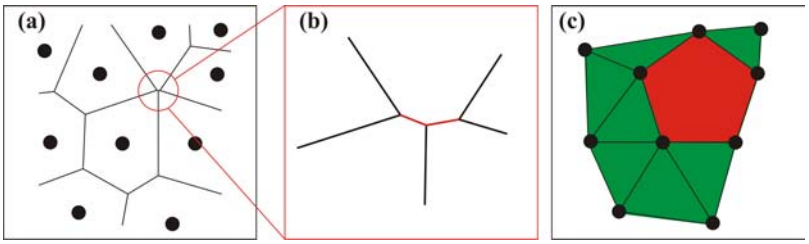

Figure 3.12: Principle of the tiling algorithm. (a) Voronoi tessellation of a set of points. (b) Detection of the short edges (in red) in the Voronoi tessellation. (c) Removing the short edges and consequently the corresponding bonds from the Delaunay triangulation leads to a tiling with pentagonal (red) and triangular (green) tiles.

edges from the Voronoi tessellation. Figure 3.12a shows the Voronoi tessellation of Fig. 3.11b, and Fig. 3.12b is a zoom on one of its vertices. It shows that the boundary of the Voronoi cells include short edges (highlighted in red). If these short edges are removed from the Voronoi tessellation and consequently the corresponding bonds in the Delaunay triangulation, a tiling consisting of different stable polygonal tiles is acquired. Accordingly, the local particle configurations are obtained independently from the thermal fluctuation effects. Fig. 3.12c is an example showing the Delaunay triangulation tiling after removing the bonds corresponding to the short edges in the Voronoi tessellation. This tiling shows the occurrence of a pentagonal (red) and several triangular tiles (green).

Within this tiling method, two tiles are considered distinct if their vertex number is different. Tiles of different size or orientation are not considered distinct. The cutoff value a_c, set for the Voronoi edge length, is a parameter that we have fixed for all measurement. a_c is set to be $0.39A$ in the following measurements (with A the mean particle distance). For a quantitative analysis, the density of the tiles with n vertices ρ_n^T is calculated.

It should be noted that this tiling algorithm cannot produce a quasiperiodic tiling with matching rules, such as the Penrose P3 tiling which is the appropriate tiling for the decagonal quasiperiodic interference patterns used in this thesis 1.2.3. This is due to the fact that tiles which are not convex, e.g. crown, are not detected with the routine. However, the Penrose P3 tiling includes pentagonal tiles oriented along two directions and such tiles can be identified with the algorithm described here. Accordingly, the occurrence of such tiles in the particle configuration is a strong indication of quasiperiodic ordering.

3.5 Quasiperiodic interference patterns

A multi-beam interferometer is used for the creation of spatially extended and highly stable substrate potentials (Fig. 3.13). By overlapping five or seven laser beams, interference patterns with decagonal or tetradecagonal symmetry are constructed.

Several parameters, such as the intensity, the polarization, the phase, and the angles of incidence have to be very precisely adjusted. In the following we describe the functionality of the interferometer and the control of the different parameters.

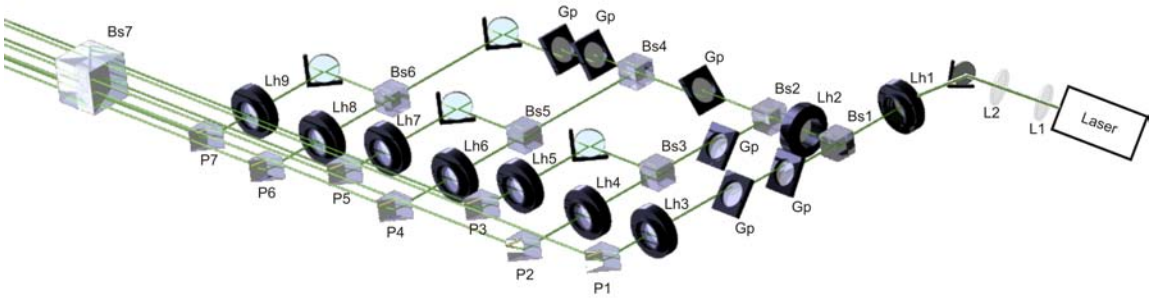

Figure 3.13: Scheme of the setup creating the optical substrate potentials. It basically consists of a modified Mach-Zehnder interferometer. The laser beams interfere inside the sample cell (not shown here), creating a well-defined quasiperiodic intensity distribution. The prisms P1 to P7 are mounted on translational stages for easy adjustment of the length scales of the interference pattern. Lh1-7 are lambda-half plates, Bs1-6 are polarizing and non-polarizing beam splitters, L1 and L2 are two achromatic lenses, and Gp refers to different glass plates.

A schematic representation of the setup is shown in Fig. (3.13). As a coherent light source we used a frequency-doubled and continuous-wavelength $Nd : YVO_4$ laser with a maximum power output of 18W (Verdi $\lambda = 532$ nm, Coherent, USA). According to the manufacturer, the beam divergence is less than $0,5$ mrad. First, the beam going out of the cavity (with a diameter of $\approx 2.25\,mm$) is broadened by a beam expander (BX). This Keplerian telescope consists of two convex lenses (L1 and L2) with focal lengths $f_1 = 80$ mm and $f_2 = 200$ mm. The lenses are set in a way to have in between a distance equal to $f_1 + f_2$, magnifying the beam diameter 2.5 times ($f_1/f_2 = 2.5$). At this position, a small deviation of the second lens from its optimal position, makes the beam slightly convergent. This leads to a variation of the size of the light pattern in the sample cell (Fig. 3.15). The large beam is divided by a set of polarizing and non-polarizing beam splitters (BS) in order to create up to seven coherent laser beams. To ensure that the scattering forces in the sample cell act on the particles only in the vertical direction, the intensities of all the beams are required to be equal. For that purpose, nine lambda-half plates are inserted in the path of the beams in combination with a polarizing beam splitter (BS7) placed at the output of the interferometer. This allows a precise tuning of each individual beam intensity using a power meter (fieldmaster, Coherent). The height of each beam, relative to the optical table, is adjusted by making them pass through several 1cm thick and tilted glass plates (GP). The tilt of the GP defines the height of the beams. The resulting beams are aligned parallel to each other using seven prisms (P1 to P7)

mounted on micrometer translational stages and Piezo nanopositioners (P-753 LISA, PhysikInstrumente). Using the nanopositioners the relative phases of the beams can also be controlled. The effect of the phase shifting on the interference patterns will be discussed later in detail. Accordingly, the lateral and vertical positions of the laser beams are easily adjustable and different geometrical configurations can be realized. For the decagonal patterns, the last two beams are blocked and the rest are set on the edges of a regular pentagon (Fig. 3.14). For the tetradecagonal patterns, a regular heptagon is used instead. With an achromatic lens (L3) the parallel beams are overlapped in the focus plane of the lens, thus creating the desired intensity pattern (Fig. 3.14). The position of the lens is chosen such that the focus (f_3) is inside the sample cell. All the incident angles of the laser beams have to be equal. This ensures that all the components of the wave vectors inside the sample plane are balanced. A non-vanishing net component of the wave vector in the sample plane leads to a lateral light pressure on the particles. This results in a drift motion of the particles along a preferential direction.

In contrast to periodic structures which are characterized by a single length scale, their quasiperiodic homologues have two or more. In this setup, these length scales depend only on the vertical angle of intersection of the laser beams. This angle can be varied by controlling their distance s towards the center of the lens (L3) and an appropriate choice of the focal length f_3. For different polarizations, different types of patterns are obtained [93, 94, 95]. Nevertheless, the global symmetry is not affected. In our experiments the polarizing beam splitter (BS7) ensures that the linear polarizations of the interfering beams have all the same direction.

In general, the interference of n beams in the sample plane form a periodic or a quasiperiodic pattern with a m-fold rotational symmetry. m is equal to n if the number of beams is even. If the number of beams is odd, m is then equal to $2n$. The intensity field is calculated by summing up the electric fields of all beams, and taking the square of the total electric field to get the intensity. The corresponding optical trapping potential is then given by the following expression:

$$V(r) = -\frac{V_0}{n^2} \sum_{j=0}^{n-1} \sum_{k=0}^{n-1} \cos\left[(G_k - G_j).r + \phi_k - \phi_j\right], \tag{3.6}$$

where V_0 is the potential depth of the unique perfect symmetry center, G the wave vectors projected onto the sample plane, r the position, and ϕ_i the phase of the i^{th} beam.

The opening angle θ between the laser beams and the orthogonal to the sample plane depends on s (Fig. 3.14), and on the focal length of the achromatic lens f_3.

$$\tan\frac{\theta}{2} = \frac{s}{2f_3}, \tag{3.7}$$

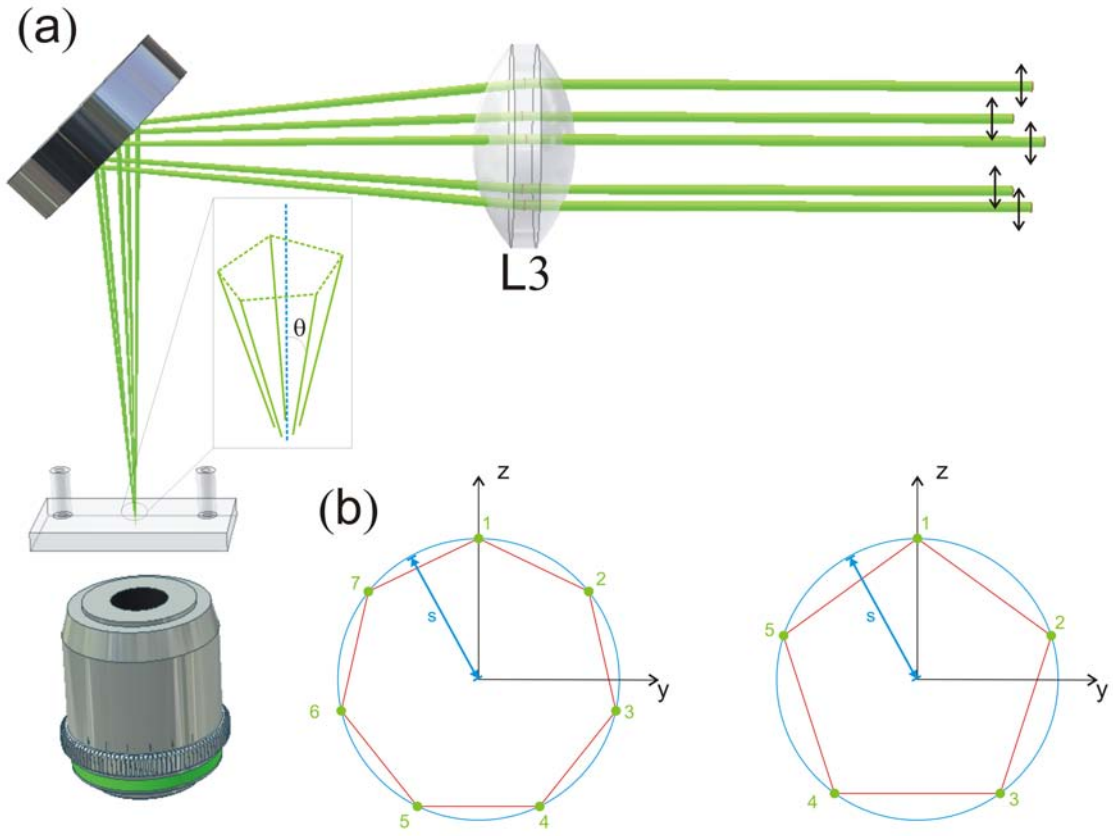

Figure 3.14: (a) Five linearly polarized parallel laser beams (polarization indicated by arrows), forming a regular pentagon, are focused with an achromatic lens (L3) into a thin sample cell. The opening angle θ between the laser beams and the orthogonal to the sample plane is chosen to be very small. (b) The ordering of the beams in the plane of the lens is shown for both decagonal and tetradecagonal patterns.

For the experiments performed θ is typically a few degrees, i.e. $\theta = 4°$ for $s = 11\,mm$ and $f_3 = 160mm$. The projected wave vector in the sample plane is given by:

$$G_j = \frac{2\pi s}{\lambda f_3} \tag{3.8}$$

$G_j = 8.12\ \mu\text{m}^{-1}$ for the above given parameters.

3.5.1 Extended patterns

If the laser beams are collimated in front of L3, the foci are located in the sample cell with typical diameter of approximately 5 µm. Therefore, no lateral extension of the light pattern can be created. To extend the light lattice, the distance between L1

and L2 (first BX) must be changed in order not to match the sum of the respective focal lengths (Fig. 3.15). By increasing the distance by Δl the collimated beams become slightly convergent after the beam expander, focused close to the last beam splitter, and slightly divergent in front of L3. The foci are not located anymore in the sample cell, instead they are shifted up. The size of the beams in the sample cell increases by increasing Δl. Accordingly, the area where the beams overlap and interfere becomes larger.

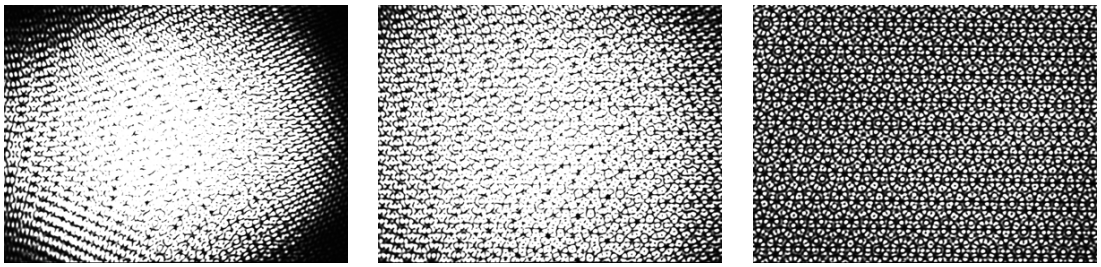

(a) (b) (c)

Figure 3.15: Intensity distribution of a tetradecagonal interference pattern depending on the distance between the two lenses of the beam expander. (a) L2 displaced by $\Delta l = 10$ mm from collimation, (b) $\Delta l = 15$ mm, and (c) $\Delta l = 41$ mm. The gaussian distribution seen in (a) and (b) vanishes by appropriate expansion on the pattern as seen in (c).

It should be noted that because the intensity of the laser beams has a gaussian distribution, the resulting potential landscape will always have a Gaussian profile, i.e. a decrease in the intensity distribution along the radial. This leads to non desired effects, such as a spatially dependent interaction strength between the colloidal particles and the substrate potential. In our experiments we have reached an almost constant intensity distribution over the whole field of view (the region where the measurements are performed) for $\Delta l_3 = 41$ mm. This expansion leads to a circular pattern with a diameter of about 1.5 mm, almost five times larger than the field of view. Even larger patterns can be created using this technique, but the intensity density and the potential strength decrease rapidly.

3.5.2 Decagonal and tetradecagonal potential substrates

The intensity patterns are regarded in our experiments as substrate potentials for the colloidal particles. Therefore, their properties must be characterized. The symmetry and the length scales are controlled by the construction of the interference pattern. Using digital video microscopy both parameters can be directly measured. Quasiperiodic interference patterns, in contrast to their periodic homologues, are not characterized by one potential depth. They consist of many potential wells with a specific potential depth distribution. These intensity patterns possess only one center of perfect rotational symmetry where all the phases ϕ_i of the beams are the same.

This center is also characterized by being the deepest potential well with a potential depth (V_0). However, other wells resemble to a large extend to the perfect symmetry center. They also enclose locally the global symmetry of the pattern and the corresponding potential depth is typically larger than $0.95V_0$. Therefore, the uniqueness of the perfect center will be in our experiments neglected.

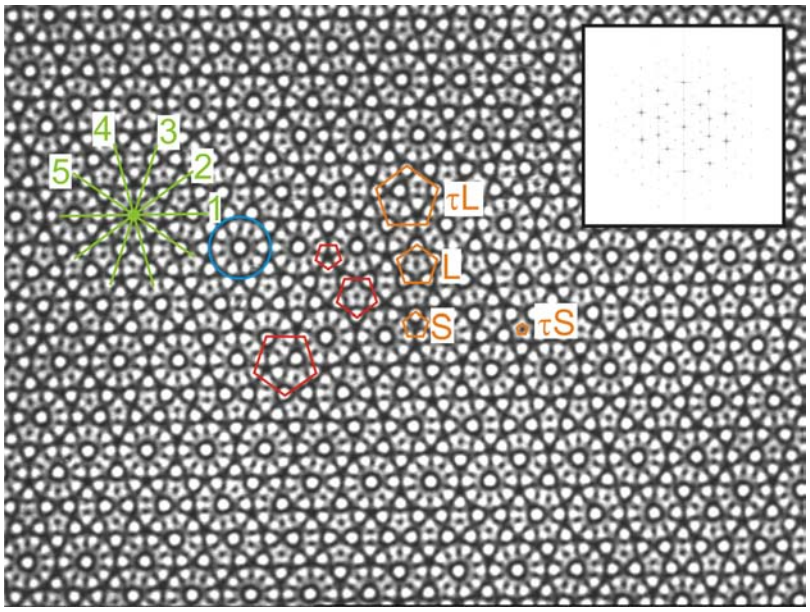

Figure 3.16: Snapshot of a quasiperiodic decagonal light substrate (356×264 μm^2) created by overlapping five laser beams. The pattern is characterized by five high symmetry axes (green lines). The potential wells (or intensity maxima) are arranged in pentagons of different size whose side lengths and heights are related by the golden ratio τ leading to two characteristic length scales (Large and Short) related by τ. Pentagons pointing up are colored in orange and those pointing down are colored in red. Another important feature is the occurrence of flowers (blue circle) having locally the global symmetry of the pattern (10-fold). The inset is a Fast Fourier Transform elucidating the decagonal (10-fold) symmetry.

Figure (3.16) shows the light intensity distribution in the sample plane which displays maxima arranged in pentagons of different size whose side lengths and heights are related by the golden ratio. Accordingly, the pattern has two intrinsic length scales a large one L and a short one S with a ratio equal to τ. The pattern is characterized by five high symmetry axes (green). Another important topological feature is the occurrence of flowers (blue circle) having locally the global 10-fold symmetry of the patterns. A Fast Fourier Transform of the figure leads to a lattice in the reciprocal space with decagonal symmetry (10-fold). For this decagonal pattern, one can always find translations which leave the potential almost (!) unchanged although strictly speaking the pattern has no translation symmetry (Fig. 3.17). This is a property of certain quasiperiodic structures, and it is called "local isomorphism" or

sometimes "indistinguishability". The reason for this is that the interference pattern contains substructures that repeat often and two parts of the pattern may contain the same statistical distribution of these substructures. Another remarkable structural property, is the self-similarity of the pattern. If the pattern is locally inflated or deflated by the golden ratio the original local structure is recovered. Similar inflation rules are known for octagonal and dodecagonal quasilattices [96].

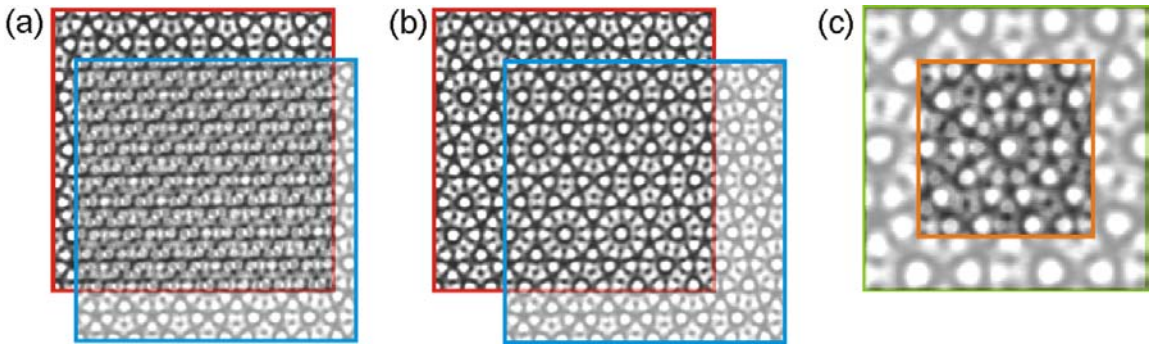

Figure 3.17: Local isomorphism and self-similarity of a decagonal substrate potential. (a) Mismatch between two identical cuts of the pattern for a random translation. The pattern with the blue contour is set to be transparent and translated by some amount relative to the pattern with the red contour. (b) The pattern is translated until regions of high intensity coincide. (c) Illustration of the self similarity of the pattern. The same cut of the pattern is up scaled by the golden ratio and placed on top of the original one. The matching regions are identified by the bright white color.

Figure (3.18) shows the light intensity distribution in the sample plane for 7-beam patterns. The maxima are arranged in heptagons of different size whose side lengths and heights are related by two irrational numbers ($\cos(\frac{\pi}{14})$ and $\cos(\frac{3\pi}{14})$) leading to three length scales. This pattern is characterized by seven high symmetry axes (green lines). The flowers here (blue circle) enclose the 14-fold symmetry. A Fast Fourier Transform of the figure leads to a lattice in the reciprocal space with tetradecagonal symmetry.

3.5.3 Potential depth distribution

As previously mentioned, the patterns consist of minima with different potential depth. Schmiedeberg and Stark calculated the probability to find a well of a certain depth for both decagonal and tetradecagonal patterns [97]. The probability density $\rho(V_m/V_0)$ for a minimum to have a potential value V_m is plotted in Fig. (3.19a-b). Both distributions are continuous, nevertheless for the decagonal pattern, minima with depths below $V_m/V_0 < 0.25$ do not exist. This indicates that the potential has no shallow minima and it mainly consists of deep wells since the distribution converges to a finite probability for $V_m = V_0$. In contrast, the tetradecagonal pattern

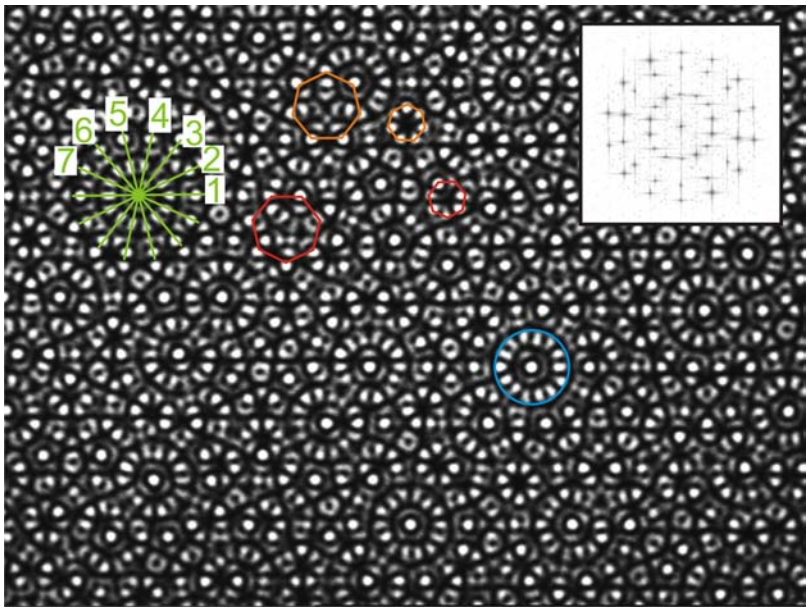

Figure 3.18: Snapshot of a quasiperiodic tetradecagonal potential substrate (356×264 μm^2) created by overlapping seven laser beams. The pattern is characterized by seven high symmetry axes (green). The potential wells (or intensity maxima) are arranged in heptagons of different size whose side lengths and heights are related by two irrational number leading to three length scales. Heptagons pointing up are colored in orange and those pointing down are colored in red. Another important feature is the occurrence of flowers (blue) having locally the global symmetry of the patterns (14-fold). The inset is a Fast Fourier Transform elucidating the tetradecagonal (14-fold) symmetry.

includes minima with $V_m/V_0 < 0.25$ and the distribution practically goes to zero for $V_m = V_0$.

In Fig. (3.19c-d) calculated patterns are plotted with decagonal and tetradecagonal symmetries, respectively. In order to illustrate the ordering of the deep potential minima, the plots are color coded in accordance with the depth. For $V_m > 0.75V_0$, the minima are colored in blue and they mainly correspond to the center of the high symmetry stars.

In the experiment, the potential strength and the intensity of the laser beams (P) are linearly related. The relationship between V_0 and P can be measured using an interference pattern of three laser beams as potential substrate. In this case, the periodic pattern is characterized by one potential depth V_0. Since the probability distribution of the particles inside an external potential is governed by the Boltzmann distribution, the strength of the external laser potential is determined by measuring the averaged density distribution of a dilute suspension of particles (Fig. 3.20). Using this calibration of the laser intensity, V_0 can be extrapolated for the decagonal and tetradecagonal patterns.

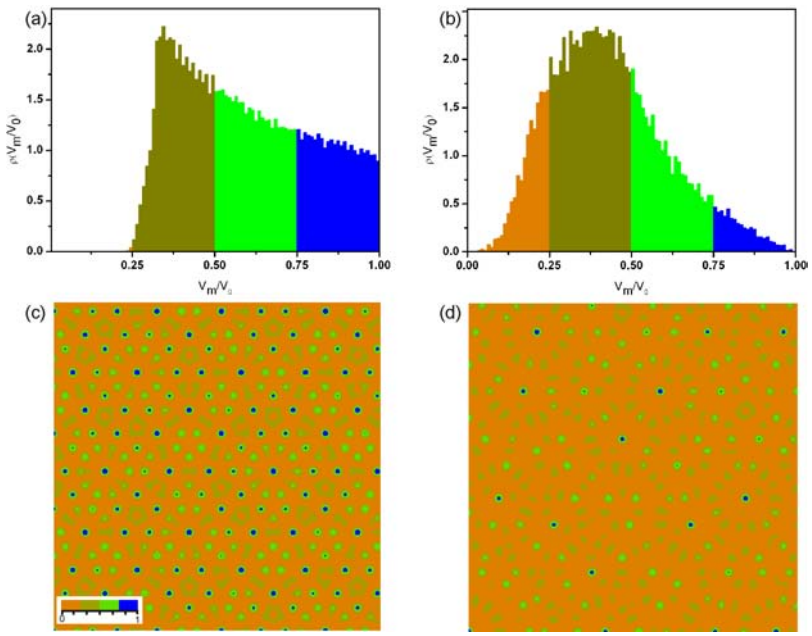

Figure 3.19: Distribution of the probability density $\rho(V_m/V_0)$ for a minimum to have a potential depth V_m in a decagonal (a) and tetradecagonal potential (b) [92]. V_0 is the deepest minima. (c-d) Numerically calculated patterns with false color coding corresponding to the distribution in (a) and (b).

3.5.4 Static strain fields

As shown in chapter one, quasicrystalline structures have physical characteristics that cannot exist in periodic structures. For example, in a periodic crystal, translations that vary slowly as a function of position define a phonon-strain field which slightly increases the free energy of the system. The strain field is described in terms of phonon collective excitations [13]. In contrast, in quasiperiodic crystals, one obtains phason-strain fields, described in terms of phason low-energy collective excitations [13].

Such static strain fields also exist in quasiperiodic interference patterns. When the relative phase of a lattice-forming laser beam varies with a constant gradient (position dependent change), a phason-strain field is created. As a result, characteristic lines of low intensity (infinitely extended in a perfect pattern) acquire a finite length (see blue lines in Fig. 3.21a,d). Experimentally, this occurs when the tilt angle of a laser beam is altered compared to the tilt angle of the other beams. This means that laser beams not perfectly adjusted relative to the vertical, lead to a substrate potential with phasonic jaggs which density is usually orientation dependent. In our experiments, we identify and control the phason-strain along each direction by means of Fourier filtering [13]. In fact, one of the signatures of a phason-strain field is the appearance of anisotropic shifts in the positions of Bragg peaks in the diffraction pattern. A back-Fourier transform of the shifted peaks leads to a real space image

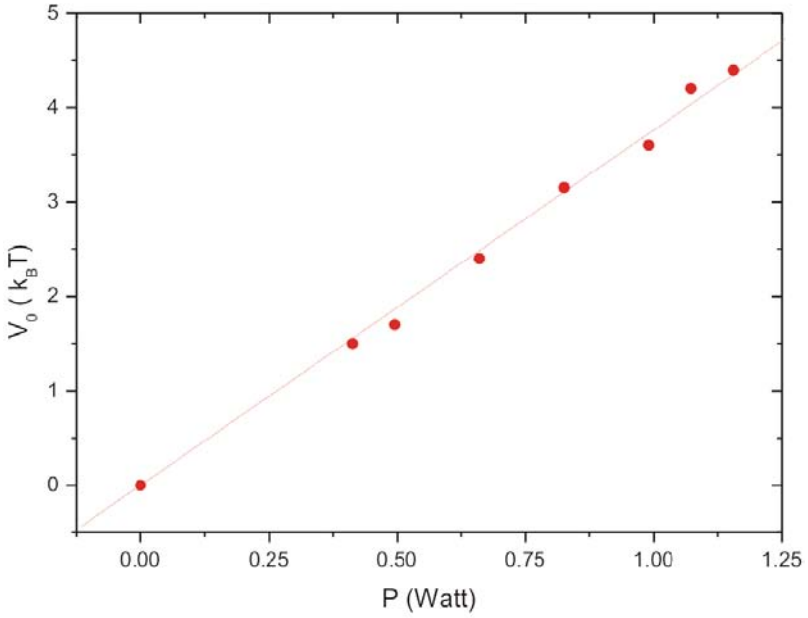

Figure 3.20: Potential strengths V_0 (dots) for different laser power P measured for a dilute system of particles interacting with a triangular lattice. The straight line is a linear regression for the data points.

with jaggs. These jaggs are the "finger print" of the existence of the phason-strain fields.

Figure (3.21) illustrates the procedure in numerically calculated interference patterns. A perfect decagonal pattern contains characteristic low intensity lines (blue lines), infinitely extended and oriented along five different directions (Fig. 3.21a). Its Fourier transform results in a pattern with characteristic Bragg peaks (Fig. 3.21b). When two pairs of Bragg peaks at τ related wavevectors are filtered out (green circles), the back-transform (as seen in Fig. 3.21c) results in an intensity distribution image formed out of stripes which distance follow the Fibonacci sequence. When the same procedure is applied to an interference pattern including phason-strain, induced by changing the tilt angle of one of the laser beams, the back transformed image shows jaggs in the pattern of stripes indicating the existence of local rearrangements with respect to the perfect pattern. The phason-strain is already seen in Fig. 3.21e by the existence of Bragg peaks shifted with respect to the radial (red dashed line).

3.5.5 Substrate potential reconstruction

One of the major advantages of this system, compared to atomic systems, is the particle tracing in real space which allows to determine their positions. More important is the determination of the particle positions relative to the interference pattern. That is why we included in the setup two CCD cameras to monitor simultaneously

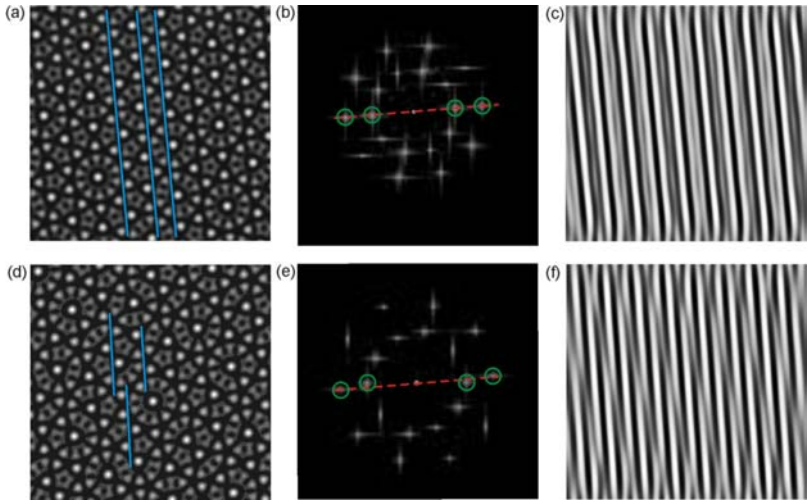

Figure 3.21: Numerically constructed interference patterns, with and without a static linear phason-strain field. (a) A perfect decagonal pattern. (b) Fourier transform of the real-space image. The white spots are the Bragg peaks of the quasicrystal and the green circles highlight the spots used for the back transformation in (c). (c) Real space image obtained by filtering only the four spots within the green circles shown in (b). (d-f) The same as (a-c) after adding a static linear phason-strain field. This is achieved by slightly changing the angle of incidence of one of the lattice-forming laser beams. The phason-strain is visible as "jaggs" in (f).

the particles and the substrate potential. Since the colloidal particles are in the same optical plane as the interference pattern, the image of the pattern also contains the green light scattered on the particles (Fig. 3.22a).

The contribution of these colloidal particles to the image could be considered as noise. A particularly useful method for isolating noise in an image is the Fourier filtering. This method belongs to a class of digital image processing algorithms utilized to transform an image into the frequency domain. After an image is transformed and described as a series of spatial frequencies, a variety of filtering algorithms can be applied, followed by a back-transformation of the filtered image to the spatial domain. This method is useful for performing a variety of filtering operations that are otherwise very difficult to perform with a spatial convolution.

There are three basic steps to frequency domain filtering. First, the image must be transformed from the spatial domain into the frequency domain using a Fast Fourier transform. Second, the resulting complex image must be multiplied by a filter. Third, the filtered image must be transformed back to the spatial domain. We have implemented these steps in an IDL (programming language) program using a Fast Fourier transform function FFT.

The low frequency terms usually represent the general shape of the image and the high frequency terms are needed to sharpen the edges and provide the details. Instead

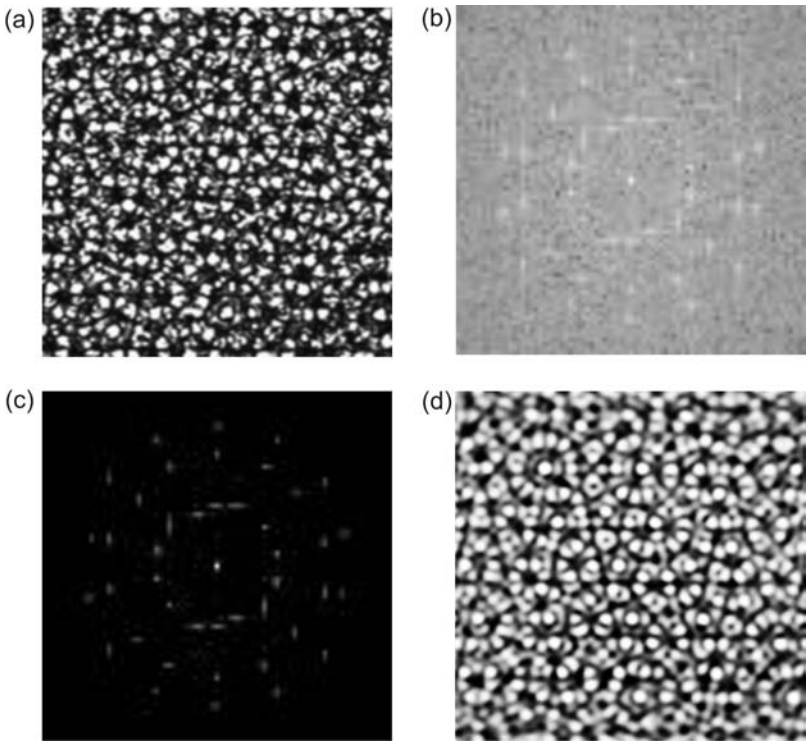

Figure 3.22: Image processing with Fourier filtering. (a) Snapshot of the substrate potential in the presence of a dense layer of colloidal particles. (b) Fast Fourier transform of the image in (a) showing the 14-fold symmetry and a noisy background . (c) The transform in (b) after filtering of the background (details in the text). (d) Back-Fourier transform showing an image which is almost identical to an image of the laser intensity distribution taken in the abscence of the particles.

of just analyzing the frequency domain image, we calculate its power spectrum. The power spectrum is a plot of the magnitude of the various components of the frequency domain image. Different frequencies are represented at different distances from the center of the image. The power spectrum shows how much of a frequency is present in the image. It is particularly useful for isolating the quasiperiodic structure or the noise in the image.

As a next step we apply a filter to the frequency domain image. A variety of adjustable filter masks, such as high-pass, low-pass, or free-hand filter, can be superimposed on the power spectrum image in order to filter desired frequencies. For removing the noise we set a lower threshold value for the magnitudes in the power spectrum. A reconstructed image displaying only the interference pattern is obtained through a back-Fourier transformation of the filtered Fourier transform image. Figure (3.22d) shows the dramatical improvement of the quality of the image.

3.6 Light induced quasiperiodic ordering

In the following, we show how the combination of all the above discussed experimental tools leads to the formation of a two-dimensional colloidal quasicrystal. The latter is illustrated by investigating the phase behavior of a fluid system with a mean particle distance $A = 5.7$ μm in the presence of a decagonal substrate potential characterized by two length scales $S \approx 5.4$ μm (short) and $L \approx 8.8$ μm (long).

3.6.1 Experimental procedures

In these experiments, we use an aqueous suspensions of highly charged sulphate-terminated polystyrene particles with a radius of $R = 1.45$μm from Interfacial Dynamics Corporation with an average polydispersity below 4 %, a solid content of 8.1 %, and a surface charge density of 9.8 μC/cm^2. Their refractive index is $n_{PS} = 1.59$.

The beginning of the measurement consists in the preparation of the colloidal suspension. First, 30 to 50 μl are taken from the main suspension. In order to reduce the amount of dissolved ions from this suspension, we mix it with about 200 μl of highly deionized water. The deionization of the water is performed as described in section 3.1. The mixture is later centrifuged, which forces the colloidal particles to sediment at the bottom of the sample container. The excess of water, which contains the largest amount of counterions, is then removed. Since this process strongly increases the interaction strength, it is repeated up to three times. Finally, the sealed vial containing the suspension is inserted in an ultrasonic bath for 10 to 15 minutes in order to separate any coagulated particles.

The highly deionized suspension is injected using a micro-pipette into the water reservoir of the deionizing circuit described in Fig. 3.3. With a very slow pumping rate, the suspension is homogeneously pumped into the sample cell which is then sealed with clamps. In this way, the suspension in the sample cell is isolated from the rest of the circuit and ions are prevented from diffusion into the cell.

Due to the gravitational force the colloidal particles sediment and form a monolayer on the lower surface of the sample cell. Before applying the quasiperiodic potential, the density of the particles in the field of view is adjusted using thermophoretic and optical forces (see section 3.2). The vertical fluctuations of the particles are suppressed by applying the pressing down laser beam (section 3.3). The particle density is kept constant using the optical fence (Fig. 3.6).

The linearly polarized laser beams creating the interference pattern are then coupled to the sample cell. Due to optical gradient forces, this interference pattern acts as an external potential on the particles with the potential amplitude scaling linearly with the laser power.

3.6.2 Strong decagonal light fields as substrate potentials

When a colloidal monolayer is exposed to a patterned light field, considerable changes in its structure are observed. Figure (3.23) shows how the particle density distribution $\rho(x, y)$ and the two-dimensional pair correlation function $G(x, y)$ of a colloidal monolayer change upon increasing the substrate strength of the decagonal substrate. $G(x, y)$ gives the relative probability of a particle to have a neighbor at a distance r(x,y). In absence of a substrate potential ($I_0 = 0$) the system adapts the structure of an isotropic fluid phase (data not shown). A very weak substrate potential of $I_0 = 0.63\ \mu\mathrm{W}\mu\mathrm{m}^{-2}$ is not capable to make any considerable changes in the isotropic structure of the fluid (Fig. 3.23a-b). This is confirmed by both $\rho(x, y)$ and $G(x, y)$. The latter shows that the correlation in the positional order of the particles is only short ranged and decays fast at large distances. For $I_0 > 2.54\ \mu\mathrm{W}\mu\mathrm{m}^{-2}$, the isotropy is broken. Already at such low substrate strength, $\rho(x, y)$ shows a density modulation, i.e. specific positions of the substrate potential are sampled often (red color). Obviously, the deep substrate potentials are already exerting a relatively strong attractive force on the neighboring particles. This can also be seen in the corresponding correlation function in Fig. 3.23d. Locally an almost isotropic positional correlation can be observed while at larger distances a long range order is present.

By increasing the potential to $I_0 = 3.82\ \mu\mathrm{W}\mu\mathrm{m}^{-2}$, the formation of pentagonal motives in $\rho(x, y)$ is observed. Since these motives are characteristic to the underlying substrate potential, their formation indicates that the potential strength is strong enough to attract the particles at potential wells which are less deep. This is also seen in $G(x, y)$ which shows a stronger positional correlation. Only at $I_0 = 5.73\ \mu\mathrm{W}\mu\mathrm{m}^{-2}$, most of the particles are trapped on lattice sites and laterally fluctuate only around the equilibrium position. A high number of pentagonal motives is observed in the density distribution and the positional correlation function shows a short and long range decagonal order.

Similar to any phase transition, this light induced quasicrystal occurs if the quasicrystalline ordering of the particles minimizes the free energy of the system. This indeed corresponds to the situation here, since the interaction energy among the particles is weak, and the potential energy of the substrate potential dominates.

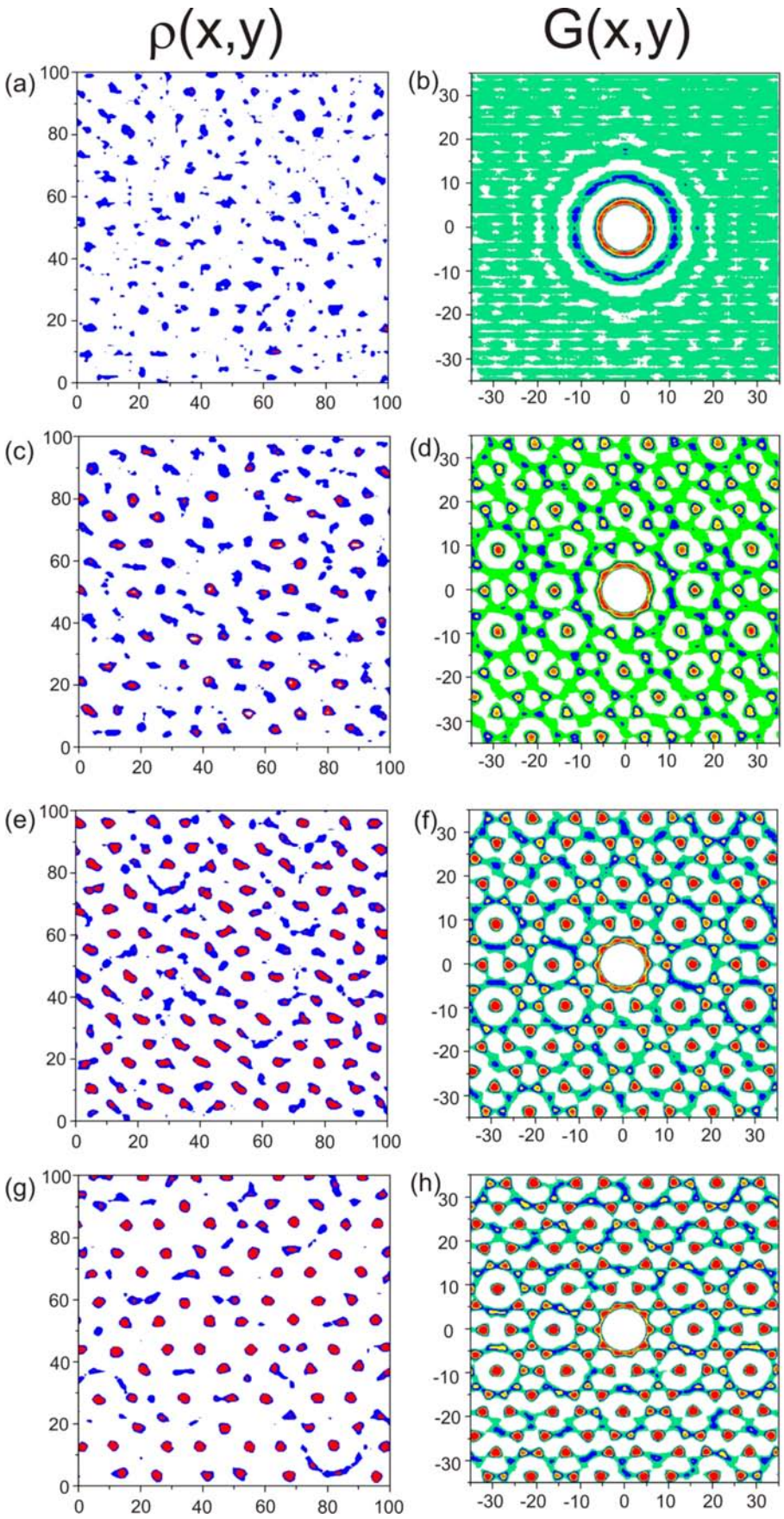

Figure 3.23: Contour plots of the density distribution $\rho(x, y)$ (left) and the pair correlation function $G(x, y)$ (right) for four different laser potential strengths. (a, b) $I_0 = 0.63\ \mu\mathrm{W}\mu\mathrm{m}^{-2}$, (c, d) $I_0 = 2.54\ \mu\mathrm{W}\mu\mathrm{m}^{-2}$, (e, f) $I_0 = 3.82\ \mu\mathrm{W}\mu\mathrm{m}^{-2}$ and (g, h) $I_0 = 5.73\ \mu\mathrm{W}\mu\mathrm{m}^{-2}$. The length scales are in μm.

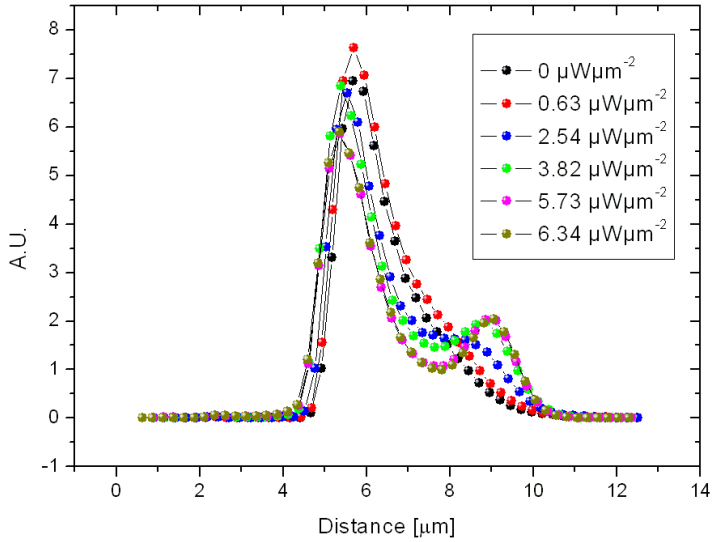

Figure 3.24: Bond-length histogram calculated for the particle configurations at different potential strength.

The change in the particle configuration and the assignment of the different phases is also evident by looking at the bond-length histogram. First, a Delaunay triangulation is performed to identify the next neighbor bonds and a histogram of the bond length is constructed. As seen in Fig. 3.24, the distribution sensitively depends on the different phases. At low laser intensities, a broad monomodal distribution with peak located at mean particle distance $A = 5.7$ μm is observed, indicating an isotropic fluid phase. By increasing the laser intensity, the peak gradually shifts to lower distances and simultaneously another peak starts to form at larger distances. For $I_0 = 3.82$ μWμm^{-2} the distribution becomes bimodal with the ratio of the two peak positions close to τ. The peaks positions are in fact located at $S = 5.4$ μm and $L = 8.8$ μm which ratio is close to τ indicating the occurrence of the quasiperiodic phase.

More evidence for the assignment of the different phases mentioned above is derived from the two-dimensional structure factor $S(q_x, q_y)$ (Fig. 3.25). As expected, $S(q_x, q_y)$ calculated for the fluid phase shows no occurrence of Bragg peaks and only diffuse background is present (Fig. 3.25a). At low potential strengths the external laser potential leads to a spontaneous symmetry breaking. This symmetry breaking destroys the isotropy of the fluid phase and leads to a density modulation which is rather quasiperiodic. For a numerically calculated pattern, 20 Bragg peaks are expected. Here, $S(q_x, q_y)$ displays a number of Bragg peaks which is still less than 20 (Fig. 3.25b). This indicates that the system is still not deep in the quasiperiodic phase. $S(q_x, q_y)$ calculated for the laser intensity $I_0 = 5.73$ μWμm^{-2} is the closest to the diffraction pattern of quasiperiodic patterns (Fig. 3.25c). The structure factor

of this quasicrystalline decagonal phase displays a dense set of delta-function Bragg peaks with higher harmonics and its symmetry is 10-fold.

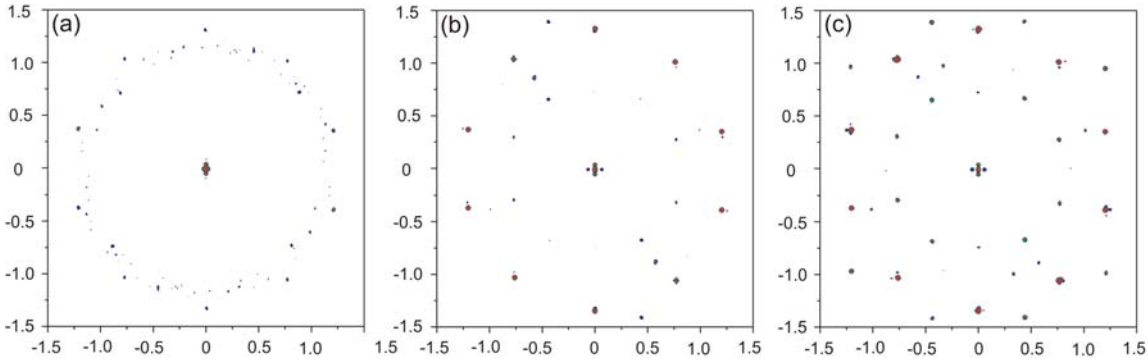

Figure 3.25: Two-dimensional structure factor $S(q_x, q_y)$ of the experimental data presented in 3.23(a,c,g). The axis are in units of $q = 2\pi/r$ where r represents the distance. (a) For the fluid at $I_0 = 0.63\ \mu\mathrm{W}\mu\mathrm{m}^{-2}$, (b) the intermediate phase at $I_0 = 2.54\ \mu\mathrm{W}\mu\mathrm{m}^{-2}$ and (c) the quasiperiodic phase at $I_0 = 5.73\ \mu\mathrm{W}\mu\mathrm{m}^{-2}$.

3.6.3 Strong tetradecagonal light fields as substrate potentials

Also when a colloidal monolayer is exposed to a tetradecagonal light field, considerable changes in the structure are observed. In this experiment, polystyrene colloidal particles with radius $R = 1.45\ \mu\mathrm{m}$ are used. The system is prepared so that, the density is $\phi = 0.020\ \mu\mathrm{m}^{-2}$ and $A = 5.98\ \mu\mathrm{m}$. The sample is later exposed to a 14-fold interference pattern and the laser intensity I_0 is stepwise increased .

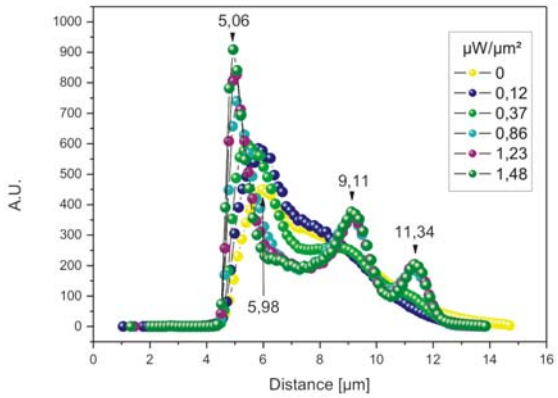

Figure 3.26: Bond-length histogram calculated for particles interacting with a tetradecagonal substrate potential at different laser power.

The change in the particle configuration upon increasing the laser power I_0 can be clearly seen in the change of the bond length histogram shown in Fig.3.26. At

$I_0 = 0$ μWμm^{-2}, a monomodal distribution with a peak located at the mean particle distance $A = 5.98$ μm is obtained, indicating an isotropic fluid phase. The fluid structure is confirmed by the calculated structure factor in Fig.3.27a. By increasing the laser intensity, the peak shifts to lower distances and simultaneously another two peaks start to form at larger distances. For $I_0 = 1.48$ μWμm^{-2} the distribution clearly becomes three-modal. The position of the peaks coincides well with the length scales of the underlying pattern. The colloid-substrate interaction is strong enough to overcome the colloid-colloid repulsion resulting in a change in the structure of the system.

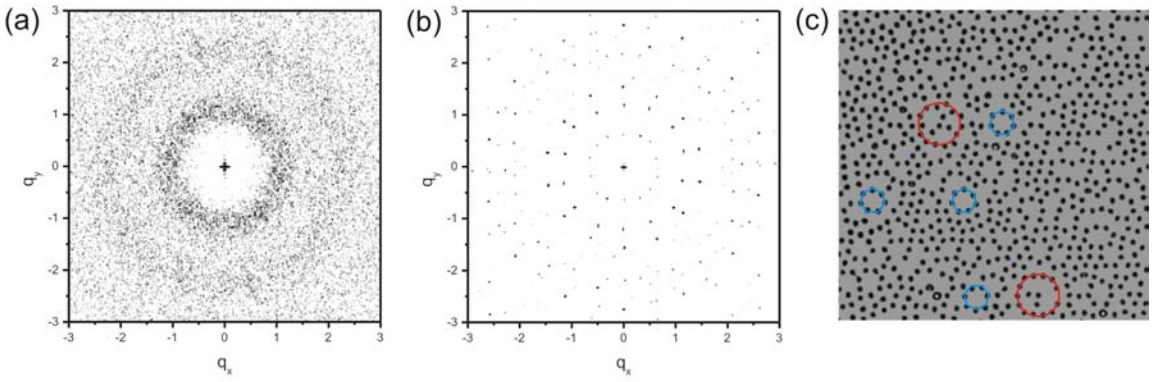

Figure 3.27: (a,b) Two-dimensional structure factor $S(q_x, q_y)$ calculated for $I_0 = 0$ μWμm^{-2} (a) and $I_0 = 1.23$ μWμm^{-2} (b). (c) Snapshot of polystyrene colloids at $I_0 = 1.23$ μWμm^{-2}. Typical motifs of the light pattern, i.e. flower (in red) and heptagon (in blue), are adapted by particles.

In Fig.3.27c a snapshot revealing the spatial distribution of the colloids is showed. A comparison with the intensity distribution of substrate potential (Fig.3.18) shows that the particles already at $I_0 = 1.23$ μWμm^{-2} have adapted some of the typical characteristics of the light field. Exemplary, a flower (red) and a heptagon (blue) are highlighted. The structure factor calculated for this snapshot is shown in Fig.3.27b. It has the expected 14-fold symmetry.

CHAPTER 4

STRUCTURAL PHASE TRANSITION OF DENSE MONOLAYERS ON DECAGONAL SUBSTRATE POTENTIALS

Measurements of the complex phase behavior of dense colloidal monolayers interacting with a quasicrystalline decagonal substrate created by interfering five laser beams are presented. Different starting configurations, such as dense fluid and triangular crystals with different densities, are prepared. At low intensities and high particle densities, the electrostatic colloidal repulsion dominates over the colloid-substrate interaction and the crystalline structure remains mainly intact. As expected, at very high intensities the colloid-substrate interaction dominates and a quasiperiodic ordering is observed. Interestingly, at intermediate intensities we observe the alignment of crystalline domains along the 5 directions of the quasicrystalline substrate. This is in agreement with observations of Xenon atoms adsorbed on the ten-fold decagonal Al-Ni-Co surface [98] and numerical simulations of weakly adsorbed atomic systems [32]. Intermediate phases are observed for colloid-substrate interactions strong enough to produce defects in the crystal. These defects adapt the form of rows of quadratic tiles.

Surprisingly, for specific particle densities (at which the colloid-substrate interaction is minimized) we identify a novel pseudomorphic ordering. This intermediate phase which exhibits likewise crystalline and quasicrystalline structural properties can be described by an Archimedean-like tiling [99, 100, 101] consisting of alternating rows of quadratic and triangular tiles. The calculated diffraction pattern of this phase is in agreement with recent observations of copper adsorbed on icosahedral $Al_{70}Pd_{21}Mn_9$ surfaces [102]. In addition to establishing a link between Archimedean tilings and quasicrystals our experiments allow to investigate in real space how single-element monolayers can form locally commensurate structures on quasicrystalline surfaces.

4.1 Motivation and introduction

As stated in the first chapter, deposition of thin films onto quasiperiodic substrates can lead to novel structures which may exhibit unusual properties. This approach might allow fabrication of materials with novel properties. Apart from understanding how quasicrystalline properties can be transferred to such adlayers, a pseudomorphic growth can help to understand the origin of many of the quasicrystals properties. In fact, because quasicrystallinity does not occur in single element systems but only in binary [28, 49] or even more complex ternary metal compounds [29], their surfaces exhibit a high degree of structural and chemical complexity. The disentanglement of the structural and chemical aspects can be achieved by growing single-element monolayers [30, 31]. The heteroepitactic growth experiments on decagonal and icosahedral surfaces shown in 1.3.2 indeed demonstrate the formation of Bi, Sb and Pb monolayers with a high degree of quasicrystalline order as determined by low-energy electron diffraction and elastic helium atom scattering experiments [40, 18, 38]. Compared to reciprocal space studies, only recently atomically resolved scanning tunneling microscopy investigations of the adsorbate morphology became possible [41, 39]. Even then, however, it is difficult to relate the structure of the adsorbate with that of the underlying substrate.

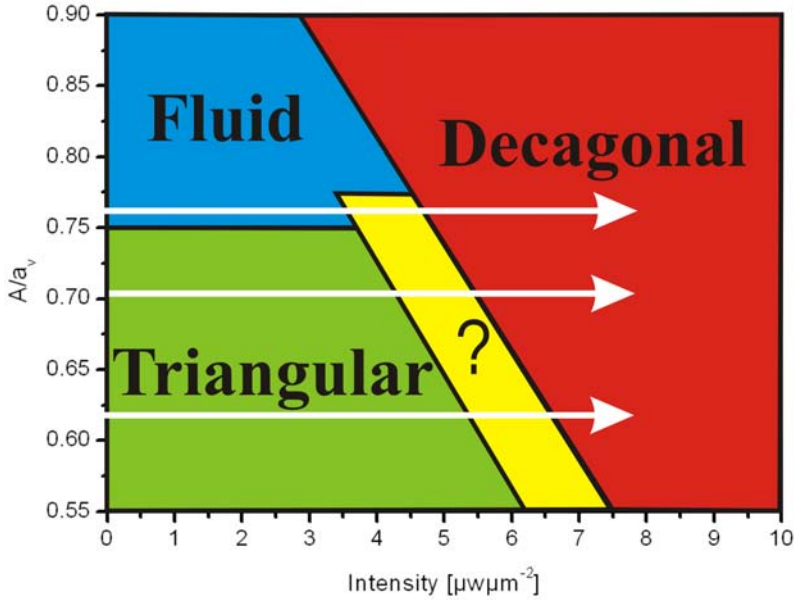

Figure 4.1: Expected phase diagram for dense colloidal systems interacting with a decagonal substrate potential for increasing laser intensity I_0. The system is charaterized by the density A/a_v, where A is the mean particle distance at $I_0 = 0$ and a_v the potential characteristic length scale. The white arrows indicate three regions of interest at which the measurements are performed.

In this respect, the study of the phase behavior of two-dimensional colloidal systems interacting with quasiperiodic potential substrates can bring new knowledge.

Instead of using topologically patterned substrates [103], we insert the colloidal particles into a sample cell with a flat glass surface (as described in the previous chapter) and create an external quasiperiodic laser field, which acts via light forces as an external potential. In this way, the colloidal structures can be classified at different regions in the phase diagram. In Fig. 4.1, an illustrative phase diagram is plotted. In the absence of the laser field ($I_0 = 0$), different starting phases can be prepared. For increasing particle densities (A/a_v), transition from a fluid phase (in blue), characterized by the short range order, to a triangular phase (in green) with long range order is expected. Independent from the density, at very high laser intensities the colloid-substrate interaction dominates and a quasiperiodic phase (in red) is expected. Our experiments help to understand the phase behavior especially at intermediate regions (in yellow) where both the electrostatic colloidal repulsion and colloid-substrate interaction play an important role. The white arrows indicate three possible paths at which the measurements are performed and which will be discussed in the following.

4.2 Transition from a dense-fluid phase to a decagonal phase

In this experiment colloids with radius $R = 1.45\mu$m and density $\phi = 0.0273\ \mu\text{m}^{-2}$ are used. This density was chosen to be slightly below the density required for spontaneous crystallization. In the absence of the quasiperiodic light potential, the particles form a dense fluid with mean particle distance given by:

$$A = \sqrt{\frac{2}{\phi\sqrt{3}}} \tag{4.1}$$

thus $A = 6.51\ \mu$m. The sample is later exposed to an interference pattern with characteristic length scale $a_v = 8.53\ \mu$m. The ratio of the particle mean distance A to the substrate length scale a_v, here $A/a_v = 0.763$, will be used to compare the densities of the different measurements. The laser intensity I_0 is increased at a rate much smaller than the typical relaxation time of the colloidal system which allows to establish equilibrium conditions.

Figs. 4.2 and 4.3 show the ordering of the tiles in real space and how the tilings and the corresponding $S(q_x, q_y)$ of the colloidal monolayer change when the substrate strength of the decagonal substrate is increased. In absence of a substrate potential, Fig. 4.2a, the tiling consists of triangular (green), quadratic (blue) and pentagonal (red) tiles. Because the system is close to crystallization, small regions or domains with different orientations and containing only triangular tiles can be observed. These domains are separated by defects making the local particle configuration quadratic or pentagonal. The structure of this phase is confirmed by the diffraction pattern in Fig. 4.2b, which mainly consists of isotropic rings. In the presence of a quasicrystalline light field, the particles also interact with the corresponding surface potential. The

formation of pentagonal tiles, having the same orientations as those occurring in the substrate potential, is expected. This is obviously not the case at $I_0 = 0.35\ \mu\mathrm{W}\mu\mathrm{m}^{-2}$. As seen in the tiling of Fig. 4.2c, the orientations of the pentagonal tiles are still random. This is also confirmed by the corresponding $S(q_x, q_y)$ in Fig. 4.2d which shows isotropic rings.

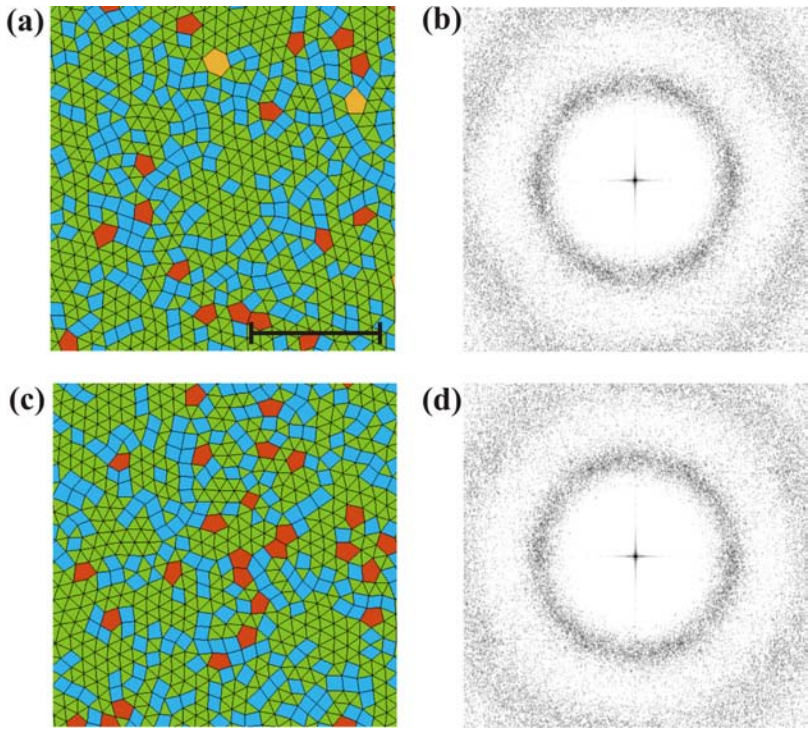

Figure 4.2: Real and reciprocal space structure of the adsorbate. (a) Tiling of the dense-fluid phase ($I_0 = 0$). (b) $S(q_x, q_y)$ calculated for data shown in (a). The scale is exponential. (c,d) Same as (a,b) for $I_0 = 0.35\ \mu\mathrm{W}\mu\mathrm{m}^{-2}$. The scale bar is 50 μm.

For $I_0 = 1.4\ \mu\mathrm{W}\mu\mathrm{m}^{-2}$, however, we observe a clear increase in the number of pentagonal tiles which become more localized. These tiles adapt the same orientations of the pentagonal structures of the underlying substrate potential (Fig. 4.3a). The arrangement of these tiles leads to the formation of 20 Bragg peaks with 10-fold symmetry in the corresponding diffraction pattern (Fig. 4.3b). This is a clear indication that the particles have partially adapted the symmetry of the substrate.

For $I_0 = 2.8\ \mu\mathrm{W}\mu\mathrm{m}^{-2}$, the particle configuration seen in Fig. 4.3c changes greatly in comparison with Fig. 4.3a. The tiling here consists of a large number of pentagonal tiles arranged on circles and which have two orientations (pointing up and down). This ordering is typical to the underlying substrate potential. The corresponding diffraction pattern also shows perfect quasicrystalline order and thus mimics the geometry of the underlying light potential (Fig. 4.3d).

The increase observed for the pentagonal tiles is quantitatively confirmed in Fig. 4.4. Here, the number density of the local particle configurations (or tiles) ρ_n^T is

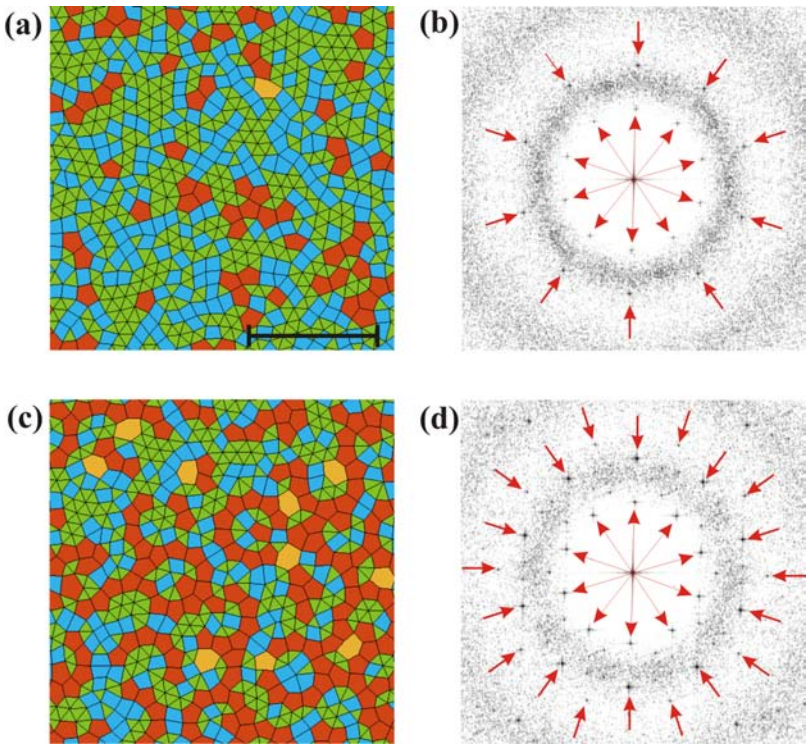

Figure 4.3: Real and reciprocal space structure of the adsorbate. (a) Tiling of the fluid-decagonal phase for $I_0 = 1.4\ \mu\mathrm{W}\mu\mathrm{m}^{-2}$. (b) $S(q_x, q_y)$ calculated for data shown in (a). (c) Tiling of the decagonal phase for $I_0 = 2.8\ \mu\mathrm{W}\mu\mathrm{m}^{-2}$. (d) $S(q_x, q_y)$ calculated for data shown in (c). The scale bar is 50 μm.

calculated for different I_0. At low intensities, 76% of the tiles are triangular (ρ_3^T), 22% are quadratic (ρ_4^T) and only 1% are pentagonal (ρ_5^T). Since the underlying substrate potential does not support the triangular tiles, an increase in the laser intensity I_0 is accompanied by a decrease of ρ_3^T. Even at high intensities, at which ρ_5^T increases, ρ_4^T stays constant.

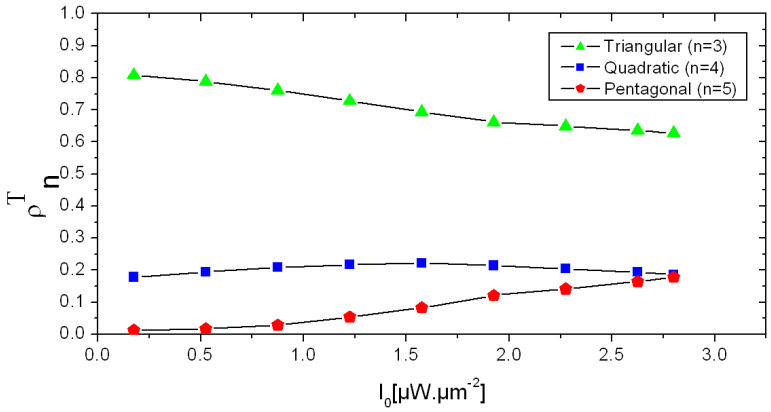

Figure 4.4: Number density of the tiles. n is the edge number, i.e. n=3 for triangular tiles, n=4 for quadratic tiles and n=5 for pentagonal tiles.

One can then deduce that the structural phase transition from a dense-fluid phase to a decagonal quasiperiodic phase involves the formation of pentagonal tiles which leads to a destruction of only the triangular tiles while the quadratic tiles number density stays intact.

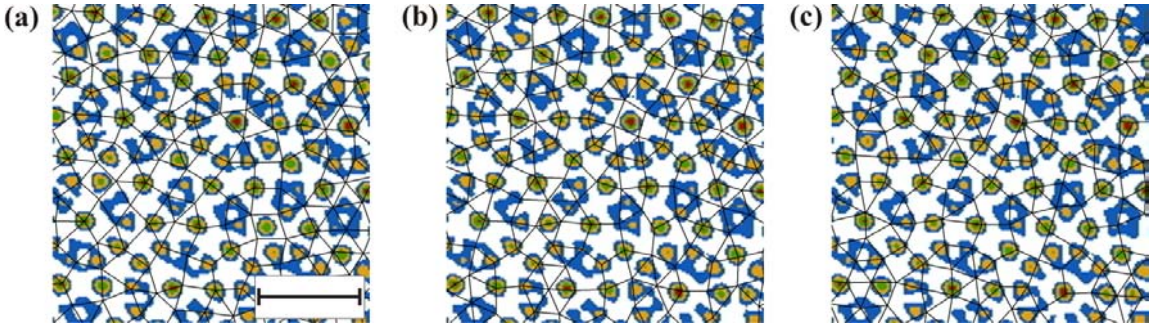

Figure 4.5: Tilings for different laser intensities superimposed on the laser intensity distribution of the decagonal interference pattern. (a) $I_0 = 0.35\ \mu\mathrm{W}\mu\mathrm{m}^{-2}$. (b) $I_0 = 1.4\ \mu\mathrm{W}\mu\mathrm{m}^{-2}$. (c) $I_0 = 2.8\ \mu\mathrm{W}\mu\mathrm{m}^{-2}$. The scale bar is 20 μm.

To understand how the observed phases form on the quasicrystalline substrate, we plot in Fig. 4.5 the contours of the tiles taken from Fig. 4.2 and 4.3 (black lines) on top of the decagonal intensity distribution of the laser field. At low intensities (Fig. 4.5a), only few particles coincide with deep potential wells. However almost none of the observed tiles are supported by the substrate potential. At higher laser power

(Fig. 4.5b), the deepest potential wells of the substrate coincide with vertices. The pentagonal tiles are clearly supported by the underlying substrate potential especially around the high symmetry star (HSS). The HSS corresponds to a deep potential minimum that is surrounded by 10 shallower potential wells. For $I_0 = 2.8$ μWμm^{-2} (Fig. 4.5c), almost all the vertices coincide with potential wells and thus show quasicrystalline order.

4.3 Transition from a triangular crystalline phase to a decagonal phase

In this experiment the colloid density $\phi = 0.0324$ μm^{-2} is increased compared to the measurement in section 4.2. At this density spontaneous crystallization is observed. In the absence of the quasiperiodic light potential, the particles thus adapt a triangular structure with long range order and a mean particle distance $A = 5.97$ μm. The sample is later exposed to an interference pattern with characteristic length scale $a_v = 8.53$ μm thus $A/a_v = 0.70$. The laser intensity I_0 is stepwise increased.

For laser intensities below $I_0 = 2.0$ μWμm^{-2}, the tiling of the colloidal crystal consists only of triangular tiles (data not shown). The pair-interaction is much stronger than the particle-substrate interaction and the crystal remains intact. The first defects occur at $I_0 = 2.45$ μWμm^{-2}. Apart from few pentagonal and hexagonal tiles, Fig. 4.6a shows the formation of many quadratic tiles. The crystalline structure is confirmed by the diffraction pattern, which has 6-fold coordinated spots (Fig. 4.6b). The broadening of the peaks is due to the quadratic defects. The intensity of the peaks decreases with increasing diffraction order, reflecting the thermal motion of particles. By increasing the intensity of the quasicrystalline light field, the particle-substrate interaction becomes stronger, and the equilibrium structure will change. Fig. 4.6c shows the situation for $I_0 = 3.15$ μWμm^{-2}. Surprisingly, a high number of quadratic tiles is observed while the number of pentagonal tiles remains almost constant. Many of these quadratic tiles arrange in chain-like structures (rows) whose orientation is given by one of the three high symmetry directions of the crystal. One can also notice the alignment of crystalline domains along specific directions corresponding to the high symmetry directions of the quasicrystalline substrate (red lines). This is in agreement with observations of Xenon atoms adsorbed on the ten-fold decagonal Al-Ni-Co surface [98] and numerical simulations of weakly adsorbed atomic systems where the colloidal repulsion dominates over the colloid-substrate interaction [32]. In addition to the 6-fold coordinated spots, the structure factor in Fig. 4.6d shows the formation of 10-fold coordinated spots with different intensities. Interestingly, the spots corresponding to the high symmetry directions of the crystal are more pronounced (red arrows).

Only at $I_0 = 4.55$ μWμm^{-2}, we observe a clear increase in the number of pentagonal tiles having two orientations as expected from the underlying substrate potential (Fig. 4.7a). The formation of these tiles destroys the quadratic rows and leads to the

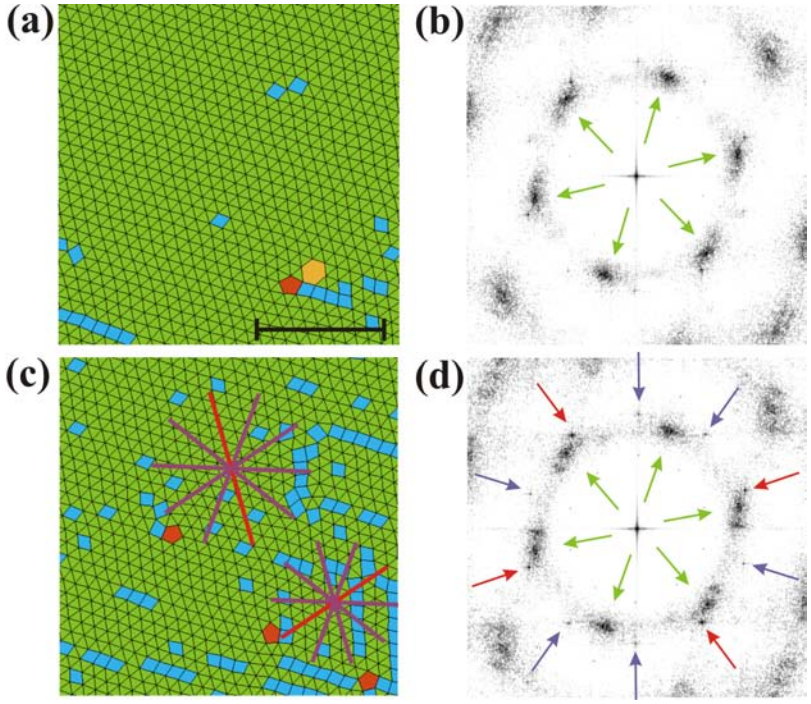

Figure 4.6: Real and reciprocal space structure of the adsorbate. (a) Tiling of the crystalline phase for $I_0 = 2.45$ μWμm^{-2}. The scale bar is 50 μm. (b) Plot of $S(q_x, q_y)$ calculated for data shown in (a). The green arrows point at the 6-fold coordinated spots, typical for a triangular crystalline phase. The scale is exponential. (c) Tiling of the particle configuration at $I_0 = 3.15$ μWμm^{-2}. The lines indicate the orientations of the underlying lattice. The red lines indicate the direction adapted by the crystal. (d) $S(q_x, q_y)$ calculated for data shown in (c). The red and violet arrows point at 10-fold coordinated spots with different intensities.

increase observed for Ψ_{10}. The corresponding diffraction pattern (Fig. 4.7b) shows at this stage the formation of 10-folded Bragg peaks. Even the highest available laser intensity, $I_0 = 6.475\ \mu\mathrm{W}\mu\mathrm{m}^{-2}$, is obviously not enough to destroy all triangular tiles. Fig. 4.7c shows the tiling for this intensity, which consists of triangular, quadratic, and pentagonal tiles. Nevertheless, the diffraction pattern in Fig. 4.7d shows a higher order of quasicrystallinity indicating that a large number of the particles has adapted the symmetry of the substrate.

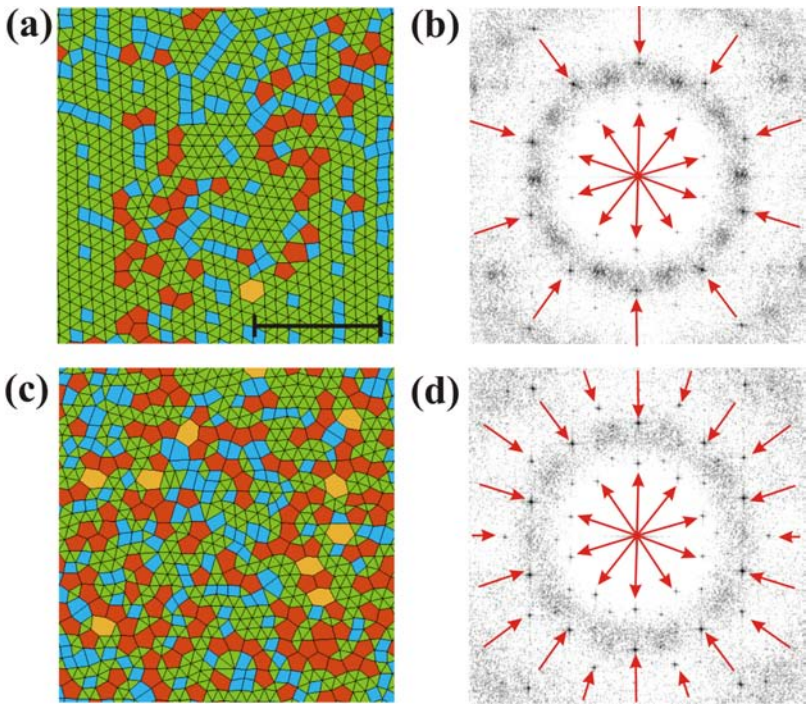

Figure 4.7: Real and reciprocal space structure of the adsorbate. (a) Tiling of the crystal-decagonal phase for $I_0 = 4.55\ \mu\mathrm{W}\mu\mathrm{m}^{-2}$. (b) $S(q_x, q_y)$ calculated for data shown in (a). (c) Tiling of the decagonal phase for $I_0 = 6.475\ \mu\mathrm{W}\mu\mathrm{m}^{-2}$. (d) $S(q_x, q_y)$ calculated for data shown in (c). The scale bar is 50 μm.

In Fig. 4.8, the number density of the tiles ρ_n^T is calculated for different I_0. With increasing intensity, the number density of triangular tiles decreases. This leads to the destruction of the 6-fold symmetry. While first ρ_5^T stays almost constant below 0.1, the number density of the quadratic tiles ρ_4^T increases and reaches a saturation value for $I_0 = 3.85\ \mu\mathrm{W}\mu\mathrm{m}^{-2}$. This obviously corresponds to a first stage in the phase transition. Only for $I_0 = 4.55\ \mu\mathrm{W}\mu\mathrm{m}^{-2}$, ρ_5^T starts to increases suggesting a second stage.

These data show that the structural phase transition of a triangular crystal interacting with a decagonal light pattern is different compared to the previous case. Here, two stages in the phase transition are involved. At low laser intensities, quadratic tiles mainly arranged in rows along the high symmetry axis of the crystal are formed. The positional order of the particles perpendicular to these rows is disturbed and a one-dimensional periodic ordering along the rows is conserved. At a second stage,

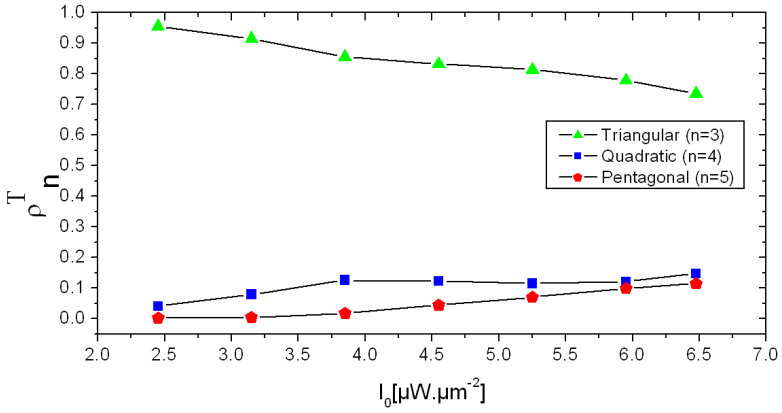

Figure 4.8: Number density of the tiles. n is the edge number, i.e. n=3 for triangular tiles, n=4 for quadratic tiles and n=5 for pentagonal tiles.

many of the local particle configurations become pentagonal and the crystalline order is destroyed. This leads to the proliferation of the quasicrystalline order.

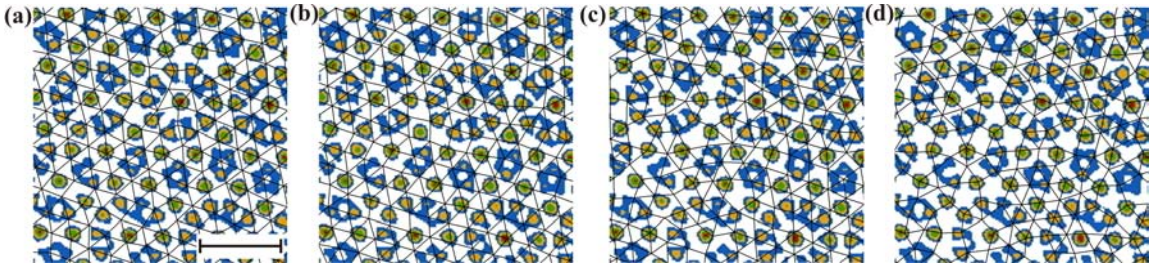

Figure 4.9: Tilings for different laser intensities superimposed on the laser intensity distribution of the decagonal interference pattern. (a) $I_0 = 2.45$ μWμm^{-2}. (b) $I_0 = 3.15$ μWμm^{-2}. (c) $I_0 = 4.55$ μWμm^{-2}. (d) $I_0 = 6.475$ μWμm^{-2}. The scale bar is 20 μm.

To understand how the observed phases form on the decagonal potential, we plot in Fig. 4.9 the contours of the tiles taken from Fig. 4.6 and 4.7 (black lines) on top of the decagonal intensity distribution of the laser field. At low intensities (Fig. 4.6a), most of the vertices do not coincide with potential wells. For $I_0 = 3.15$ μWμm^{-2}, the tiling shows many rows of quadratic tiles. These rows, as seen in Fig. 4.6c, form due to the electrostatic repulsion between the colloids. At higher intensities (Fig. 4.7), a high number of the particles is trapped by the deep potential wells leading to the formation of the pentagonal tiles.

In Fig. 4.10 an illustrative scheme for the formation of the quadratic rows is presented. Only at a critical laser intensities, colloids start to be attracted to deep potential wells and individual particles are displaced from their initial position in the crystalline structure (Fig. 4.10a). This displacement leads to a local formation of a defect, and the surrounding colloids adjust their position in order to maximize the

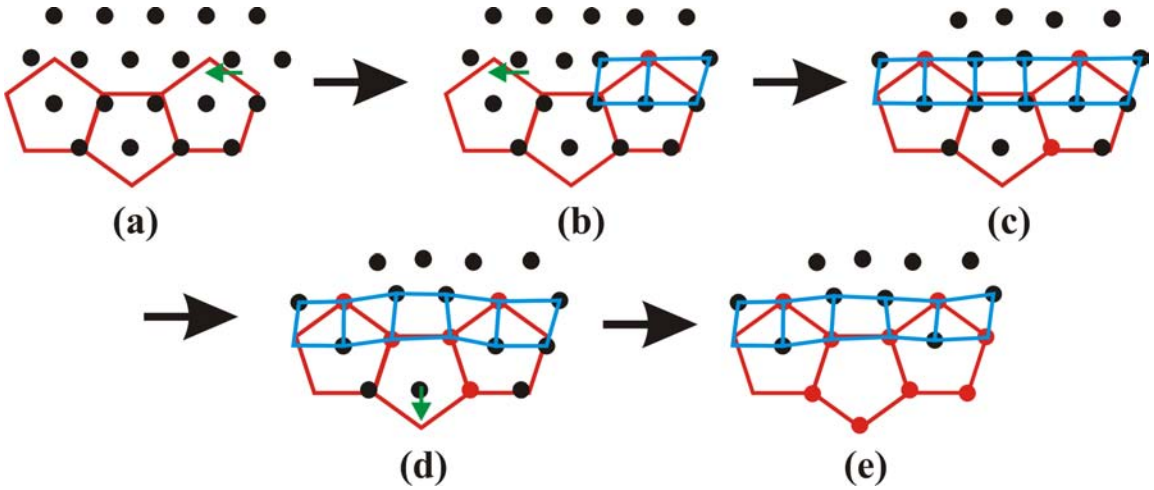

Figure 4.10: Scheme illustrating the formation of quadratic rows. (a) A particle (black point) is pushed towards a potential well (vertex of a red pentagons). (b) Due to the electrostatic repulsion the neighboring particles form quadratic tiles to maximize the inter-particle distances. (c) If the same phenomena happens for another particle on the same line a row of quadratic tiles is formed. (d,e) Here the ordering propagates perpendicular to the rows and pentagonal tiles are formed.

interaction energy (Fig. 4.10b). This leads to the formation of two adjacent quadratic tiles (in blue). The formation of such defects in the crystalline structure will lead to a particle rearrangement, and deep potential wells attract other neighboring particles (Fig. 4.10c). Through this mechanism the quadratic rows increase their length. At a higher critical laser intensity, the potential wells are deep enough to create pentagonal tiles and destroy the crystalline ordering perpendicular to the rows (Fig. 4.10d,e).

One can then deduce, that the structural phase transition from a periodic triangular phase to a decagonal quasiperiodic phase involves two stages. First quadratic local configurations forming rows along the high symmetry axis of the crystal are formed. At a later stage, characterized by a critical laser intensity, pentagonal tiles starts to nucleate and the quasiperiodic order proliferates. In the next section, we check whether this phase behavior is conserved for even higher densities.

4.4 Intermediate archimedean-like tiling phase

In this experiment a colloidal system with a higher density $\phi = 0.038\ \mu m^{-2}$ is prepared (particle radius $R = 1.95\ \mu m$). As before, in the absence of the quasiperiodic light potential the system crystallizes thus the particles adapt a triangular structure. Although the measurement procedures are not altered, we observe a progressive increase of the particle density in the field of view at low laser intensities. As seen in Fig. 4.11, the increase is about 8% and the density stays almost constant for $I_0 > 1.25\ \mu W \mu m^{-2}$ with a value of $\phi = 0.0406\ \mu m^{-2} \pm 1.5\%$. The reason of the den-

sity change will be explained later. For $\phi = 0.0406\ \mu m^{-2}$, the mean particle distance is $A = 5.29\ \mu m$ thus $A/a_v = 0.62$. The laser intensity I_0 is stepwise increased.

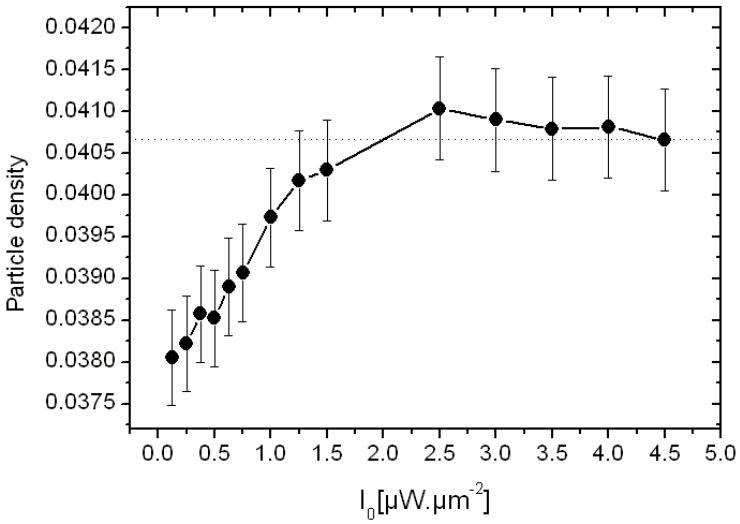

Figure 4.11: Increase in the particle density in the field of view at low laser intensities. For $I_0 > 1.25\ \mu W \mu m^{-2}$ the density variation stays below 1.5% with an average value of $\phi = 0.0406\ \mu m^{-2}$ (dashed line).

4.4.1 Identification of the phases

Fig. 4.12 and 4.13 show how the particle configuration and the structure factor change when the substrate strength of the decagonal substrate is increased. The periodic crystal shown in Fig. 4.12a can be described by a triangular lattice (green triangular tiles). The electrostatic colloidal repulsion dominates over the colloid-substrate interaction and the crystalline structure remains mainly intact. Also here, we observe the alignment of the crystalline domain along one of the 5-fold directions of the quasicrystalline substrate. Apart from some defects, each vertex is surrounded by six triangular tiles forming a (3^6)-vertex type where 3 represents a triangle and 6 is the number of triangles surrounding the vertex. The crystalline structure is confirmed by the diffraction pattern, which has 6-fold coordinated spots leading to periodically spaced peaks in the projected diffraction pattern $\bar{S}(q_x)$. The intensity of the peaks decreases with increasing diffraction order, reflecting the thermal motion of particles.

When I_0 is increased to $I_0 = 2.5\ \mu W \mu m^{-2}$, the particles also strongly interact with the corresponding surface potential, and the equilibrium structure changes. As shown in Fig. 4.6c, the tiling of the colloidal system does not only consist of triangular tiles. The particle-substrate interaction is strong enough to create geometrical defects in the crystal. The observed structure shows neither a triangular nor a deca-

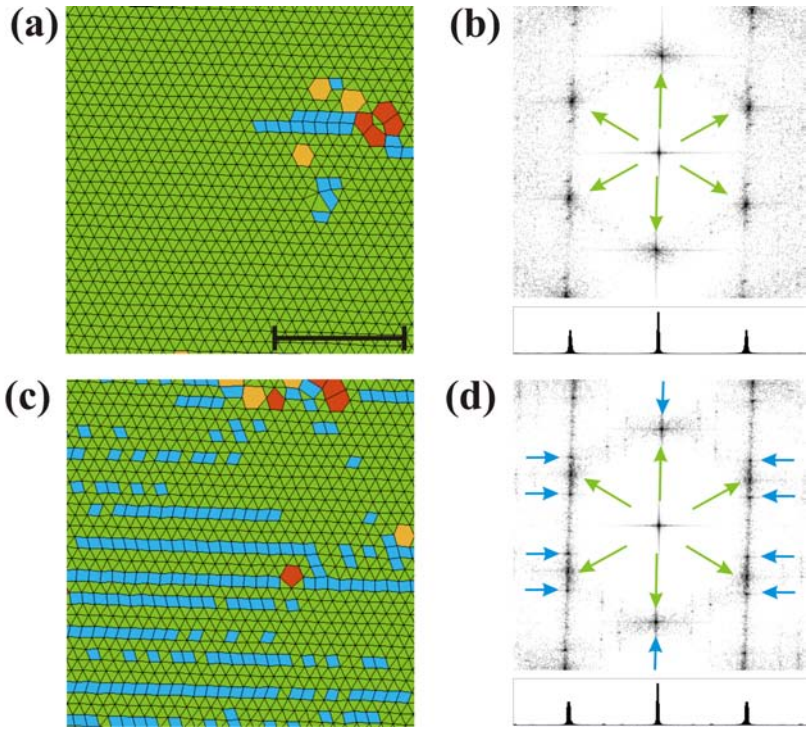

Figure 4.12: Real and reciprocal space structure of the adsorbate. (a) Tiling of the crystalline phase for $I_0 = 1.5\ \mu\mathrm{W}\mu\mathrm{m}^{-2}$. The scale bar is 50 µm. (b) $S(q_x, q_y)$ calculated for data shown in (a) and projection $\bar{S}(q_x)$. The green arrows point at the 6-fold coordinated spots, typical for a triangular crystalline phase. The scale is exponential. (c) Tiling of the particle configuration at $I_0 = 2.5\ \mu\mathrm{W}\mu\mathrm{m}^{-2}$. (d) $S(q_x, q_y)$ and $\bar{S}(q_x)$ calculated for data shown in (c). The blue arrows indicate the peaks occurring due to the quadratic rows.

gonal symmetry. In contrast with the triangular structure which consists of mainly triangular tiles, here long rows of quadratic tiles start to form. These rows are mainly aligned along the horizontal which is a high symmetry axis for the crystalline structure and the underlying substrate potential. The structure factor in Fig. 4.7d shows strong peaks (blue arrows) aligned along the q_y direction. The position of these peaks coincides with positions of peaks expected for the decagonal phase.

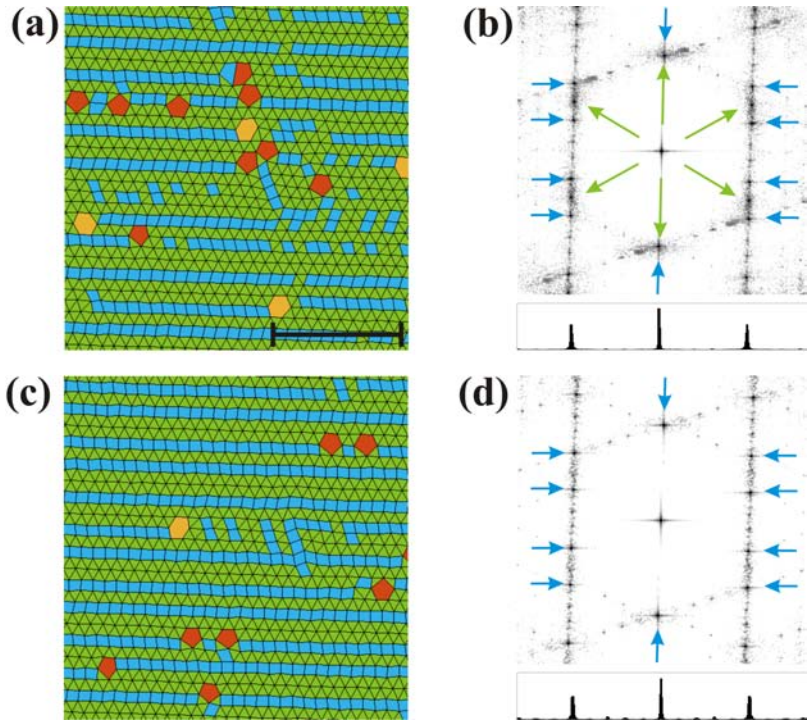

Figure 4.13: Real and reciprocal space structure of the adsorbate. (a) Tiling of the intermediate phase for $I_0 = 3\ \mu\mathrm{W}\mu\mathrm{m}^{-2}$. (b) $S(q_x, q_y)$ and $\bar{S}(q_x)$ calculated for data shown in (a). (c) Tiling of the intermediate phase for $I_0 = 4\ \mu\mathrm{W}\mu\mathrm{m}^{-2}$. (d) $S(q_x, q_y)$ and $\bar{S}(q_x)$ calculated for data shown in (c). The scale bar is 50 µm.

As seen in Fig. 4.13, the increase of the laser intensity leads to an elongation in the length of the quadratic rows, and an almost perfect ordering along the horizontal with some intrusions at an angle of 72°. The structure in fig. 4.13c is well characterized by a tiling composed of squares (blue) and triangles (green). The peaks in the corresponding $S(q_x, q_y)$ are periodically spaced along the q_x direction (as clearly seen in the projection $\bar{S}(q_x)$), whereas in the q_y direction their distance is close to the golden ratio τ. This is a clear signature of quasicrystalline order along the y direction. Obviously, the competition between the colloid-colloid repulsion and their interaction with the quasicrystalline substrate leads at these particle densities to an ordered phase that has both periodic and quasicrystalline structural properties.

In Fig. 4.15, the number density of the tiles ρ_n^T is calculated for different I_0. The global behavior is rather similar to what has been observed in the previous

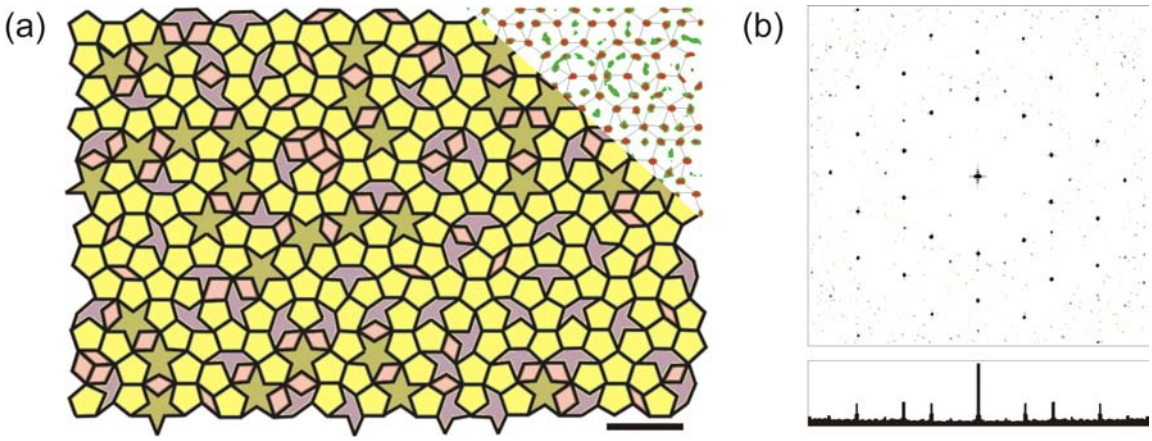

Figure 4.14: Real and reciprocal space structure of the adsorbate with screened electrostatic interaction ($\phi = 0.046\ \mu m^{-2}$, $I_0 = 2\ \mu W \mu m^{-2}$, $\kappa \approx 10nm$, $R = 1.45 \mu m$). (a) Particle density distribution and tiling composed of pentagons (yellow), rhombuses (pink), crowns (violet) and pentagonal stars (brown). $I_0 = 4.55\ \mu W \mu m^{-2}$. (b) $S(q_x, q_y)$ with 10-fold symmetry calculated for data shown in (a) and the projection $\bar{S}(q_x)$. The scale bar is 20 μm

measurement. With increasing intensity, the number density of triangular tiles decreases. Almost no pentagonal tiles are formed along the whole measurement. Instead, the number density of quadratic tiles (ρ_4^T) increases and reaches a value of 27% at $I_0 = 4\ \mu W \mu m^{-2}$.

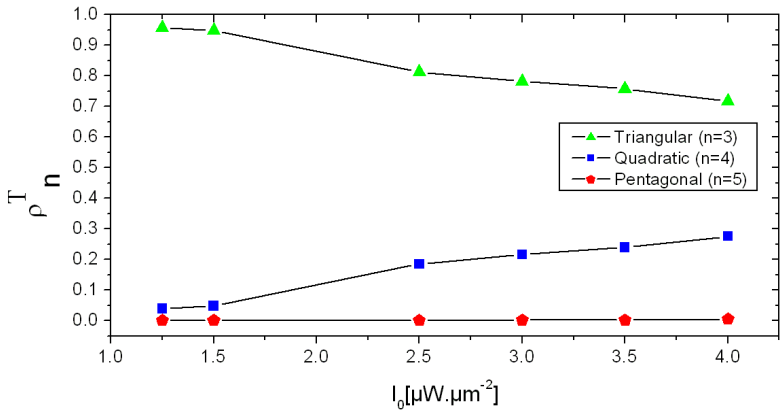

Figure 4.15: Number density of the tiles. n is the edge number, i.e. n=3 for triangular tiles, n=4 for quadratic tiles and n=5 for pentagonal tiles.

Also in this situation, one can then deduce that the structural phase transition involves the occurrence of an intermediate phase. And the question is whether the spatial ordering of the quadratic tiles is different than the one observed at lower densities.

Before analyzing this new intermediate phase in more detail, we discuss the observation when the colloid-substrate interaction dominates even at high particle densities (Fig. 4.14). This is achieved by preparing a colloidal system with particle density $\phi = 0.046\ \mu\text{m}^{-2}$ and a high ionic strength ($\kappa \approx 10nm$) which greatly reduces the repulsion between the colloids. For $I_0 = 2\ \mu\text{W}\mu\text{m}^{-2}$, the particle density distribution $\rho(x, y)$ follows a tiling consisting of prototiles shaped like rhombuses, pentagons, crowns and stars. Such tiles are known from the P1 Penrose tiling and have also been applied successfully to the 5-fold surface of AlPdMn [8]. The corresponding diffraction pattern shows perfect quasicrystalline order and thus mimics the geometry of the underlying light potential. As expected, $\bar{S}(q_x)$ consists of peaks whose distances are not equal but are given by τ.

4.4.2 Orientation of the intermediate phase

The direction of the quadratic rows varied between different experiments but always corresponded to one of the five orientations given by the substrate potential. The analysis of the static phason strain occurring in the underlying substrate (for details see 3.5.4) has shown that this orientation is correlated with the density of jaggs which varies for the five directions of the pattern.

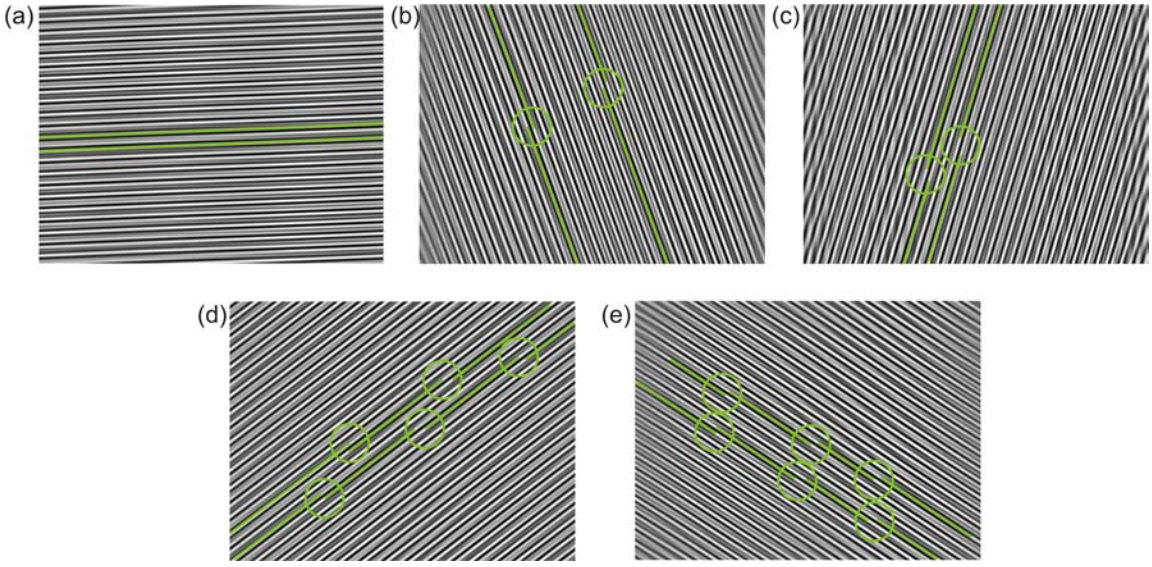

Figure 4.16: (a-e) Back Fourier transforms of two pairs of Bragg peaks at τ related wavevectors for the five directions of the patterns (for details refer to 3.5.4). The resulting intensity distribution image is formed out of stripes without jaggs (a) and with jaggs (b-e) indicated by green circles. This is due to the existence of local rearrangements with respect to a perfect pattern.

The density of the jaggs can be seen in the back-Fourier transforms of two pairs of Bragg peaks at τ related wavevectors (for details refer to 3.5.4). The resulting intensity distribution images are formed out of stripes with jaggs (green circles)

indicating the existence of local rearrangements with respect to a perfect pattern. As shown in Fig. 4.16, along the horizontal direction the bright lines are continuous without any jaggs, in contrast to the other 4 directions.

4.4.3 Macroscopic description

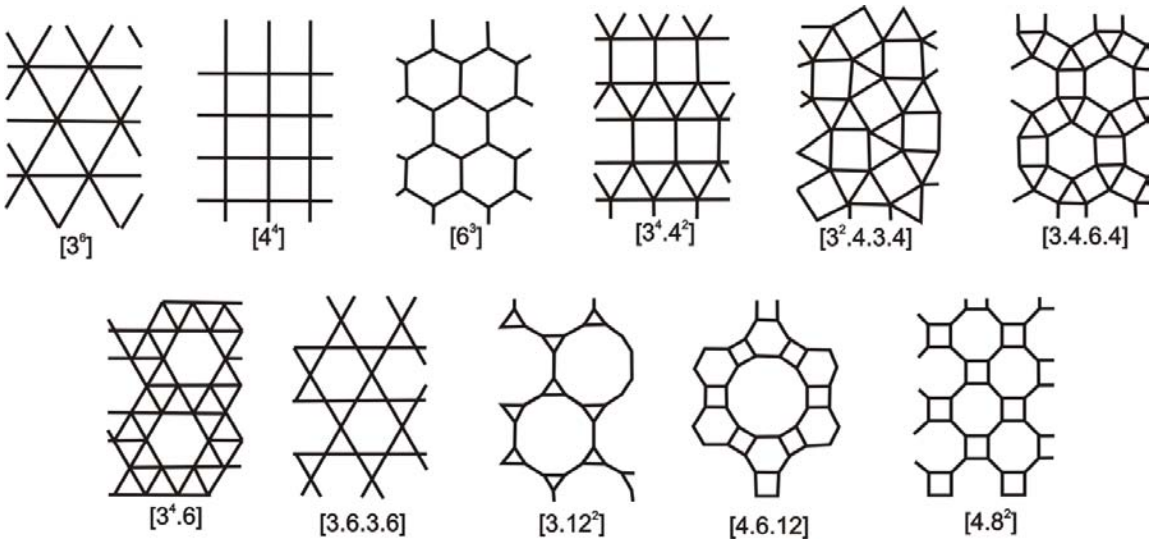

Figure 4.17: The eleven archimedean tiling structures. The tilings are composed of regular convex polygons that are not necessarily identical, but identically arranged around each vertex. The archimedean tilings include the traditional Bravais lattices. The tilings are denoted by a set of integers and superscripts ($n_1^{p_1}.n_2^{p_2}...$) referring to the vertex type (p n-gons meet on each vertex).

The structure of the intermediate phase is remarkably similar to one of the 11 archimedean tilings first introduced by Kepler in 1619 [1]. Currently, there is renewed interest in archimedean tilings as candidates for photonic crystals [100]. In contrast to the five two-dimensional Bravais lattices each described by identical tiles (being the corresponding unit cell), archimedean tilings may be composed of more than one, but regular, tile. Those tiles are arranged in such a way that only one vertex type exists (Fig. 4.17). Fig. 4.18a shows an example of an archimedean tiling consisting of alternating rows of triangular and quadratic tiles. Because each vertex is surrounded by three triangles and two squares, this leads to a $(3^3.4^2)$-vertex type. Although the structure is strictly periodic, it has marked similarities with quasicrystals. First, every vertex has five nearest neighbors at equal distances that form an irregular pentagon. Second, the structure of the archimedean tiling is equivalent to an oblique lattice (red lines) with a two-atomic basis. The oblique angle $\gamma = 75°$ is close to the value of 72° on decagonal substrates. Accordingly, when superimposing ideal pentagons (white lines) on the archimedean tiling, their vertices (and the center of the bigger one) agree almost perfectly with the vertex positions. The height ratio of these pentagons equals the golden ratio τ.

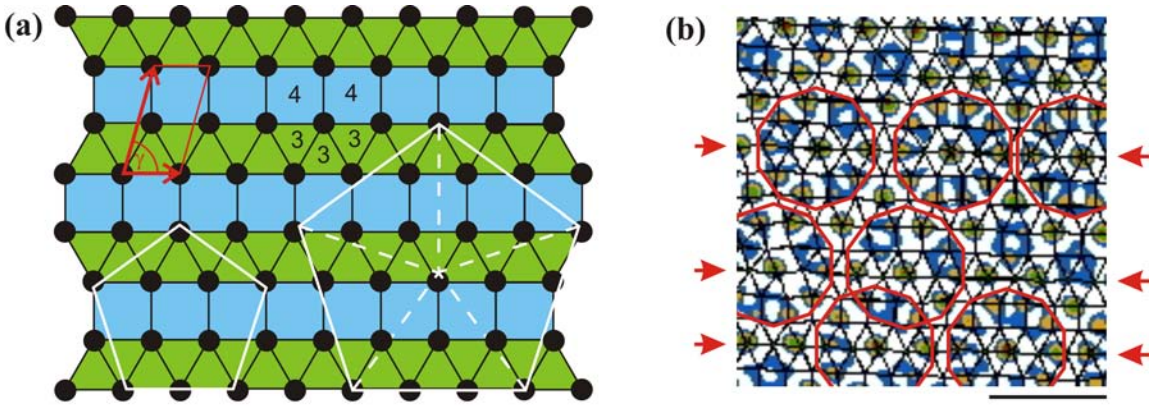

Figure 4.18: Substrate-adsorbate correlations. (a) Ideal archimedean tiling with $(3^3.4^2)$ vertex type. The vertices and centers of the two pentagons (white) fit the lattice sites almost perfectly. The structure can be also represented by an oblique lattice with two atoms per unit cell (red). (b) Tiling of the intermediate phase superimposed on the laser intensity distribution of the decagonal interference pattern. Particles are partly located at deep minima in substrate potential. Other colloids are located at interstitial sites with weak substrate interactions. The red decagons indicate the high symmetry stars (HSS) where double triangular rows are observed (red arrows). The scale bar is 20 µm.

To understand how the observed intermediate phase forms on the quasicrystalline substrate, we plotted the contours of the tiles taken from Fig. 4.13c (black lines) on top of the decagonal intensity distribution of the laser field (Fig. 4.18b). The deepest potential wells of the substrate coincide with vertices and thus show quasicrystalline order. For our particle density, this applies to about half of all vertex positions. The other vertices are located at sites with weak or vanishing substrate interactions, and their configuration is dominated by electrostatic particle repulsion. They therefore assemble in such a way that their nearest-neighbor distance is fairly uniform. As a result, vertices partly adopt a 10-fold rotational symmetry but simultaneously seek to achieve equal nearest-neighbor distances. Both aspects are ideally supported by the archimedean tiling. Because archimedean tilings are strictly periodic, they can be only locally commensurate with quasicrystalline substrates; disruptions at larger length scales must occur. In Fig. 4.19 we show the tiling of a larger cut. Remarkably, one can observe the alignment along two directions of large domains. These domains show additional interstitial rows of triangles (that is, double triangular rows). As a result, two vertex types, namely $(3^3.4^2)$ and (3^6), arise. Such structures are referred to as archimedean-like tilings [100]. One would expect that the spacing of those interstitial rows corresponds to a Fibonacci sequence, taking into account the long range quasicrystalline order along one direction. This is consistent with the structure observed in Fig. 4.19. The origin of the two characteristic length scales of such a Fibonacci chain is due to the fact that the double triangular rows nucleate along

rows in the pattern where high symmetry stars HSS are present (Fig. 4.18b). The sequence of these HSS along e.g. the vertical direction follows indeed the Fibonacci sequence.

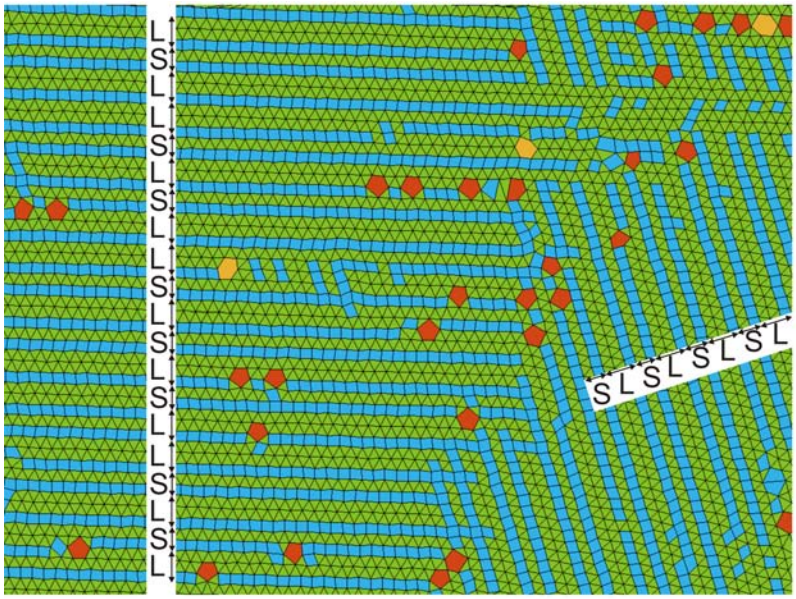

Figure 4.19: Tiling of a larger cut showing the formation of the intermediate archimedean-like tiling aligned along two directions making an angle of 72°. Along each direction a part of the Fibonacci sequence of long (square-triangle-triangle) and short (square-triangle) stripes is observed.

4.4.4 Density dependence

We also investigated whether the intermediate phase is stable with other parameters. Fig. 4.20 shows the result when a colloidal layer with density $\phi = 0.030\ \mu\text{m}^{-2}$ is exposed to a decagonal substrate potential whose characteristic length scales is decreased to $a_v = 7.8\ \mu\text{m}$ thus $A/a_v = 0.79$.

In contrast to the above, here the number of deep potential wells provided by the substrate is larger than the number of vertices. Nevertheless, the structure of the system is again well described by an archimedean-like tiling and even though the magnitude of particle fluctuations relative to the substrate is stronger than in the previous case, the diffraction pattern (Fig. 4.20b) agrees well with that in Fig. 4.13d. This suggests that the intermediate phase forms for a wider range of parameters.

Obviously this intermediate phase can occur at different densities for which a high number of particles is located in a potential well and subsequently the average potential energy is minimized. Schmiedeberg et al. calculated how this average potential energy varies with density when the particles adapt a triangular structure and when they adapt the archimedean-like tiling structure in the presence of the decagonal substrate potential [104]. From Fig. 4.21 one can clearly identify two

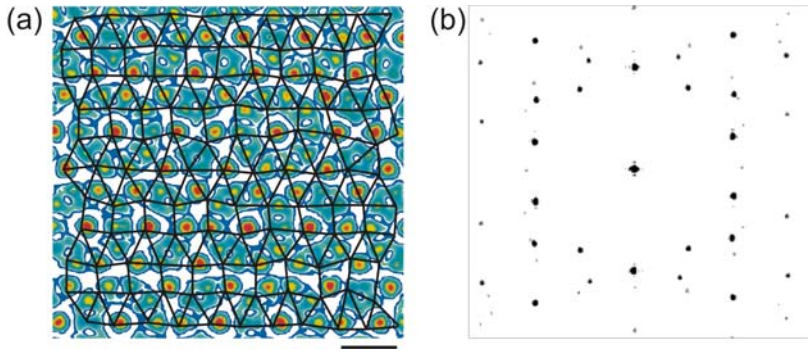

Figure 4.20: (a) Tiling of the intermediate phase occurring at different parameters. The tiling is superimposed on the laser intensity distribution of the decagonal interference pattern. The particle density is $\phi = 0.030\ \mu m^{-2}$, and the pattern characteristic length scales is decreased to $a_v = 7.8\ \mu m$. (b) Structure factor of (a).

densities where the archimedean-like tiling fits to the substrate perfectly and other densities at which the potential energy of the archimedean-like tiling phase is slightly lower compared to the triangular phase. The first deep minimum at $A/a_v = 0.58$ agrees well with the experimental data shown in Fig. 4.13 and proves that the change of density observed at low laser intensities is a result of the energy minimization. Most of the colloids are then located in minima of the potential and therefore the average potential energy exhibits a sharp minimum.

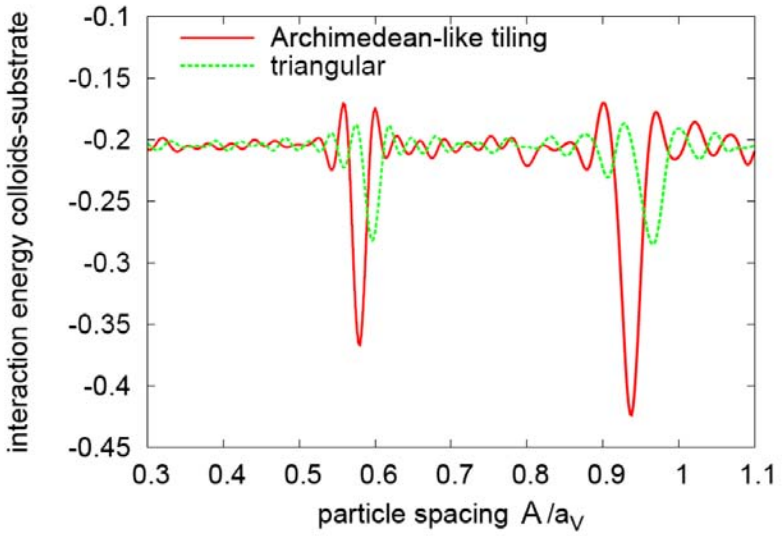

Figure 4.21: Average potential energy of a colloid in the decagonal potential calculated for a triangular and for an archimedean-like tiling structure as a function of density, which is given by the particle spacing A/a_V.

4.4.5 Numerical simulations

By using Monte Carlo simulations, Schmiedeberg et al. also studied the phase behavior of charged-stabilized colloidal particles in a two-dimensional substrate potential with quasicrystalline decagonal symmetry [105]. The colloidal structures were classified by the bond-orientational order parameter Ψ_m (m=6, 10 and 20). In the phase diagrams of Fig. 4.22(a,b) which show the respective phase diagrams for the low and high density cases, a m-fold bond order was assigned to the phases for $\Psi_m > 0.1$. For both cases, at low V_0 the phase transition from the triangular to the fluid phase is observed. At sufficiently large V_0, a quasicrystalline phase with 10-fold symmetry is favored by the decagonal potential. Interestingly, other phases occur for intermediate potential strengths. In the low density case (Fig. 4.22a), a quasicrystalline phase with pure 20-fold bond order is found, i.e., where $\Psi_{20} > 0.1$ but $\Psi_{10} < 0.1$. In the high density case (Fig. 4.22b), the intermediate phase does not display any bond-orientational order. For $A/a_v = 0.58$, a distinctive feature occurs and the archimedean-like tiling phase is observed.

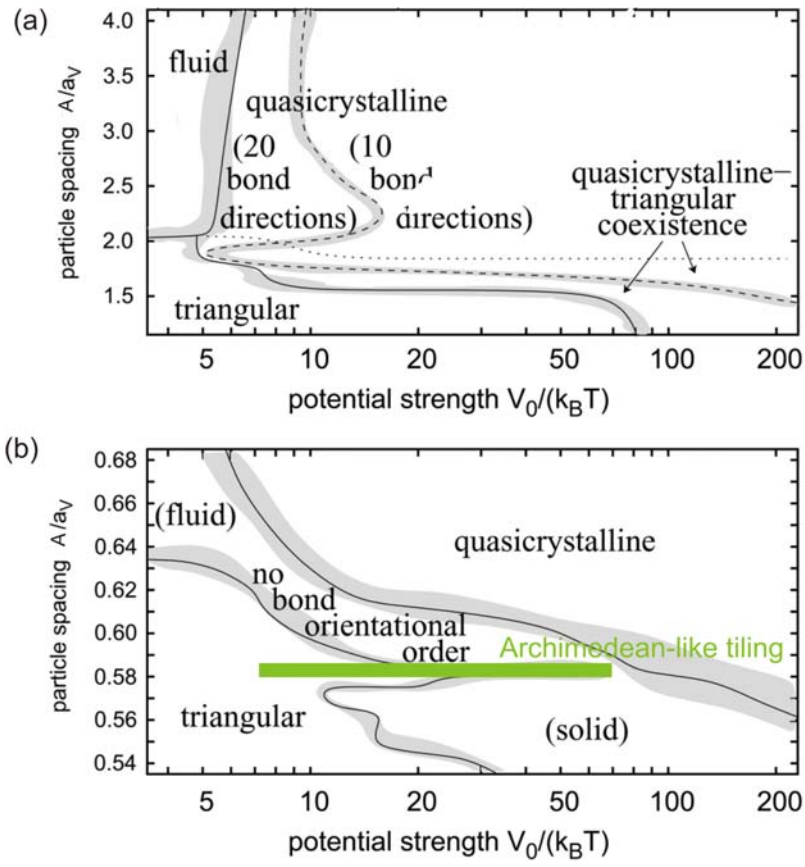

Figure 4.22: Phase diagrams for low (a) and high (b) colloidal densities depending on the potential strength V_0 (in units of k_BT) and the particle spacing A (in units of a_V) in an ideal triangular lattice. [105]

As seen in Fig. 4.23, also the simulation data show the formation of an archimedean-like tiling phase. A sequence that corresponds to 77 single or double rows of triangles was identified [104] and within this range the observed sequence is exactly the sequence of the Fibonacci chain, if one identifies a double row with L and a single row with S.

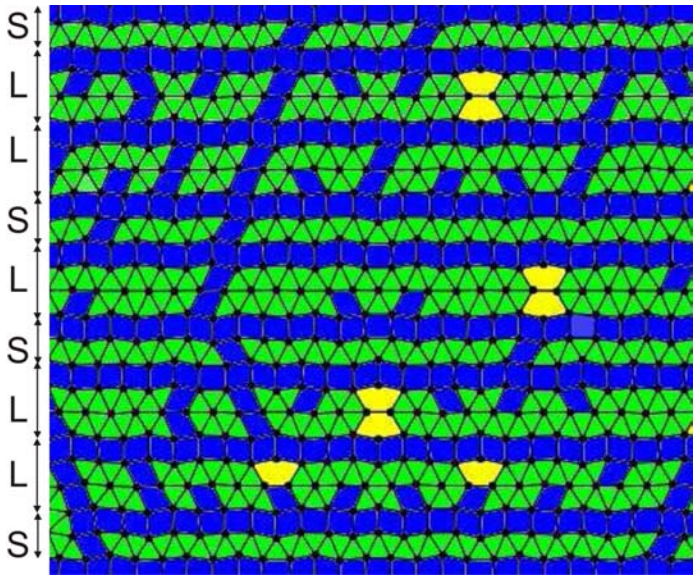

Figure 4.23: Archimedean-like tiling phases obtained by Monte Carlo simulations induced by a decagonal substrate. The figure shows a Delaunay triangulation of the colloidal coordinates where bonds longer than $1.1a_S$ are omitted. The potential strength is $V_0/(k_BT) = 20$ and the density is given by $A/a_V = 0.57$. Along the vertical direction a part of the Fibonacci sequence of long (square-triangle-triangle) and short (square-triangle) stripes is observed. [104]

4.4.6 Archimedean tiling phases in other systems

Because the phase behavior of colloidal monolayers on surfaces is similar to that of atomic systems [62], structures comparable to those observed in the colloidal systems are expected to occur in atomic adsorbates on quasicrystalline surfaces. Experiments with thin copper films deposited on the 5-fold surface of icosahedral AlPdMn quasicrystals reveal that above a few monolayers the copper atoms are arranged in rows spaced in a Fibonacci sequence [102, 42]. The atomic positions relative to the substrate have not yet been identified. However, although the atomic pair interactions in these experiments are more complex than in colloidal systems, the diffraction pattern of the copper film is almost identical to that of our intermediate phase (Fig. 4.24). This close resemblance suggests that the intermediate phase does not necessarily require complex substrate interactions but is driven by geometrical considerations and thus might also be observed for other adsorbate/quasicrystal combinations.

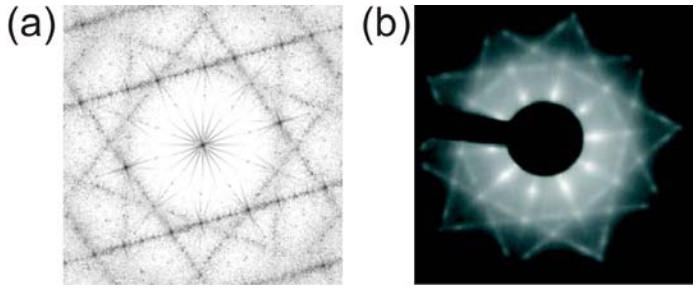

Figure 4.24: Comparison between colloidal and atomic systems. (a) Superposition of diffraction patterns taken from Fig. 4.13d and rotated by multiples of 72°. The result is in very good agreement with (b) the LEED pattern of the five-fold oriented domains of thin Cu films on quasicrystalline Al-Pd-Mn surfaces [102].

Similar Archimedean tiling was also lately observed for binary mixtures of nanoparticles situated between a cubic and a dodecagonal phase [49]. At the periphery of large quasicrystal domains observed in self-assembled system of binary nanoparticles (Fig. 4.25), a smooth transition between a decagonal quasiperiodic phase and a cubic phase was observed. The transition between the two topologically different phases was achieved through a region of $(3^3.4^2)$ archimedean tiling that matched both phases with a low concentration of interfacial defects. This demonstrates the unique feature of this phase with crystalline and quasicrystalline structural properties.

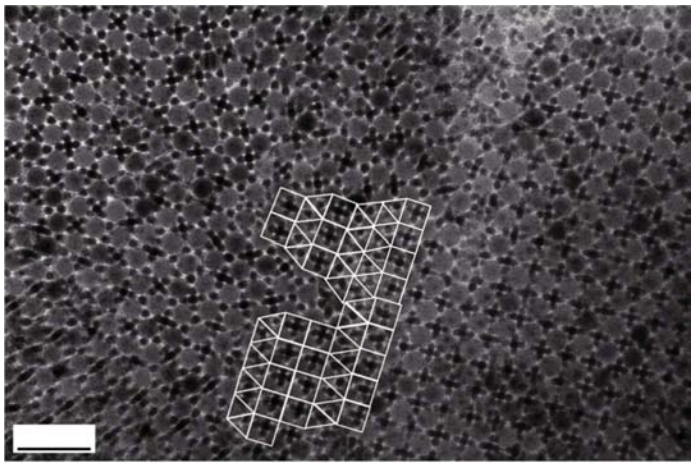

Figure 4.25: Structure of the interface between quasicrystalline and crystalline phases in a self-assembled system from 12.6 nm Fe_3O_4 and 4.7 nm Au nanocrystals. The transition from the dodecagonal phase to the cubic phase is facilitated by the presence of a $(3^3.4^2)$ Archimedean tiling [49].

4.5 Conclusion

Our experiments show that colloidal systems on decagonal light patterns allow us to understand the equilibrium structure of monolayers on quasicrystalline surfaces. We found that the phase transition from a triangular crystalline structure to a decagonal quasiperiodic phase occurs in two stages. First, rows of quadratic tiles are formed leading to a destruction of the local periodic ordering perpendicular to the rows. In a second stage, at a critical laser intensity, pentagonal tiles start to form and lead to the quasiperiodic ordering. We also found that for specific densities, the quadratic rows can be infinitely long and lead to the formation of a pseudomorphic phase that shows both crystalline and quasicrystalline structural properties. It can be described by an archimedean-like tiling consisting of alternating rows of square and triangular tiles. The calculated diffraction pattern of this phase is in agreement with recent observations of copper adsorbed on icosahedral $Al_{70}Pd_{21}Mn_9$ surfaces. In addition to establishing a link between archimedean tilings and quasicrystals, our experiments allow us to investigate in real space how single-element monolayers can form commensurate structures on quasicrystalline surfaces.

This approach can be also extended to investigate dynamical processes on quasicrystalline surfaces. By introducing phase shifts between the interfering laser beams, phason or phonon modes can be induced in the substrate. These elementary excitations are important for the three-dimensional growth of quasicrystals and it will be interesting to study how such substrate excitations modify the behavior of adsorbed thin films.

CHAPTER 5

FORMATION OF COLLOIDAL QUASICRYSTALS WITH ANOMALOUS SYMMETRIES

Despite a strong potential for numerous technical applications, the conditions under which quasicrystals form are still poorly understood [106, 4, 107, 108, 109, 110]. Currently, it is not clear why all two-dimensional quasicrystals are of a rank $\Delta = 4$ but no single example with $\Delta \geq 6$ has ever been observed [111, 112]. Here we report on geometrical constraints which impede the formation of quasicrystals with certain symmetries in a colloidal model system. This is achieved by subjecting a colloidal monolayer to N=5- and 7-beam quasiperiodic potential landscapes, i.e. $\Delta = 4$ and $\Delta = 6$ respectively. Our results clearly demonstrate that quasicrystalline order is much easier established for N = 5 compared to N = 7. With increasing laser intensity we observe that the colloids first adopt quasiperiodic order at local areas which then laterally grow until an extended quasicrystalline layer forms. As nucleation sites where quasiperiodicity originates, we identify highly symmetric motifs in the laser pattern. We find that their density strongly varies with n and surprisingly is smallest exactly for those quasicrystalline symmetries which have never been observed in atomic systems. Since such high symmetry motifs also exist in atomic quasicrystals where they act as preferential adsorption sites, this suggests that it is indeed the deficiency of such motifs which accounts for the absence of e.g. materials with 7-fold symmetry.

Interestingly, we also observe the formation of the same archimedean-like tiling phase (shown in the previous chapter) on the tetradecagonal potential at densities for which the potential energy of the colloidal system is minimized. Although the structure can also be described by rows of triangles and rows of squares, a closer analysis reveals substantial differences. Here, large domains with almost periodic ordering are found. We show that this behavior is closely related to the low density of the high symmetry motifs.

5.1 Peculiarity of quasicrystals with rank $\Delta = 6$

Although geometrical principles do not forbid structures with arbitrary rotational symmetry, experimentally only quasicrystals with 5-,8-,10-, 12-fold (axial symmetries) and icosahedral point group symmetries have been found [111]. Interestingly, for all axial symmetries, the minimum number of incommensurate wave vectors Δ (rank) required to span the reciprocal space is 4 and for the icosahedral symmetry $\Delta = 5$ (for details refer to 1.2.4). It is interesting to ask why e.g. solids with 7-fold rotational symmetry ($\Delta = 6$) do not exist because this will give insights into the mechanisms governing the formation of ordered matter in general.

According to some energetic-based considerations, it has been shown that if only the two-dimensional part of quasicrystals is taken into account, only those based on quadratic irrationalities should be energetically stable [113]. Consequently, only 5-, 8-, 10-, and 12-fold symmetries would be allowed. Nevertheless, three-dimensional quasicrystals, based on cubic irrationalities, such as 7- and 9-fold, would also be possible according to thermodynamics-based considerations [114].

Simple geometrical arguments can illustrate the peculiarity of quasicrystals with rank $\Delta = 6$ (Fig. 5.1) [112]. Starting with a pentagonal, hexagonal or heptagonal tile, one can construct 5-, 6- or 7-fold structures by iteratively adding identical clusters at the free edges. Although the building complexity of all three structures is quite similar, their decoration with atoms or molecules is not. Contrary to the 5-fold structure which leaves voids (white), the 7-fold structure causes overlaps of different shapes (green). Their atomic decoration becomes nontrivial due to steric hindrance. Similar, non-uniform overlaps, however, also occur for e.g. 8-fold structures (being indeed observed in atomic systems); therefore additional reasons for the absence of 7-fold quasicrystals must exist.

5.2 Comparison of the phase behavior of colloids on lattices with rank $\Delta = 4$ and $\Delta = 6$

Because there exist no regular or semiregular polyhedra with more than 5-fold symmetry, any quasicrystal with rank $R \geq 6$ will be comprised of periodically stacked quasicrystalline layers [115]. Therefore, in our work we search for hurdles that impede the formation of certain symmetries in two-dimensional systems. We create quasiperiodic potentials with rank $\Delta = 4$ and rank $\Delta = 6$. As described in 3, this is achieved by interfering N=5 and 7 laser beams. The resulting intensity patterns have 10- and 14-fold symmetry, i.e decagonal and tetradecagonal respectively.

Fig. 5.2 show the measured intensity distribution of quasiperiodic light patterns created from 5 and 7 laser beams which exhibit differently sized pentagonal and heptagonal structures. The characteristic length scales of both patterns has been adjusted to the same value of $a_v = 7.5$ µm.

In Figs. 5.3 and 5.4 we qualitatively compare how a colloidal system responds to these patterns as a function of the areal laser intensity I_0. The particle density

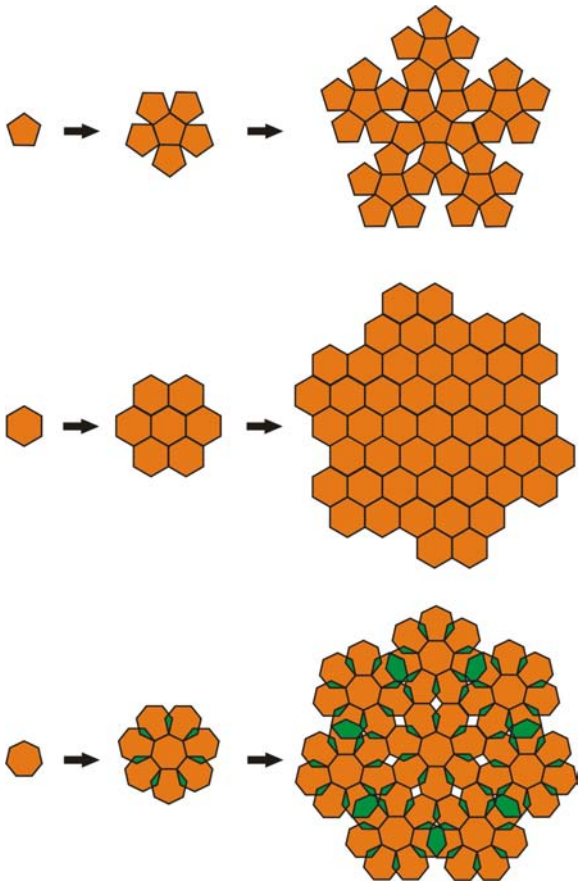

Figure 5.1: Construction of 5-, 6- or 7-fold tilings. Assembly of periodic and quasiperiodic tilings according to the method of polysynthetic twinning [112]. The construction principle consists in starting with a nucleus polygon and then iteratively adding others to the free edges. Pentagons lead to a tiling with quasiperiodic 5-fold local symmetry including gaps (white). From hexagons a periodic tiling without any gaps is obtained. For heptagons, the tiling contains both gaps (white) and nonuniform overlapping regions (green) leading to non-trivial steric hindrance problems when decorating the tiles with atoms.

and the Debye screening length were chosen such, that the colloids ($R = 1.45$ μm) form a liquid in the absence of the laser field. In case of the 5-beam pattern, the colloids follow the underlying potential already at quite small intensities as seen by the formation of local pentagons. At a laser intensity of about $I_0 = 2.82$ μWμm^{-2} the particle configuration almost perfectly resembles the underlying interference pattern.

In contrast, when exposing the colloidal system to a 7-beam pattern, the particles do only rarely form heptagons at the same intensity. Even at $I_0 = 5.08$ μWμm^{-2} (Fig. 5.3b) the particles do not equally respond to the pattern compared to Fig. 5.4b. To quantify this observation, in Fig. 5.5 we show the corresponding bond orientational order parameter normalized by the maximal value Ψ_m can achieve. It

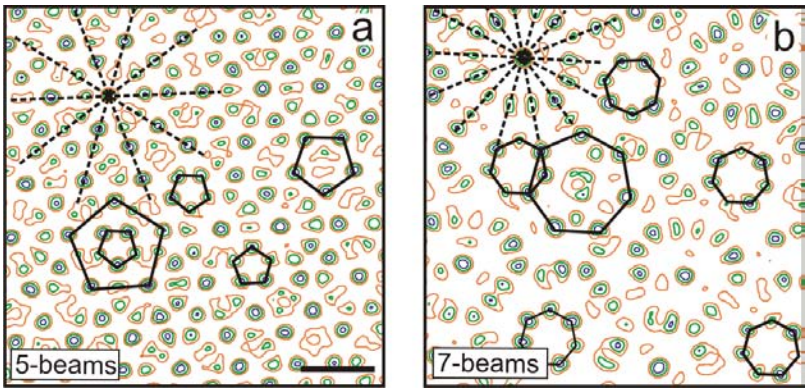

Figure 5.2: Contour plots of the intensity distribution of a 5-beam (a) and a 7-beam (b) pattern with characteristic length scale $a_v = 7.5$ μm. They exhibit characteristic motifs (shown as black solid lines), pentagonal in (a) and heptagonal in (b). The dashed lines correspond to the directions of the incident laser beams. The scale bare denotes 15 μm.

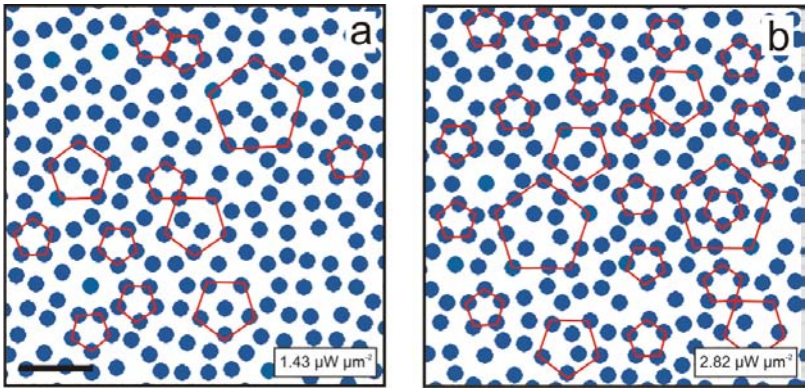

Figure 5.3: Colloidal monolayer subjected to a 5-beam interference pattern ($\phi = 0.028$ μm^{-2}), at different laser intensities. For higher intensities, the particles adapt the structure of pentagonal motifs (red). The scale bare denotes 15 μm.

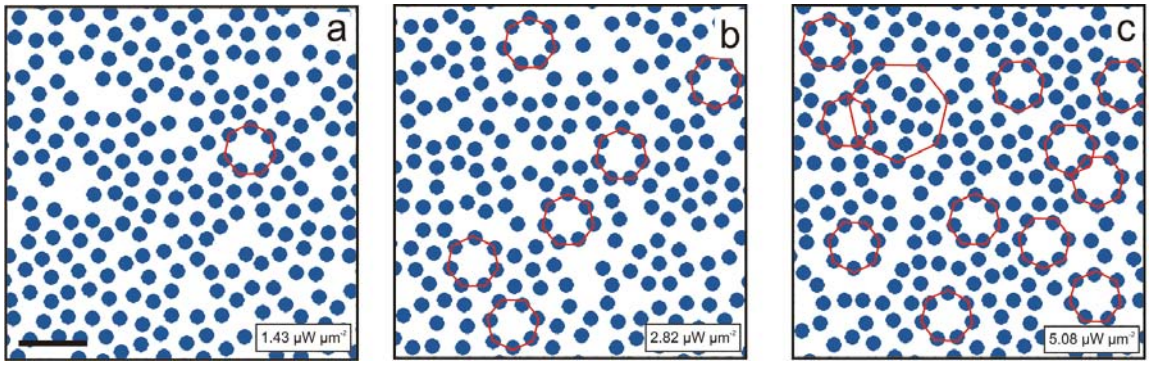

Figure 5.4: Same colloidal monolayer as in fig. 5.3 subjected to a 7-beam interference pattern, at different intensities. Only at very high intensities, the particles adapt the structure of heptagonal motifs (red). The scale bare denotes 15 μm.

is clearly seen that at $I_0 = 2.82\ \mu W \mu m^{-2}$ the particles on the 5 beam interference pattern have achieved almost 70% of the saturation value while in case of the 7 beam interference pattern even for the highest experimental intensity $I_0 = 5.08\ \mu W \mu m^{-2}$ only 40% of the corresponding maximum value were achieved. Similar results were obtained for other particle densities and Debye screening lengths. Obviously, quasicrystalline order induced by a quasiperiodic light potential of N=7 is only achieved at much higher potential strengths of the light field compared to N=5.

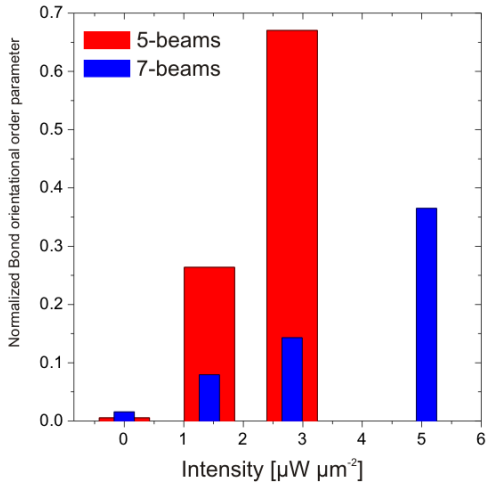

Figure 5.5: Comparison of the bond-orientational order parameter Ψ_m of the colloidal system on quasiperiodic patterns of 5 (m=10) and 7 (m=14) laser beams. Ψ_m is normalized by the maximal value it can achieve.

5.3 Phase transition from a periodic crystal to a tetradecagonal quasicrystal

To understand on a microscopic scale what prevents the colloidal particles to follow the 7 beam quasiperiodic pattern at small laser intensities, we increased their density and electrostatic interaction which results in the formation of large hexagonal colloidal domains in the absence of the laser field. Due to the well defined particle positions in a periodic crystal (compared to a liquid) this facilitates the analysis how the particles respond to a quasiperiodic potential landscape.

Fig. 5.6 shows typical particle snapshots showing how a colloidal crystal responds to a 7-beam pattern of increasing laser intensity. In order to highlight regions where the hexagonal order becomes destroyed due to the interaction of the particles with the quasiperiodic light field, we have applied a Delaunay triangulation (lines) and encoded the number of nearest neighbors with different colors (green=5, blue=6, red=7). With this representation one can easily identify regions where the initial

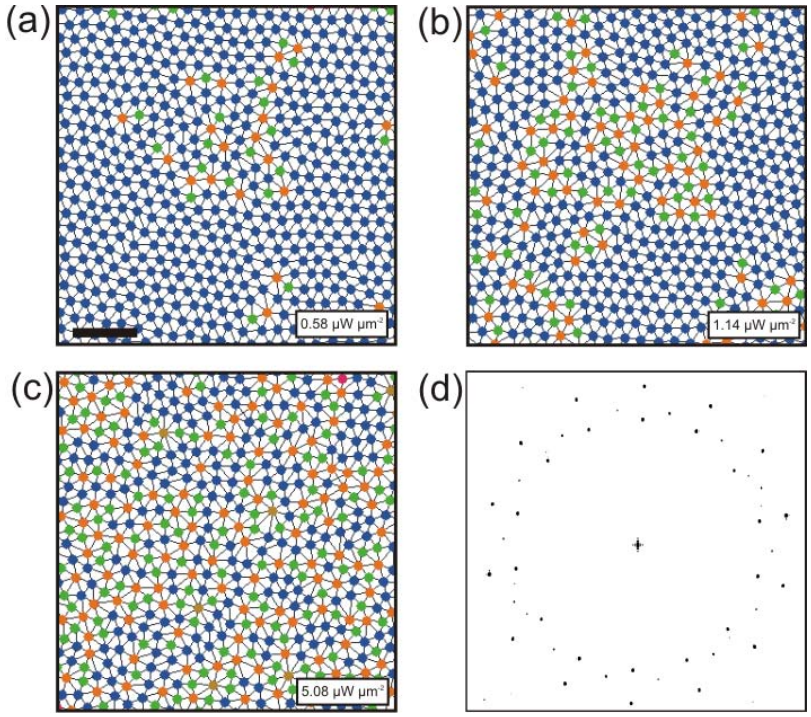

Figure 5.6: Phase transition from a periodic crystal to a quasicrystal on a 7-beam pattern. (a-c) Delaunay triangulation of typical particles configurations for a colloidal monolayer interacting with a 7-beam interference pattern of increasing intensity; $\phi = 0.033$ μm^{-2}, $a_v = 8.5$ μm. The particle coordination 5, 6, 7 is encoded in green, blue and red, respectively. The scale bar corresponds to 20 μm. (d) Two-dimensional structure factor calculated for the particle configuration in (c).

hexagonal structure of the particles becomes distorted by the underlying laser field. For $I_0 = 0$ the particles arrange in a single hexagonal domain with most of the particles having 6 nearest neighbors. Upon increasing I_0, the interaction with the quasiperiodic laser field leads to an increasing number of defects. Interestingly, these defects develop at rather localized regions (center of Fig. 5.6a and remain there during the entire measurement. Further increase of I_0 leads to a spatial extension of the defect area (Fig. 5.6b) until finally most of the particles lost their 6-fold coordination (Fig. 5.6c). In this situation, the particles almost perfectly follow the underlying quasiperiodic light field as seen by the 14-fold rotational symmetry of the corresponding structure factor (Fig. 5.6d).

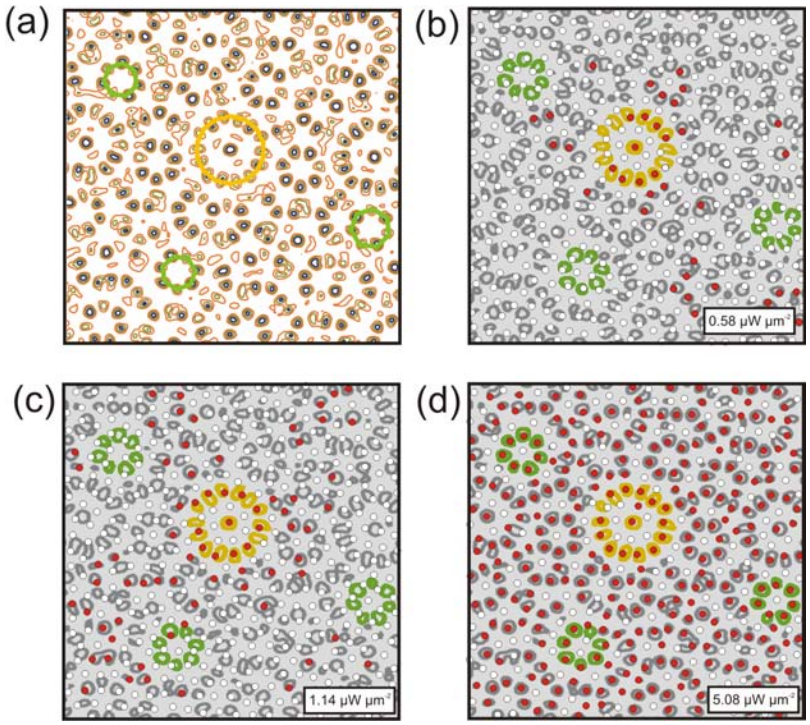

Figure 5.7: (a) Contour plot of the 7-beam light pattern with heptagons (green) and high symmetry stars (yellow). (b-d)Particle positions (taken from 5.6) superimposed to the light pattern (grey contour). Particles whose nearest neighbors are not 6-fold coordinated and overlap by more than 50% with an intensity maximum of the laser field are colored in red (white otherwise). The yellow and green patterns indicate distinct symmetric motifs in the laser pattern and are a guide to the eye.

To identify what determines the positions where the defects first occur, in Figs. 5.7b-d we superimposed the particle positions taken from Figs. 5.6a-c with the laser intensity distribution (light grey). In red we marked those colloids which most strongly respond to the quasiperiodic laser lattice, i.e. whose nearest neighbors lost their original 6-fold coordination and which overlap with quasiperiodic potential wells (all other particles are white). As seen from Fig. 5.7b, the particles which most

strongly respond to the interference pattern are those at so-called high symmetry stars (yellow) which correspond to local motifs in the laser lattice having the highest possible local rotational symmetry. High symmetry stars are comprised of a central potential well surrounded by 14 others. Since the potential wells are rather deep, they enforce a colloidal arrangement with quasiperiodic order. Upon further increasing I_0, quasicrystalline order laterally spreads around the high symmetry stars until almost all particles lost their 6-fold coordination and follow the quasicrystalline potential (Fig. 5.7a). From this we conclude, that the high symmetry stars of the laser pattern act as preferential adsorption sites where quasicrystalline order is initiated in the colloidal monolayer. Interestingly, the particles do not equally respond to the heptagonal motifs (green circles in Figs. b-d) of the laser pattern although their potential depths is similar to that of the high-symmetry stars. Obviously, the deep central potential wells of high symmetry stars (which are absent in the heptagons) plays an important role for the decoration of high symmetry stars with colloidal particles.

5.4 High symmetry stars density

After having identified high symmetry stars as nucleation sites of quasicrystalline order in the colloidal system, we expect that a high density of such stars should largely facilitate the extention of quasiperiodic order across the entire system. To demonstrate that this is indeed the case, we calculated the density of high symmetry stars for interference patterns created with $3 \leq n \leq 12$ laser beams. As shown in the chapter 3, high symmetry stars occur in any interference pattern created with n beams. They are not limited to 7-fold patterns but appear in any interference pattern of n laser beams. Fig. 5.8 illustrates such patterns of N=3, 5, 7, 8 laser beams together with the corresponding HSS. Depending on whether N is even or odd, they exhibit either N- or 2N-fold rotational symmetry.

Fig. 5.9a shows how the number density F of such stars varies with N. In our calculations, the number density of high symmetry stars F is determined by calculating the potentials that correspond to the intensity distribution of the laser fields and determining the fraction of local minima whose depths is at least 99 % of the deepest well. At a deep potential well the laser beams are almost in phase and therefore such a minimum is the center of a high symmetry star. Although the number density varies over several orders of magnitude depending on N, three regimes can be distinguished: for periodic laser patterns with N=3, 4 or 6 laser beams, F is of the order of 1 (i). For N=5, 8, 10 and 12, i.e. for laser fields with rank $\Delta = 4$, the value of F is about two orders of magnitude smaller (ii) and for N=7, 9, 11 (Δ=6) the density of high symmetry stars becomes smallest (iii). It is important to realize that all quasicrystalline symmetries in regime (ii) have been experimentally observed in atomic systems [116] while no single example of regime (iii) was ever found.

This systematic dependence of F reported in Fig. 5.9a does not only occur for interference patterns but is a general feature of quasiperiodic order. It is also found

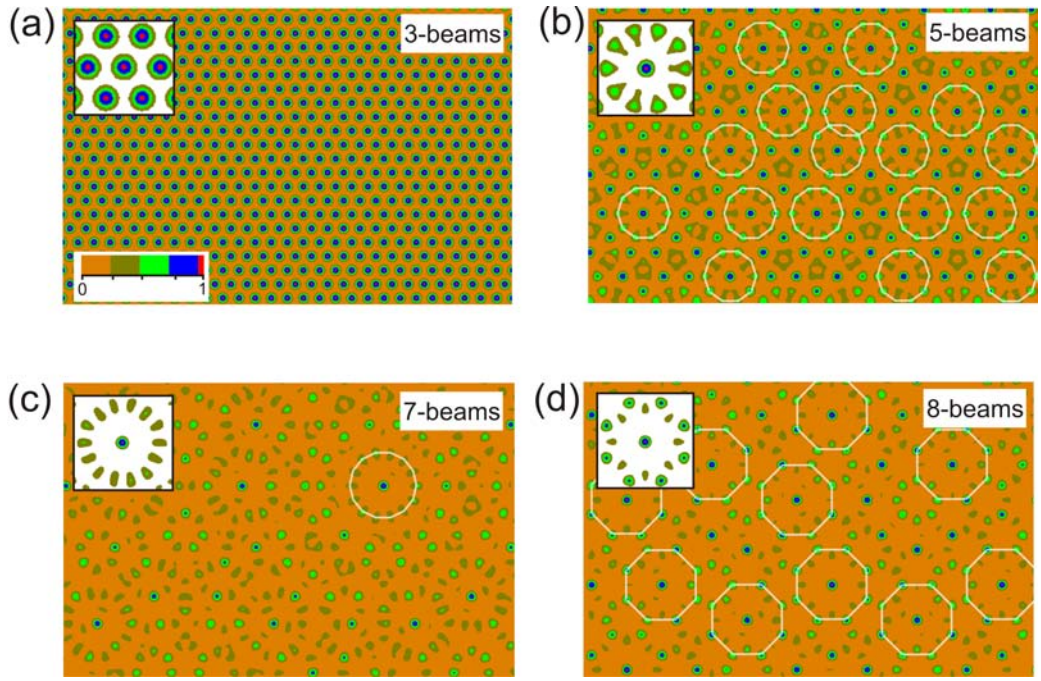

Figure 5.8: Calculated 3-, 5-, 7- and 8-beam patterns. The inset shows typical HSS for each pattern. The white polygons highlight the HSS. When potential wells are deeper than $V = 0.95V_0$ (V_0 being the deepest potential well), they are considered as centers of the stars. The hexagons in the case of the 3-beam pattern are not plotted.

in n-fold rhombic tiling based on the dualization of an n-fold grid [117]. They are constructed from n grids of parallel lines pointing along n symmetrically distributed directions and have the same rotational symmetry as an n-fold light pattern. The number density of HSS was calculated for rhombus tilings with up to 4×10^7 vertices by Johannes Roth (Fig. 5.9b). For n prime it is possible to estimate the frequency of HSS in the rhombus pattern analytically by the projection method which is completely equivalent to the dual-grid-method: The rhombus pattern is produced by projection from n to 2 dimensions. The acceptance domain is the complementary (n-2)-dimensional projection of a hypercube and contains the acceptance domain of the HSS at its center. The frequency of the HSS can be determined if we assume that both domains are similar (which is an underestimation, since the HSS domain is larger). The existence condition for the HSS and thus the similarity factor S is given as in [118]. Then the frequency of HSS is roughly S(n-2). Although the high-dimensional polytopes get exceedingly complex we have succeeded in checking the accurateness of the estimate by calculating the volumes and cross sections of the polytopes exactly up to n=7 and partially up to n=11. Despite quantitative variations compared to Fig. 5.9a, the differences between observed and not observed atomic quasicrystalline symmetries are obvious.

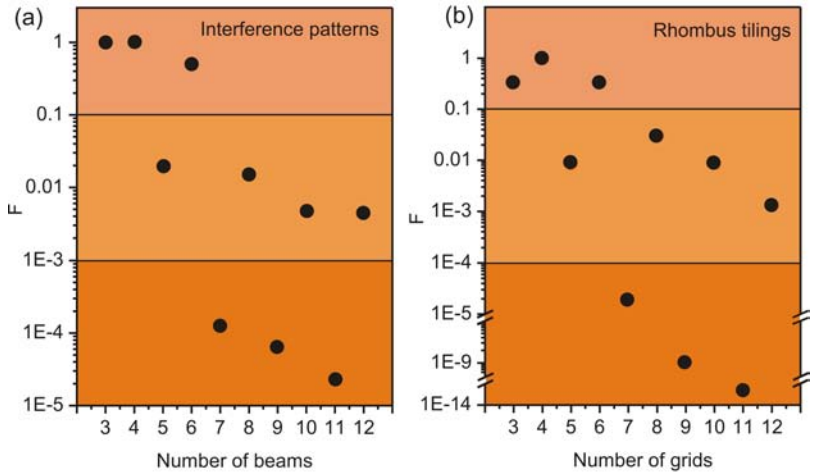

Figure 5.9: (a) Number density of high symmetry stars F calculated for n-beam patterns with $3 \leq n \leq 12$. The density of high symmetry stars is defined by the fraction of wells deeper than 99% of the deepest well. For 11-beam patterns the value provides an upper limit. (b) Same as (a), but calculated for rhombus tilings.

This remarkable coincidence cannot be accidental. It suggests that a similar argument, i.e. a deficiency of high symmetry motifs, may also explain why certain quasicrystalline symmetries are not observed in atomic systems. In contrast to crystals which are periodic in all three dimensions, quasiperiodicity is always (except for icosahedral quasicrystals) restricted to two dimensions [115]. Accordingly, three-dimensional quasicrystals are comprised of a periodic stacking of quasiperiodic layers and any hurdle in the formation of quasiperiodic order within a single layer will even-

tually prohibit their growth along the periodic direction. Indeed, strong evidence for the importance of symmetric motifs for the formation of quasiperiodic order in atomic systems has been recently obtained by scanning-tunneling microscopy studies and ab initio calculations [38, 119] where the structure of thin overlayers adsorbed on quasiperiodic surfaces was determined. Only for certain atoms, which do preferentially absorb on these motifs, extended thin films with quasiperiodic order have been observed.

5.5 Archimedean-like tiling phase on tetradecagonal lattices

In the previous chapter, we have shown that subjecting a crystalline monolayer to a laser pattern with decagonal symmetry can lead to the formation of an archimedean-like tiling phase where rows of squares and triangles are order aperiodically along one direction [101]. In this section, we show that a similarly ordered intermediate phase can also occur on laser patterns with tetradecagonal symmetry. When hexagonal monolayers, with densities, at which the colloid-substrate interaction is minimized, is subjected to a 7-beam pattern, a structure also consisting of alternating rows of squares and rows of triangles is found. In the following, we study the phase behavior of a colloidal system which is denser than the system in section 5.3 interacting with a tetradecagonal substrate potential. We investigate the structure of the occurring intermediate phase and show that, in contrast to the decagonal case, the ordering is rather periodic in both directions. We also show that this behavior is related to the low density of the high symmetry motifs.

In this experiment, polystyrene colloidal particles with radius $R = 1.45$ μm are used. The system is prepared so that the density is $\phi = 0.036$ μm^{-2}, i.e. 3500 particles homogeneously distributed in the field of view (the choice of this specific density will be explained later). In the absence of the quasiperiodic light potential, spontaneous crystallization is observed. The particles thus adapt a triangular structure with long range order and a mean particle distance $A = 5.39$ μm. The sample is later exposed to an interference pattern with characteristic length scale $a_v = 7.5$ μm thus $A/a_v = 0.72$. The laser intensity I_0 is stepwise increased with a time interval of 2000 seconds.

The change in the particle configuration upon increasing the laser power I_0 can be clearly seen in the change of the bond length histogram shown in Fig. 5.10. At low I_0, a sharp monomodal distribution with a peak located at the mean particle distance $A = 5.39$ μm is observed. This indicates a periodic crystalline phase characterized by one length scale, i.e. the particle mean average distance. By increasing the laser intensity, the peak slightly shifts to lower distances and simultaneously another peak starts to form at larger distances (green arrow). For $I_0 = 1.11$ μWμm^{-2} the distribution clearly becomes bimodal with the ratio of the two peak positions close to $\sqrt{2}$. The position of the first peak coincides well with the shortest length scale of the

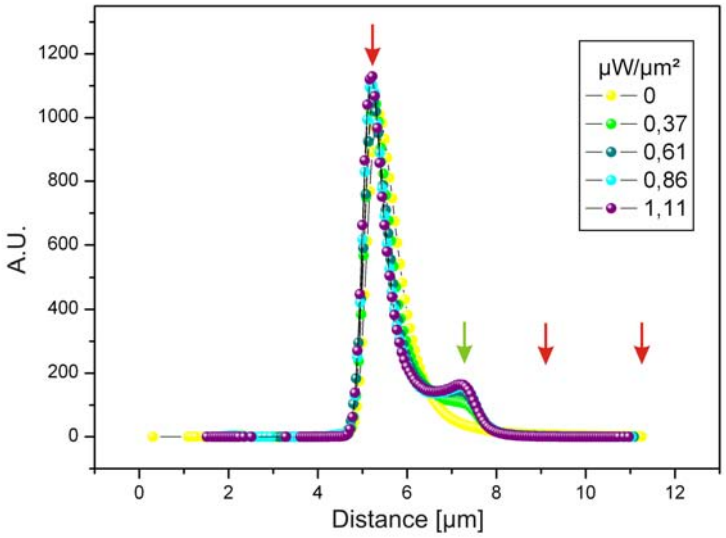

Figure 5.10: Bond-length histogram calculated for the particle configurations at different potential strength. The red arrows mark the positions of the pattern three length scales and the green arrow located at $A\sqrt{2}$ points at the peak corresponding to the diagonal of the square tiles.

underlying pattern (red arrow). Obviously, the colloid-substrate interaction is strong enough to overcome the colloid-colloid repulsion resulting in a shift in the position of the peak of about 230 nm. The second peak (green arrow), however, does not coincide with any of the larger length scales of the tetradecagonal pattern (red arrows). Since the bond length distribution depends sensitively on the structure of the different phases, and since a quasiperiodic order would lead to a three-modal distribution (3.6.3), one would expect that this distribution corresponds to an intermediate phase containing quadratic tiles. The fact that the ratio of the two peak positions is $(\sqrt{2})$ suggests the formation of quadratic tiles with a diagonal bond length equal to $A\sqrt{2}$.

To confirm the hypothesis of the occurrence of an intermediate phase, we construct the tiling of single snapshots taken at different laser intensities. Figure 5.11 shows how the colloidal monolayer changes when the substrate strength of the tetradecagonal substrate is increased. In absence of a substrate potential the system crystallizes (5.11a). The observed structure contains two triangular domains (green tiles) oriented along two directions having an angle of 85°. Apart from the defects along the domain wall, each vertex is surrounded by six triangular tiles forming a (3^6)-vertex type. When I_0 is increased to $I_0 = 0.37\ \mu\mathrm{W}\mu\mathrm{m}^{-2}$, the particles strongly interact with the surface potential, and the tiling of the colloidal system does not only consist of triangular tiles. The particle-substrate interaction is strong enough to create geometrical defects in the form of quadratic tiles (blue). The observed structure shows a coexistence between regions where the triangular ordering prevails (white contour)

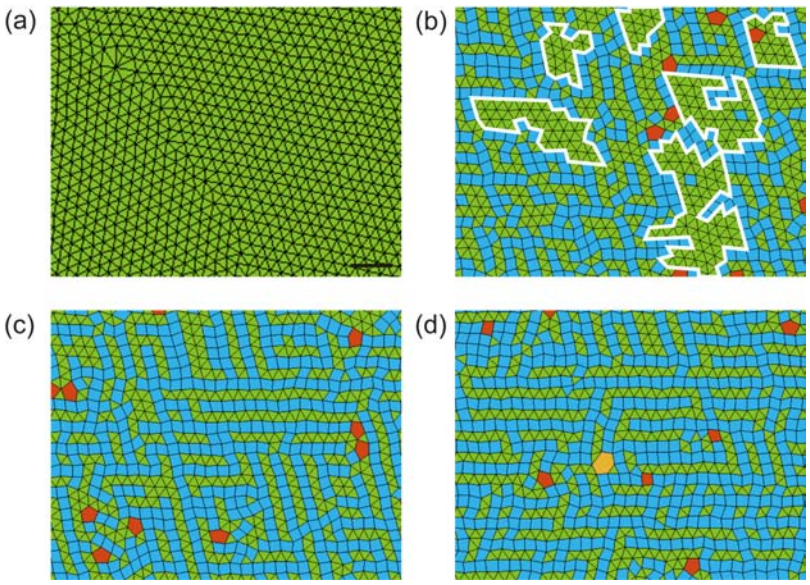

Figure 5.11: Real space structure of the adsorbate. Tiling of the phases for $I_0 = 0\ \mu W \mu m^{-2}$ (a) $I_0 = 0.37\ \mu W \mu m^{-2}$ (b) $I_0 = 0.61\ \mu W \mu m^{-2}$ (c) and $I_0 = 0.86\ \mu W \mu m^{-2}$ (d). The scale bar is 20 μm.

and regions with triangular and quadratic tiles. An increase of the laser intensity, $I_0 = 0.86\ \mu W \mu m^{-2}$, leads to a complete destruction of the triangular ordering and the formation of rows of quadratic tiles. These rows are mainly aligned along two directions making an angle of about 72°. The analysis of the static phason strain occurring in the underlying substrate (for details see 3.5.4) has also shown that these orientation match with the directions of the substrate with low density of jaggs.

The structure in Fig. 5.11d is almost identical with the archimedean-like tiling observed on decagonal substrates (as shown in 4.4). Exemplary, we show in Fig. 5.12a the ordering of 53 horizontally aligned rows of squares and rows of triangles. Except for few defects, the tiles in this situation mainly form a $(3^3.4^2)$-vertex type. Similar to the situation on the decagonal substrate, disruptions at larger length scales must occur. Indeed, as shown by two black arrows double square rows interrupt the periodic sequence of alternating rows of squares and rows of triangles. Accordingly, this phase consists of large periodic regions that correspond to a perfect archimedean tiling of type $(3^3.4^2)$ and the periodicity is only interrupted by a few double rows of squares. Fig. 5.12b shows a cut of the archimedean-like tiling phase observed on decagonal substrates. In contrast to Fig. 5.12a, the double triangular rows (black arrows) occur more often and lead to an aperiodic ordering perpendicular to the rows.

In order to understand why the interstial rows are of a different nature between the decagonal and the tetradecagonal cases, we next look at the position of the colloids on the different substrates. In Fig. 5.13 the substrate-adsorbate correlations are plotted for both tetradecagonal (a) and decagonal (b) substrate potentials. It can be clearly seen that the interstial rows occur at positions where high symmetry stars are present.

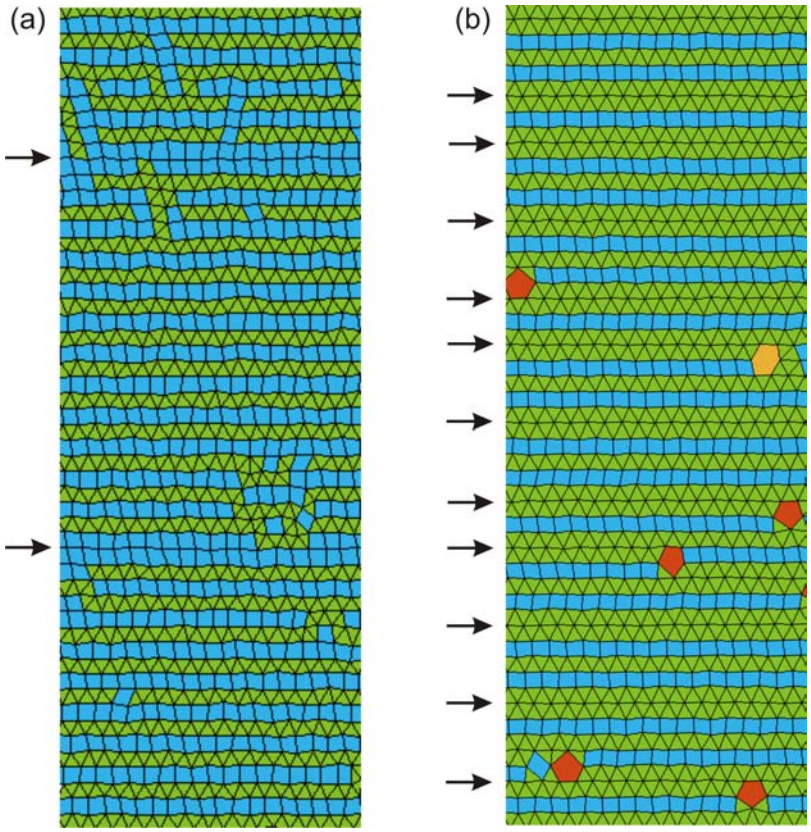

Figure 5.12: Comparison between archimedean-like tiling structures on tetradecagonal substrates ($I_0 = 0.86$ μWμm^{-2} and $A/a_v = 0.72$) (a) and decagonal substrates ($I_0 = 3$ μWμm^{-2} and $A/a_v = 0.62$) (b). The arrows point at disruptions that occur as additional interstitial rows of squares in (a) and triangles in (b).

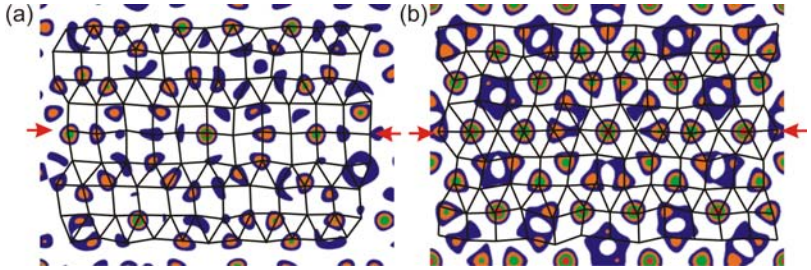

Figure 5.13: Substrate-adsorbate correlations. Tiling of both intermediate phases showing interstial rows superimposed on the laser intensity distributions. For the tetradecagonal case (a) the interstitial rows are double square rows and for the decagonal case (b) double trangular rows. The interstial rows occur at positions where high symmetry stars are present (red arrows).

Obviously, a double row of squares occurs at a 14-fold high symmetry star and a double triangular row at a 10-fold high symmetry star. Since in a tetradecagonal laser field local symmetry stars are rare (ref. 5.4), only few double rows of squares exist in the archimedean-like tiling structure. For the decagonal case, there are much more symmetry stars and subsequently much more double rows exist in the archimedean-like tiling phase of a decagonal substrate.

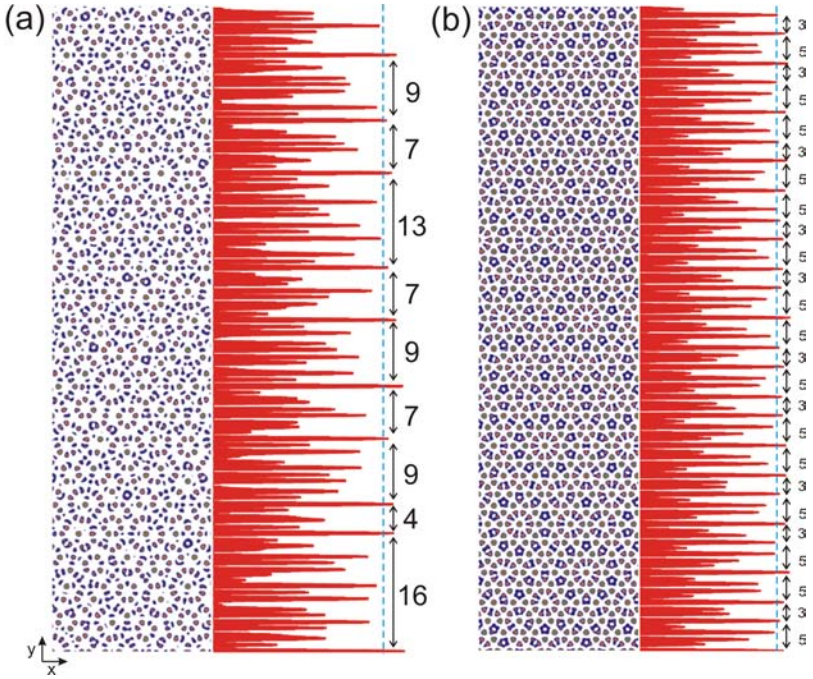

Figure 5.14: Calculated 7- and 5-beam, (a) and (b) respectively, interference patterns and a projection of the intensities along the x direction. In between the high peaks the number of square and triangle rows that can fit is indicated. The dashed blue line indicates the intensity threshold used to determine the highest peaks.

The spacing of those interstitial rows is illustrated in Fig. 5.14. For numerical 7- and 5-beam patterns, (a) and (b) respectively, we calculate the projection of the intensities along the x direction (in red). As stated before, the central intensity maximum of a high symmetry star is, compared to all other maxima, the highest. Accordingly, the spacing between the highest peaks in the intensity projection must be equal to the spacing between the interstial rows observed in the tiling of the colloidal particles. By choosing an appropriate threshold (dashed blue line), the highest peaks are selected and the number of rows fitting in between is calculated. In the case of the tetradecagonal pattern, a large number of rows, ranging from 4 to 16, can fit in between two peaks. For the decagonal pattern, only three or five rows are obtained. The sequence of these three and five rows is, as mentioned previously, a Fibonacci sequence reflecting on an intermediate length scale the long

range quasicrystalline order along one direction. This result is in good agreement with the experimental data.

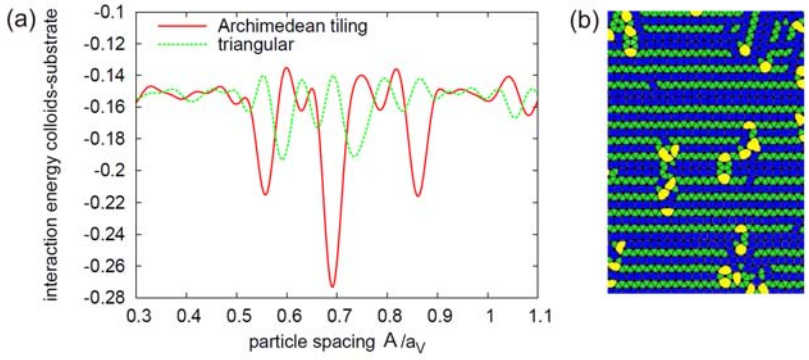

Figure 5.15: (a) Average potential energy of a colloid in the tetradecagonal potential calculated for a triangular and for an archimedean tiling structure as a function of density, which is given by the particle spacing A/a_V. (b) Archimedean-like tiling phases obtained by a Monte Carlo simulations induced by a tetradecagonal substrate. The figure shows a Delaunay triangulation of the colloidal coordinates where bonds longer than $1.1a_S$ are omitted. The potential strength is $V_0/(k_BT) = 20$ and the density is given by $A/a_V = 0.7$.

The densities, at which archimedean-like tilings occur under the influence of the tetradecagonal substrate potentials, are shown in Fig. 5.15a [104]. The calculated average potential energy of a colloid within an archimedean tiling structure as a function of the particle spacing A/a_v shows pronounced minima at $A/a_v = 0.557$, $A/a_v = 0.691$, and $A/a_v = 0.861$. The second minimum matches well with the experimental data. This proves, once again, that such intermediate phases occur at densities for which a high number of particles is located in a potential well and subsequently the average potential energy is minimized. Our experimental data were also reproduced by Monte Carlo simulations [104]. Fig. 5.15b shows the formation of an archimedean-like tiling phase on a tetradecagonal substrate with potential strength $V_0/(k_BT) = 20$ for a density equal to $A/a_V = 0.7$.

Interestingly, simulations using substrate potentials with other quasiperiodic symmetries also show similar phases. For example, on a 8-beam pattern rows of squares and triple or four-fold rows of triangles are observed [104]. A 10-beam pattern favors exactly the same structure as the decagonal potential created by 5-beams. For the case of eleven beams, characteristic rows of triangles and squares are also observed.

5.6 Conclusion

From our experiments we conclude that colloidal particles on quasicrystalline laser fields favor symmetries with rank $\Delta = 4$ compared to $\Delta = 6$. This behavior is attributed to large differences in the number of highly symmetric sites where quasicrystalline order first originates. The remarkable coincidence between the symmetries

with low density of high symmetry stars and the non-observed symmetries in atomic systems suggests that a similar argument, i.e. a deficiency of high symmetry motifs, may also explain why certain quasicrystalline symmetries are not observed in atomic systems. The importance of symmetric motifs for the formation of quasiperiodic order in atomic systems has been also recently reported by scanning-tunneling microscopy studies and ab initio calculations [38, 119] where the structure of thin overlayers adsorbed on quasiperiodic surfaces was determined. It should be emphasized, that geometrical considerations do not only play an important role for the growth of quasicrystals. Recent experiments demonstrate, that e.g. the electronic properties of Pb monolayers with quasiperiodic and periodic order are quite different [38]. In addition, the friction [23] or the lattice vibrations [24] also strongly depend on the quasiperiodic long range order.

By studying of the phase behavior of colloids on tetradecagonal substrates, we also find that intermediate archimedean-like tiling phases are not exclusive to decagonal substrate potentials. Similar phase also occur on tetradecagonal potentials. While the ordering perpendicular to the rows in the decagonal case is aperiodic, for the tetradecagonal case large periodic sequences interrupted by interstitial double rows of squares are observed. This behavior is also related to the low density of the high symmetry motifs.

CHAPTER 6

MICROMETER-SCALE QUASICRYSTALLINE MATERIALS

Because quasicrystals have higher point group symmetry than ordinary crystals, micrometer-scale quasicrystalline materials are expected to exhibit large and isotropic photonic bandgaps in the visible range [53, 100]. In this chapter, we report the fabrication of large colloidal quasiperiodic layers incorporated in a polymer hydrogel matrix. The quasiperiodic symmetries are induced using extended light fields. The present gelled colloidal quasicrystals are unique in that they have large sizes as well as good optical uniformity. With laser diffraction the in situ variable length scale of such materials is demonstrated. Also preliminary stacking experiments aiming to create three-dimensional structures are presented.

6.1 Introduction

Photonic crystals are materials with periodically repeating variations in refractive index [120]. An electromagnetic wave propagating inside these structures undergoes constructive or destructive interferences, depending on its frequency [121]. These effects lead to the appearance of allowed or forbidden frequency bands (stop-bands). Photons in the stop-band will not propagate in any dimension inside the photonic band gap (PBG) crystal. The ability of PBGs to control, reflect, or redirect light has powerful applications in photonics and optoelectronics [122].

Until recently, the only known materials with complete PBGs were photonic crystals comprised of a periodic arrangements of dielectric materials. One can define a Brillouin zone because of the periodicity; and a complete photonic gap (i.e., bandgaps for any propagation direction in the periodicity plane and for both polarizations) is formed when the spectral gaps at the Brillouin zone boundary overlap in all directions. The spatial arrangement of two-dimensional photonic crystals corresponds to one of the five two-dimensional Bravais lattices. Among these five lattices, the tri-

angular and honeycomb ones possess the highest order of rotational symmetry (six), and the Brillouin zone that is the closest to the circle. They exhibit the widest two-dimensional complete bandgaps [123]. Nevertheless, the band diagram of these lattices remains strongly dependent on the light propagation direction.

Because quasicrystals have higher point group symmetry than ordinary crystals, they are expected to have a complete bandgap that is more closely spherically symmetric [53]. In the search for structures with isotropic optical properties, photonic quasicrystals were studied both theoretically and experimentally [121, 120, 124]. For instance, quasicrystals with 8-, 10-, and 12-fold rotational symmetries were proposed [121]. These lattices present a higher order of local rotational symmetry than Bravais lattices. Their spectral properties are thus much less dependent on the propagation direction. Quasiperiodic symmetries facilitate the development of PBG for light propagating through quasicrystalline dielectric heterostructures, even when the dielectric contrast among the constituent materials is low.

Colloidal crystals, like photonic crystals, are composite materials with a spatial periodic distribution of micrometric building blocks. Because of their simplicity and scalability over a wide range of length scales, colloidal crystals are considered to be excellent photonic materials for the visible range. Quasiperiodic micrometer-scale materials have been realized in lithographically or holographically defined quasiperiodic structures [124, 125, 95]. Here we propose the use of colloids on extended quasiperiodic light fields in combination with hydrogel matrices. In contrast to other methods, here large materials with high optical uniformity can be fabricated.

6.2 Directed-assembly of polymerized quasicrystalline colloidal layers

Our approach is based on immobilizing colloidal particles, with high index of refraction, quasiperiodically arranged on large laser fields. We use melamine microspheres with carboxylic endgroup (MF-COOH-S1748, Microparticles GmbH Berlin). The melamine particles have according to the manufacturer a diameter of 3.27 μm, a density of $\rho_{MF} = 1.51$ g/cm^3, and a refractive index of $n_{MF} = 1.68$ much higher than the index of refraction of silica or polystyrene particles.

Figure 6.1 illustrates the preparation procedure. The particles are first dispersed in a aqueous solution of monomer-crosslinker and a UV-light-curable photoinitiator. As monomer and cross-linker we use a 40% (diluted to 30%) aqueous solution of acrylamide and N,N'-methylenebis(acrylamide) with a mass ratio of 19:1 (Carl Roth). As photoinitiator we use 2,2-diethoxyacetophenone (Sigma Aldrich). The mixture is later inserted in a home made cell consisting in two glass substrates and separated by a d=1mm silicon rubber spacer (Fig.6.1a). The sample cell is then inserted in the interferometer setup (described in chapter 3) and exposed to a quasiperiodic light field (decagonal or tetradecagonal) (Fig.6.1b). The laser intensity is gradually increased over 20 minutes which allows the particles to sample the whole pattern.

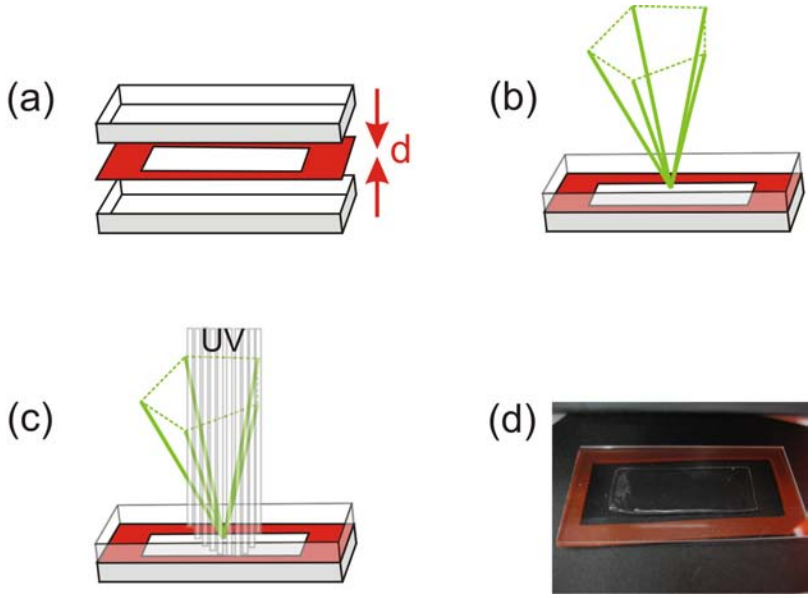

Figure 6.1: (a-c) Schematic drawings illustrating the preparation procedure of a two-dimensional polymerized colloidal quasicrystal. The description is in the text. (d) Picture of the resulting sample which contains the polymerized colloidal quasicrystal.

At very high laser power, $I_0 > 5\ \mu W \mu m^{-2}$, the particles are trapped in the deep potential wells. To cure the monomer and to polymerize the gel, the sample is then homogenously illuminated by a UV-light lamp (X-Cite 120Q, EXFO Mississauga) for several minutes (Fig.6.1c). The quasiperiodic colloidal crystal is then immobilized even when the quasiperiodic light field is turned off. The gelled quasicrystals could be removed from the cell as selfstanding materials. A continuous exposure to air results in dehydration of the sample, however they are long-time stable in closed vessels.

Figure 6.2 is a picture of the whole gelled quasicrystal. As the laser beam profiles are circular, the decagonal colloidal crystal is extended over a circular region (red lines) with a diameter of about 1.2 mm, i.e. includes about 40000 particles. In the outer region of the sample cell, the particles are immobilized but the structure has no long range order. Figure 6.3 shows snapshots taken from the sample after polymerization. The first (Fig. 6.3a) is taken from a region where the particles were not exposed to the light field and the second (Fig. 6.3b) from a region exposed to the light field. The difference in the structure can be clearly seen. In Fig. 6.3b the particles are arranged along the directions of the laser beams highlighted by the red lines.

A zoom in the above described images shows the ordering on the level of each particle. The $220 \times 176\ \mu m^2$ cuts in Fig. 6.3(c,d) are taken several months after the polymerization. They show that the quasiperiodic ordering is perfectly conserved. As highlighted by the red decagons and the blue pentagons, almost all the particles

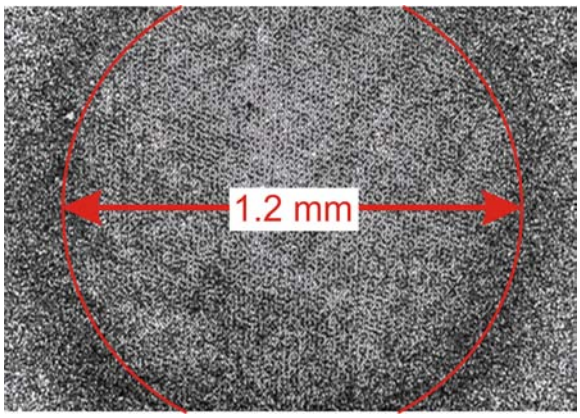

Figure 6.2: Snapshot of the system after polymerization. The red lines surround the region of the sample containing the quasiperiodic structure. It has a diameter of 1.2 mm and contains about 40000 particles. In the outer regions of the sample, the particles are also immobilized.

are located at potential wells. Subsequently, they locally adapt the structure of the pattern.

6.3 Laser diffraction from two-dimensional layers

The optical uniformity and high quality of the above described quasiperiodic material can be checked using laser diffraction. Figure 6.4(a,b) shows the visible diffraction pattern produced by a normally incident green He-Ne laser beam ($\lambda = 543$ nm) for tetradecagonal and decagonal fabricated quasicrystals. The observed Bragg peaks are sharp with several higher-harmonic peaks confirming the fabrication of a fully-fledged quasicrystal [54]. Each order has rings of peaks at different cone angles around the zero-order central peak which is blocked in order to make the higher-order peaks easily visible. The peaks show a 14- (a) and 10-fold (b) symmetry as expected. These pictures clearly show the presence of quasiperiodicity within the sample.

The quality of these diffraction patterns, in contrast to other micrometer-scale quasiperiodic structures as shown in Fig. 6.5 [126, 124, 95], is comparable to x-ray diffraction patterns obtained from decagonal or icosahedral metal alloys. In figure 6.4c, we show the 5-fold x-ray pattern of a natural quasiperiodic alloy of aluminum, copper, and iron ($Al_{65}Cu_{20}Fe_{15}$) [4]. A comparison of the 10-fold laser diffraction pattern (Fig. 6.4b) with the X-ray diffraction pattern from atomic quasicrystals (Fig. 6.4c) shows that both patterns are almost identical. The correspondence between the positions of the spots in the laser diffraction pattern with those in the x-ray pattern provide insight into the nature of the order in the atomic quasicrystal.

The colloidal quasicrystal fixed in the polyacrylamide hydrogel matrix is a highly elastic material. In order to demonstrate the in situ variable length scale of such materials we record the change in the 10-fold diffraction pattern while applying a mechanical deformation to the hydrogel. Figure 6.6 shows the in situ length scale

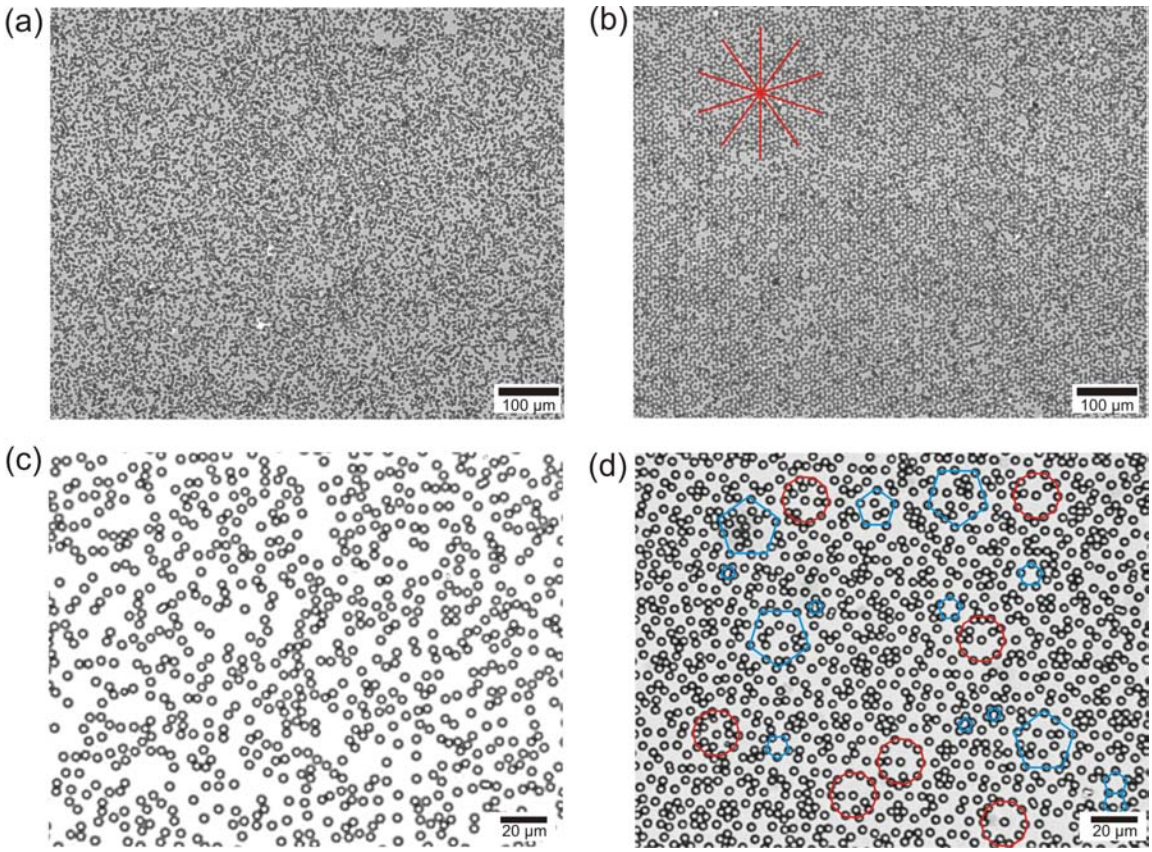

Figure 6.3: Snapshots taken from the polymerized sample. (a,b) 850×680 µm^2 cuts showing the fluid phase adapted by the particles in regions not exposed to the laser field (a) and the decagonal quasiperiodic phase where the particles were exposed to the laser field (b). The red lines indicate the directions of the laser beams. (c,d) 220×176 µm^2 cuts showing the local ordering of melamine particles with diameter 3.3 µm. (c) Fluid phase and (d) decagonal phase. The red decagons and blue pentagons highlight some of the main structural motifs also present in the underlying pattern.

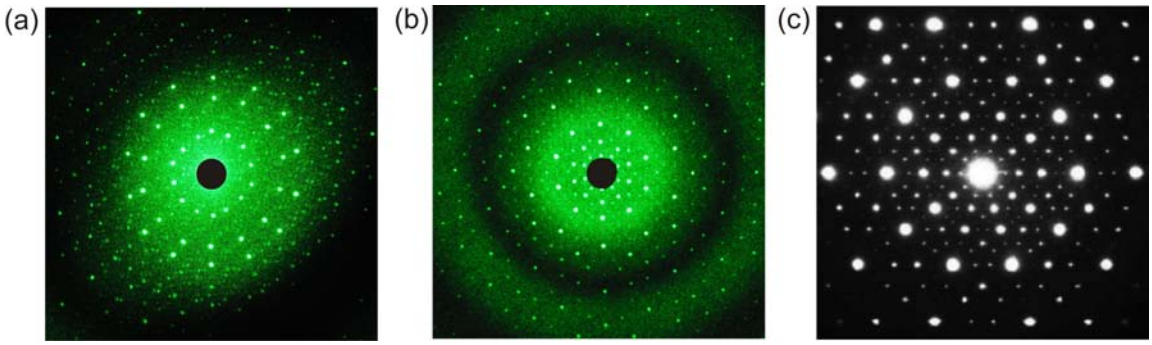

Figure 6.4: (a,b) Laser diffraction pattern obtained from the tetradecagonal (a) and decagonal (b) polymerized colloidal quasicrystals. (c) 5-fold X-ray diffraction pattern obtained from a icosagedral natural alloy of aluminum, copper, and iron [4].

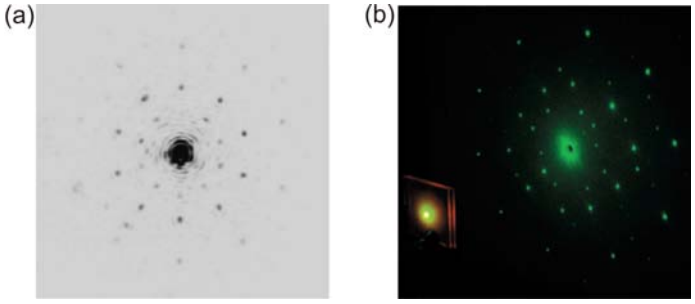

Figure 6.5: (a) Laser diffraction pattern showing 10-fold symmetric peaks obtained from a holographic assembly of 173 silica particles [124]. (b) Diffraction pattern using a green wavelength laser obtained from a quasicrystal structure fabricated in holographic polymer-dispersed liquid-crystal materials using a multibeam hololithography exposure technique [95].

variation in real and reciprocal space. The system shown in Fig. 6.6a is stretched to about 120% of its original size along the x direction. The circular quasiperiodic region thus becomes elliptical (Fig. 6.6b). The high intensity Bragg peaks are traced while applying the deformation and the resulting trajectories are plotted in Fig. 6.6c. As expected the deformation in real space is translated into a change in the position of the Bragg peaks in the reciprocal space. The trajectories path (evolving from red to green) shows that the Bragg peaks are displaced along the k_y direction.

6.4 Conclusion

Creating large quasiperiodically ordered arrays in the micrometer-scale is quite important especially for manipulating photons in the visible range. Here, we reported a different method to create such structures with long-range quasiperiodic order in two dimensions. Thousands of particles arranged quasiperiodically on extended light fields are immobilized using a polymerized hydrogel. The gelled colloidal quasi-

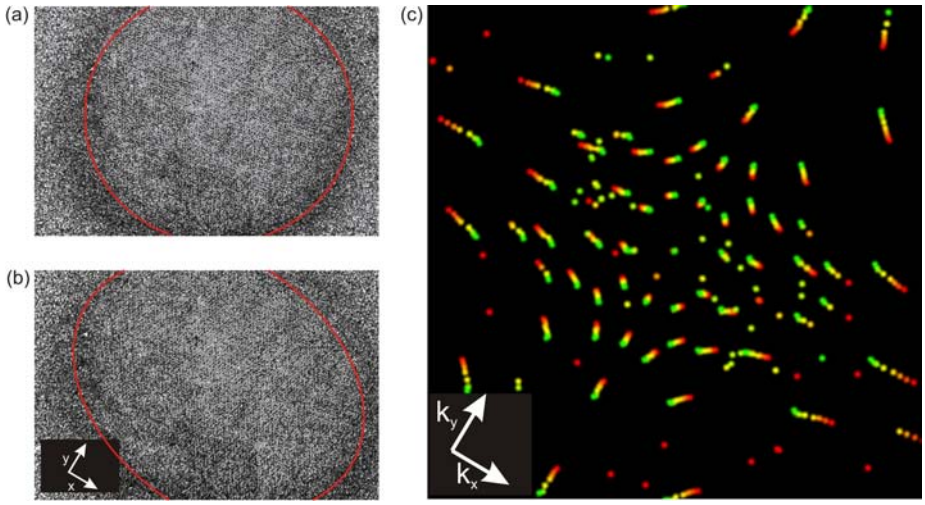

Figure 6.6: In situ length scale variation in real and reciprocal space. (a) Real space picture of the system. (b) After stretching, the quasiperiodic region of the sample becomes elliptical. (c) Trajectories (from red to green) of the Bragg peaks registered while stretching the hydrogel sample.

crystals are unique in that they have large sizes as well as good optical uniformity demonstrated in the high quality laser diffraction patterns. We also demonstrate the in situ variable length scale of such materials by applying a mechanical deformation to the sample and recording the change in the position of the Bragg peaks.

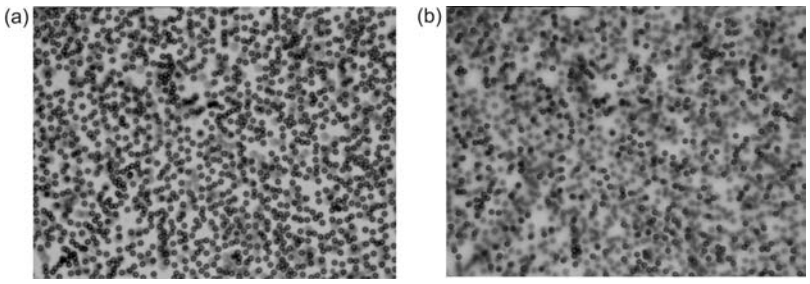

Figure 6.7: Snapshot showing the stacking of double quasiperiodic layers. The image is focused in (a) on the first layer and in (b) on the second.

Using this fabrication method three-dimensional structures can also be formed. Figure 6.7 shows preliminary experiments where a layer by layer assembly is applied. These preliminary results show that this is a promising route for creating novel photonic structures.

SUMMARY AND OUTLOOK

Quasicrystals provide a fascinating class of materials with partially unique properties. Compared to crystals, quasicrystalline surfaces exhibit much larger structural and chemical complexity leading e.g. to unusual frictional, catalytical or optical properties. Accordingly, deposition of thin films onto such substrates can lead to novel structures which may even exhibit typical quasicrystalline properties. Recent experiments indeed demonstrate 5-fold symmetries in the diffraction pattern of metallic layers adsorbed onto quasicrystals. In this Thesis we report on a real-space investigation of the phase behaviour of a colloidal monolayer interacting with a decagonal substrate created by interfering five laser beams. Different starting configurations, such as dense fluid and triangular crystals with different densities, are prepared. At low intensities and high particle densities, the electrostatic colloidal repulsion dominates over the colloid-substrate interaction and the crystalline structure remains mainly intact. As expected, at very high intensities the colloid-substrate interaction dominates and a quasiperiodic ordering is observed. Interestingly, at intermediate intensities we observe the alignment of crystalline domains along the 5 directions of the quasicrystalline substrate. This is in agreement with observations of Xenon atoms adsorbed on the ten-fold decagonal Al-Ni-Co surface and numerical simulations of weakly adsorbed atomic systems. Intermediate phases are observed for colloid-substrate interactions strong enough to produce defects in the crystal. These defects adapt the form of rows of quadratic tiles. Surprisingly, for specific particle densities (at which the colloid-substrate interaction is minimized) we identify a novel pseudomorphic phase which exhibits likewise crystalline and quasicrystalline structural properties. It can be described by an Archimedean-like tiling consisting of alternating rows of square and triangular tiles. The calculated diffraction pattern of this phase is in agreement with recent observations of copper adsorbed on icosahedral AlPdMn surfaces. In addition to establishing a link between Archimedean tilings and quasicrystals our experiments allow to investigate in real space how single-element monolayers can form commensurate structures on quasicrystalline surfaces.

In the second part of this Thesis the conditions under which quasicrystals form are investigated. Currently, it is not clear why most quasicrystals hold 5- or 10-fold

symmetry but no single example with 7 or 9-fold symmetry has ever been observed. Here, we report on geometrical constraints which impede the formation of quasicrystals with certain symmetries in a colloidal model system. Experimentally, this is achieved by subjecting a colloidal monolayer to two-dimensional quasiperiodic potential landscapes created by N = 5 and 7 laser beams. Our results clearly demonstrate that quasicrystalline order is much easier established for N = 5 compared to N = 7. With increasing laser intensity we observe that the colloids first adopt quasiperiodic order at local areas which then laterally grow until an extended quasicrystalline layer forms. As nucleation sites where quasiperiodicity originates, we identify highly symmetric motifs in the laser pattern. We find that their density strongly varies with n and surprisingly is smallest exactly for those quasicrystalline symmetries which have never been observed in atomic systems. Since such high symmetry motifs also exist in atomic quasicrystals where they act as preferential adsorption sites, this suggests that it is indeed the deficiency of such motifs which accounts for the absence of e.g. materials with 7-fold symmetry. In addition to the fundamental aspects, we also demonstrate that the combination of extended light fields and hydrogel matrices lead to the formation of quasiperiodically ordered colloidal materials. The reported gelled colloidal quasicrystals are unique in that they have large sizes as well as good optical uniformity. With laser diffraction we demonstrate the in situ variable length scale of such materials.

After having demonstrated that colloids on quasiperiodic light fields are a good model system, other apsects can be in the future investigated. This approach can be used to study the elastic properties of a two-dimensional colloidal quasicrystals. Similar studies on periodic systems have shown that the phonon band structure can be tuned depending on the symmetry and depth of the substrate potential. Subsequently, the investigation of quasiperiodic structures must be of high interest since there are no restrictions on the rotational symmetries. Our approach can also be extended to investigate dynamical processes on quasicrystalline surfaces. By introducing phase shifts between the interfering laser beams, phason modes can be induced in the substrate. Such elementary excitations are important for the three-dimensional growth of quasicrystals and it will be interesting to study how such substrate excitations modify the behaviour of adsorbed thin films. Also by introducing controlled phase shifts, long-wavelength phonon modes can be induced. Such modes lead to a continous translation of the laser pattern. This enables the study of friction on periodic and quasiperiodic substrates, and the investigation of collective sliding states as a function of substrate strength.

ACKNOWLEDGEMENT

This Thesis owes its very existence to the trust Prof. Clemens Bechinger put in me. He gave me much more than the opportunity to work on the project. The time he spent with me for discussions, the good suggestions, and the continuous support are invaluable. The interest he always had in my work highly motivated me. I should also thank him for teaching me how to write a good paper and make it accessible for broad audience. I couldn't have imagined a better place for my PhD years.

I'm highly indebted for the support of Dr. Laurent Helden. His help at the early stages of this Thesis provided a good basis. I also greatly profited from our discussions whenever I had new results.

A very special thanks to Sebastian Rausch, Günter Gera and Tobias Rybka. I am very grateful for having them working with me on different projects. I learned a lot with and from them. Their contributions brought a lot of advances.

It is a great pleasure to acknowledge Dr. Johannes Roth, Dr. Michael Schmiedeberg and Prof. Holger Stark, who at certain points boosted the theoretical work in order to understand better the experimental data.

I also thank Dr. Julian Ledieu who kindly answered many questions I had related to adsorbtion of atoms on quasiperiodic surfaces.

I am indebted to all those who helped by reading carefully parts or all the manuscript, especially Prof. Clemens Bechinger, Dr. laurent Helden, Thomas Bohlein, Dr. Alevtina Baskakova, Dr. Fadi Elhallak and Dr. Pedro Vidal.

I of course want to thank all the former and present group members for their help, support and valuable hints. I'm grateful for Uwe Rau and Denis Kobasevic who helped me solving many technical problems while building the setup. They were always there to offer their help.

I am deeply grateful to Mrs. Ulrike Offenbeck for her great efforts in handling the administrative issues throughout my stay at the institut. She was always of great help and support to me.

Of course I can not forget the wonderful team Fadi, Pedro, Pegor, and Arda. I am grateful that I got to know them all. I also thank Talal and all the Lebanese friends I met in Stuttgart.

Finally I will thank my beloved fiance Alevtina, my parents, and my brothers, who enriched my life and encouraged me every single morning, and supported me in every possible way they could. I dedicate this Thesis to my beloved mother.

BIBLIOGRAPHY

[1] J. Kepler. *Harmonices Mundi*. Am. Philos. Society, 1619.

[2] D. Shechtman, I. Blech, D. Gratias, and J. W. Cahn. Metallic phase with long-range orientational order and no translational symmetry. *Physical Review Letters*, 53:1951–1953, 1984.

[3] W. Steurer. Twenty years of structure research on quasicrystals. part 1. pentagonal, octagonal, decagonal and dodecagonal quasicrystals. *Zeitschrift Fur Kristallographie*, 219:391–446, 2004.

[4] L. Bindi, P. J. Steinhardt, N. Yao, and P. J. Lu. Natural quasicrystals. *Science*, 324:1306–1309, 2009.

[5] P. J. Lu and P. J. Steinhardt. Decagonal and quasi-crystalline tilings in medieval islamic architecture. *Science*, 315:1016–1110, 2007.

[6] Michael Baake. A guide to mathematical quasicrystals. *ArXiv Mathematical Physics e-prints*, 1999.

[7] M. Baake, D. Joseph, and M. Schlottmann. The root lattice d4 and planar quasi-lattices with octagonal and dodecagonal symmetry. *International Journal of Modern Physics B*, 5:1927–1953, 1991.

[8] J. Ledieu, R. McGrath, R. D. Diehl, T. A. Lograsso, D. W. Delaney, Z. Papadopolos, and G. Kasner. Tiling of the fivefold surface of al70pd21mn9. *Surface Science*, 492:L729–L734, 2001.

[9] J. Ledieu, A. W. Munz, T. M. Parker, R. McGrath, R. D. Diehl, D. W. Delaney, and T. A. Lograsso. Structural study of the five-fold surface of the al70pd21mn9 quasicrystal. *Surface Science*, 435:666–671, 1999.

[10] Stephan Weber. http://jcrystal.com/steffenweber/.

[11] E. J. W. Whittaker and R. M. Whittaker. Some generalized penrose patterns from projections of normal-dimensional lattices. *Acta Crystallographica Section A*, 44:105–112, 1988.

[12] R. P. A. Dullens and A. V. Petukhov. Second-type disorder in colloidal crystals. *Epl*, 77:–, 2007.

[13] B. Freedman, R. Lifshitz, J. W. Fleischer, and M. Segev. Phason dynamics in nonlinear photonic quasicrystals. *Nature Materials*, 6:776–781, 2007.

[14] P. Repetowicz and J. Wolny. Diffraction pattern calculations for a certain class of n-fold quasilattices. *Journal of Physics a-Mathematical and General*, 31:6873–6886, 1998.

[15] R. Lifshitz. What is a crystal? *Zeitschrift Fur Kristallographie*, 222:313–317, 2007.

[16] R. N. Bracewell. Numerical transforms. *Science*, 248:697–704, 1990.

[17] C. Janot. *Quasicrystals-A primer*. Oxford Univ. press, New York, 1994.

[18] H. R. Sharma, M. Shimoda, and A. P. Tsai. Quasicrystal surfaces: structure and growth of atomic overlayers. *Advances in Physics*, 56:403–464, 2007.

[19] A. P. Tsai, J. Q. Guo, E. Abe, H. Takakura, and T. J. Sato. Alloys - a stable binary quasicrystal. *Nature*, 408:537–538, 2000.

[20] T. M. Schaub, D. E. Burgler, H. J. Guntherodt, J. B. Suck, and M. Audier. The surface-structure of icosahedral al68pd23mn9 measured by stm and leed. *Applied Physics a-Materials Science and Processing*, 61:491–501, 1995.

[21] M. Krajci, J. Hafner, J. Ledieu, and R. McGrath. Surface vacancies at the fivefold icosahedral al-pd-mn quasicrystal surface: A comparison of ab initio calculated and experimental stm images. *Physical Review B*, 73:–, 2006.

[22] Andrew Zangwill. *Physics at surfaces*. Cambridge University press, 1988.

[23] J. Y. Park, D. F. Ogletree, M. Salmeron, R. A. Ribeiro, P. C. Canfield, C. J. Jenks, and P. A. Thiel. High frictional anisotropy of periodic and aperiodic directions on a quasicrystal surface. *Science*, 309:1354–1356, 2005.

[24] Marc de Boissieu, Sonia Francoual, Marek Mihalkovi, Kaoru Shibata, Alfred Q. R. Baron, Yvan Sidis, sutomu Ishimasa, Dongmei Wu, Thomas Lograsso, Louis-Pierre Regnault, Franz Gähler, Satoshi Tsutsui, Bernard Hennion, Pierre Bastie, Taku J. Sato, Hiroyuki Takakura, Roland Currat, and An-Pang Tsai. Lattice dynamics of the zn-mg-sc icosahedral quasicrystal and its zn-sc periodic 1/1 approximant. *Nature Materials*, 2007.

[25] J. V. Barth, G. Costantini, and K. Kern. Engineering atomic and molecular nanostructures at surfaces. *Nature*, 437:671–679, 2005.

[26] A. P. Tsai and M. Yoshimura. Highly active quasicrystalline al-cu-fe catalyst for steam reforming of methanol. *Applied Catalysis a-General*, 214:237–241, 2001.

[27] M. E. Zoorob, M. D. B. Charlton, G. J. Parker, J. J. Baumberg, and M. C. Netti. Complete photonic bandgaps in 12-fold symmetric quasicrystals. *Nature*, 404:740–743, 2000.

[28] H. Takakura, C. P. Gomez, A. Yamamoto, M. De Boissieu, and A. P. Tsai. Atomic structure of the binary icosahedral yb-cd quasicrystal. *Nature Materials*, 6:58–63, 2007.

[29] J. M. Dubois. Quasicrystals. *Journal of Physics-Condensed Matter*, 13:7753–7762, 2001.

[30] V. Fournee, T. C. Cai, A. R. Ross, T. A. Lograsso, J. W. Evans, and P. A. Thiel. Nucleation and growth of ag films on a quasicrystalline alpdmn surface. *Physical Review B*, 67:033406, 2003.

[31] S. Curtarolo, W. Setyawan, N. Ferralis, R. D. Diehl, and M. W. Cole. Evolution of topological order in xe films on a quasicrystal surface. *Physical Review Letters*, 95:136104, 2005.

[32] B. Bilki, M. Erbudak, M. Mungan, and Y. Weisskopf. Structure formation of a layer of adatoms on a quasicrystalline substrate: Molecular dynamics study. *Physical Review B*, 75:045437, 2007.

[33] L. Barbier, D. Le Floc'h, Y. Calvayrac, and D. Gratias. Identification of the atomic structure of the fivefold surface of an icosahedral al-pd-mn quasicrystal: Helium diffraction and scanning tunneling microscopy studies. *Physical Review Letters*, 88:085506, 2002.

[34] B. Bolliger, V. E. Dmitrienko, M. Erbudak, R. Luscher, H. U. Nissen, and A. R. Kortan. Epitactic textures of fcc al on icosahedral al-pd-mn quasicrystal. *Physical Review B*, 6305:052203, 2001.

[35] M. Shimoda, T. J. Sato, A. P. Tsai, and J. Q. Guo. Epitaxial crystalline film with psuedo-tenfold symmetry formed by au-deposition on a decagonal al72ni12co16 quasicrystal. *Physical Review B*, 62:11288–11291, 2000.

[36] N. Ferralis, R. D. Diehl, K. Pussi, M. Lindroos, I. Fisher, and C. J. Jenks. Low-energy electron diffraction study of xe adsorption on the ten-fold decagonal al-ni-co quasicrystal surface. *Physical Review B*, 69:–, 2004.

[37] M. Mungan, Y. Weisskopf, and M. Erbudak. Deposition of atoms on a quasicrystalline substrate: Molecular dynamics study in three dimensions. *Physical Review B*, 76:–, 2007.

[38] J. Ledieu, L. Leung, L. H. Wearing, R. McGrath, T. A. Lograsso, D. Wu, and V. Fournee. Self-assembly, structure, and electronic properties of a quasiperiodic lead monolayer. *Physical Review B*, 77:–, 2008.

[39] J. Ledieu, M. Krajci, J. Hafner, L. Leung, L. H. Wearing, R. McGrath, T. A. Lograsso, D. Wu, and V. Fournee. Nucleation of pb starfish clusters on the five-fold al-pd-mn quasicrystal surface. *Physical Review B*, 79:–, 2009.

[40] K. J. Franke, H. R. Sharma, W. Theis, P. Gille, P. Ebert, and K. H. Rieder. Quasicrystalline epitaxial single element monolayers on icosahedral al-pd-mn and decagonal al-ni-co quasicrystal surfaces. *Physical Review Letters*, 89:156104, 2002.

[41] H. R. Sharma, M. Shimoda, A. R. Ross, T. A. Lograsso, and A. P. Tsai. Real-space observation of quasicrystalline sn monolayer formed on the fivefold surface of icosahedral al-cu-fe quasicrystal. *Physical Review B*, 72:045428, 2005.

[42] J. Ledieu, J. T. Hoeft, D. E. Reid, J. A. Smerdon, R. D. Diehl, T. A. Lograsso, A. R. Ross, and R. McGrath. Pseudomorphic growth of a single element quasiperiodic ultrathin film on a quasicrystal substrate. *Physical Review Letters*, 92:135507, 2004.

[43] M. Krajci, J. Hafner, and M. Jahnatek. Ab initio study of quasiperiodic bi monolayers on a tenfold d-al-co-ni surface. *Physical Review B*, 73:–, 2006.

[44] J. Ledieu, P. Unsworth, T. A. Lograsso, A. R. Ross, and R. McGrath. Ordering of si atoms on the fivefold al-pd-mn quasicrystal surface. *Physical Review B*, 73:–, 2006.

[45] J. A. Smerdon, L. Leung, J. K. Parle, C. J. Jenks, R. McGrath, V. Fournee, and J. Ledieu. Formation of a quasicrystalline pb monolayer on the 10-fold surface of the decagonal al-ni-co quasicrystal. *Surface Science*, 602:2496–2501, 2008.

[46] K. Hayashida, T. Dotera, A. Takano, and Y. Matsushita. Polymeric quasicrystal: Mesoscopic quasicrystalline tiling in abc star polymers. *Physical Review Letters*, 98:195502, 2007.

[47] S. C. Glotzer and M. J. Solomon. Anisotropy of building blocks and their assembly into complex structures. *Nature Materials*, 6:557–562, 2007.

[48] X. B. Zeng, G. Ungar, Y. S. Liu, V. Percec, S. E. Dulcey, and J. K. Hobbs. Supramolecular dendritic liquid quasicrystals. *Nature*, 428:157–160, 2004.

[49] Dmitri V. Talapin, Elena V. Shevchenko, Maryna I. Bodnarchuk, Xingchen Ye, Jun Chen, and Christopher B. Murray. Quasicrystalline order in self-assembled binary nanoparticle superlattices. 461:964–967, 2009.

[50] T. Dotera and T. Gemma. Dodecagonal quasicrystal in a polymeric alloy. *Philosophical Magazine*, 86:1085–1091, 2006.

[51] R. Lifshitz and H. Diamant. Soft quasicrystals - why are they stable? *Philosophical Magazine*, 87:3021–3030, 2007.

[52] W. Steurer and D. Sutter-Widmer. Photonic and phononic quasicrystals. *Journal of Physics D-Applied Physics*, 40:R229–R247, 2007.

[53] W. N. Man, M. Megens, P. J. Steinhardt, and P. M. Chaikin. Experimental measurement of the photonic properties of icosahedral quasicrystals. *Nature*, 436:993–996, 2005.

[54] B. Freedman, G. Bartal, M. Segev, R. Lifshitz, D. N. Christodoulides, and J. W. Fleischer. Wave and defect dynamics in nonlinear photonic quasicrystals. *Nature*, 440:1166–1169, 2006.

[55] A. R. Denton and H. Löwen. Stability of colloidal quasicrystals. *Physical Review Letters*, 81:469–472, 1998.

[56] V. J. Anderson and H. N. W. Lekkerkerker. Insights into phase transition kinetics from colloid science. *Nature*, 416:811–815, 2002.

[57] M. Engel and H. R. Trebin. Self-assembly of monatomic complex crystals and quasicrystals with a double-well interaction potential. *Physical Review Letters*, 98:–, 2007.

[58] M. Engel and H. R. Trebin. Stability of the decagonal quasicrystal in the lennard-jones-gauss system. *Philosophical Magazine*, 88:1959–1965, 2008.

[59] D. A. Weitz and W. B. Russel. New developments in colloid science. *Mrs Bulletin*, 29:82–83, 2004.

[60] W. Poon. Colloids as big atoms. *Science*, 304:830–831, 2004.

[61] J. C. Crocker and D. G. Grier. Methods of digital video microscopy for colloidal studies. *Journal of Colloid and Interface Science*, 179:298–310, 1996.

[62] A. Yethiraj. Tunable colloids: control of colloidal phase transitions with tunable interactions. *Soft Matter*, 3:1099–1115, 2007.

[63] T. Sawetzki, S. Rahmouni, C. Bechinger, and D. W. M. Marr. In situ assembly of linked geometrically coupled microdevices. *Proceedings of the National Academy of Sciences of the United States of America*, 105:20141–20145, 2008.

[64] R. Tadmor. The london van der waals interaction energy between objects of various geometries. *J. Phys. Condens. Matter*, 13, 2000.

[65] J.N. Israelachvili. *Intermolecular and surface forces*. Academic Press, 2 edition, 1991.

[66] E. J. W. Verwey. Theory of the stability of lyophobic colloids. *Journal of Physical and Colloid Chemistry*, 51:631–636, 1947.

[67] J. Mikhael. *Depletion Forces in Binary Colloidal Systems*. Master thesis, 2005.

[68] J. Baumgartl, J. L. Arauz-Lara, and C. Bechinger. Like-charge attraction in confinement: myth or truth? *Soft Matter*, 2:631–635, 2006.

[69] J. Dobnikar, M. Brunner, H. H. von Grunberg, and C. Bechinger. Three-body interactions in colloidal systems. *Physical Review E*, 69:–, 2004.

[70] R. Klein, H. H. von Grunberg, C. Bechinger, M. Brunner, and V. Lobaskin. Macroion shielding and state-dependent pair potentials in colloidal suspensions. *Journal of Physics-Condensed Matter*, 14:7631–7648, 2002.

[71] A. Ashkin. Acceleration and trapping of particles by radiation pressure. *Physical Review Letters*, 24:156–, 1970.

[72] L. Guidoni, C. Triche, P. Verkerk, and G. Grynberg. Quasiperiodic optical lattices. *Physical Review Letters*, 79:3363–3366, 1997.

[73] L. Guidoni, B. Depret, A. di Stefano, and P. Verkerk. Atomic diffusion in an optical quasicrystal with five-fold symmetry. *Physical Review A*, 60:R4233–R4236, 1999.

[74] A. Ashkin. Forces of a single-beam gradient laser trap on a dielectric sphere in the ray optics regime. *Biophysical Journal*, 61:569–582, 1992.

[75] T. Tlusty, A. Meller, and R. Bar-Ziv. Optical gradient forces of strongly localized fields. *Physical Review Letters*, 81:1738–1741, 1998.

[76] J. Y. Walz and D. C. Prieve. Prediction and measurement of the optical trapping forces on a microscopic dielectric sphere. *Langmuir*, 8:3073–3082, 1992.

[77] Jm Kosterli and D. J. Thouless. Long-range order and metastability in 2-dimensional solids and superfluids. *Journal of Physics Part C Solid State Physics*, pages L124–+, 1972.

[78] B. I. Halperin and D. R. Nelson. Theory of 2-dimensional melting. *Physical Review Letters*, 41:121–124, 1978.

[79] N. D. Mermin. Crystalline order in two dimensions. *Physical Review*, 176:250 – 254, 1968.

[80] K. Zahn, R. Lenke, and G. Maret. Two-stage melting of paramagnetic colloidal crystals in two dimensions. *Physical Review Letters*, 82:2721–2724, 1999.

[81] A. H. Marcus and S. A. Rice. Observations of first-order liquid-to-hexatic and hexatic-to-solid phase transitions in a confined colloid suspension. *Physical Review Letters*, 77:2577–2580, 1996.

[82] Gasser, Maret, and Keim. Das schmelzen zweidimensionaler kristalle. *Phys. Unserer Zeit*, 2008.

[83] Boyer and falcom. Two-dimensional melting of a crystal of ferrofluid spikes. *Physical Review Letters*, 103:144501, 2009.

[84] M. Brunner and C. Bechinger. Phase behavior of colloidal molecular crystals on triangular light lattices. *Physical Review Letters*, 88:–, 2002.

[85] S. Bleil, H. H. von Grunberg, J. Dobnikar, R. Castaneda-Priego, and C. Bechinger. Strain-induced domain formation in two-dimensional colloidal systems. *Europhysics Letters*, 73:450–456, 2006.

[86] B. Grimm, H. Hovel, M. Pollmann, and B. Reihl. Physisorbed rare-gas monolayers: Evidence for domain-wall tilting. *Physical Review Letters*, 83:991–994, 1999.

[87] Michael Schmiedeberg, Johannes Roth, and Holger Stark. Freezing and melting of a colloidal adsorbate on a 1d quasicrystalline substrate. *Physical Review Letters*, 97:158304, 2006.

[88] T. Palberg, W. Hartl, U. Wittig, H. Versmold, M. Wurth, and E. Simnacher. Continuous deionization of latex suspensions. *Journal of Physical Chemistry*, 96:8180–8183, 1992.

[89] M. Brunner. *Effective Interactions and Phase Behavior of Colloidal Monolayers in the Presence of Light-Induced Substrate Potentials*. PhD thesis, 2003.

[90] M. Brunner, C. Bechinger, W. Strepp, V. Lobaskin, and H. H. von Grünberg. Density-dependent pair interactions in 2d colloidal suspensions. *Europhysics Letters*, 58:926–932, 2002.

[91] S. Duhr and D. Braun. Two-dimensional colloidal crystals formed by thermophoresis and convection. *Applied Physics Letters*, 86:–, 2005.

[92] M. Schmiedeberg. *Colloidal particles on quasicrystalline substrates*. PhD thesis, 2008.

[93] S. P. Gorkhali, G. P. Crawford, and J. Qi. Electrically switchable two-dimensional penrose quasi-crystal. *Molecular Crystals and Liquid Crystals*, 433:297–308, 2005.

[94] S. P. Gorkhali, J. Qi, and G. P. Crawford. Electrically switchable mesoscale penrose quasicrystal structure. *Applied Physics Letters*, 86:–, 2005.

[95] S. P. Gorkhali, J. Qi, and G. P. Crawford. Switchable quasi-crystal structures with five-, seven-, and ninefold symmetries. *Journal of the Optical Society of America B-Optical Physics*, 23:149–158, 2006.

[96] K. Niizeki. Self-similarity of quasilattices in two dimensions: Iii. inflation by a non-unit pv number. *Journal of Physics a-Mathematical and General*, 22:1859–1869, 1989.

[97] M. Schmiedeberg. *Private communications*. PhD thesis.

[98] N. Ferralis, A. W. Szmodis, and R. D. Diehl. Diffraction from one- and two-dimensional quasicrystalline gratings. *American Journal of Physics*, 72:1241–1246, 2004.

[99] P. Pearce. *Structure in Nature is a strategy for Design*. Cambridge MA:MIT Univ. Press, 1978.

[100] S. David, A. Chelnokov, and J. M. Lourtioz. Isotropic photonic structures: Archimedean-like tilings and quasi-crystals. *IEEE Journal of Quantum Electronics*, 37:1427–1434, 2001.

[101] J. Mikhael, J. Roth, L. Helden, and C. Bechinger. Archimedean-like tiling on decagonal quasicrystalline surfaces. *Nature*, 454:501–504, 2008.

[102] J. Ledieu, J. T. Hoeft, D. E. Reid, J. A. Smerdon, R. D. Diehl, N. Ferralis, T. A. Lograsso, A. R. Ross, and R. McGrath. Copper adsorption on the fivefold al70pd21mn9 quasicrystal surface. *Physical Review B*, 72:035420, 2005.

[103] N. V. Dziomkina and G. J. Vancso. Colloidal crystal assembly on topologically patterned templates. *Soft Matter*, 1:265–279, 2005.

[104] M. Schmiedeberg, J. Mikhael, S. Rausch, Johannes Roth, L. Helden, C. Bechinger, and H. Stark. Archimedean-like colloidal tilings on substrates with decagonal and tetradecagonal symmetry. *Submitted*, 2010.

[105] M. Schmiedeberg and H. Stark. Two-dimensional quasicrystals of decagonal order in one-component monolayer films - comment. *Physical Review Letters*, 1:–, 2008.

[106] A. S. Keys and S. C. Glotzer. How do quasicrystals grow? *Physical Review Letters*, 99:–, 2007.

[107] Paul J. Steinhardt. Solid-state physics: How does your quasicrystal grow? 452:43–44, 2008.

[108] U. Grimm and D. Joseph. *Quasicrystals: An Introduction to Structure, Physical Properties, and Applications*, volume Chapter Modelling Quasicrystal Growth. Springer, New York, 2002.

[109] Hyeong-Chai Jeong and Paul J. Steinhardt. Constructing penrose-like tilings from a single prototile and the implications for quasicrystals. *Physical Review B*, 55:3520 LP – 3532, 1997.

[110] V. Elser. Comment on "quasicrystals: A new class of ordered structures". *Physical Review Letters*, 54:1730 LP – 1730, 1985.

[111] W. Steurer. Boron-based quasicrystals with sevenfold symmetry. *Philosophical Magazine*, 87:2707–2712, 2007.

[112] W. Steurer. Reflections on symmetry and formation of axial quasicrystals. *Zeitschrift Fur Kristallographie*, 221:402–411, 2006.

[113] L. S. Levitov. Why only quadratic irrationalities are observed in quasi-crystals. *Europhysics Letters*, 6:517–522, 1988.

[114] E. Pelantova and R. Twarock. Tiles in quasicrystals with cubic irrationality. *Journal of Physics a-Mathematical and General*, 36:4091–4111, 2003.

[115] N. David Mermin, David A. Rabson, Daniel S. Rokhsar, and David C. Wright. Stacking quasicrystallographic lattices. *Physical Review B*, 41:10498 LP – 10502, 1990.

[116] Nicolas Stenger, Jean-Luc Rehspringer, and Charles Hirlimann. Template-directed self-organized silica beads on square and penrose-like patterns. *Journal of Luminescence*, 121:278–281, 2006.

[117] K. Niizeki. A classification of two-dimensional quasi-periodic tilings obtained with the grid method. *Journal of Physics a-Mathematical and General*, 21:3333–3345, 1988.

[118] E. Zobetz and A. Preisinger. Vertex frequencies in generalized penrose patterns. *Acta Crystallographica Section A*, 46:962–969, 1990.

[119] B. Unal, C. J. Jenks, and P. A. Thiel. Adsorption sites on icosahedral quasicrystal surfaces: dark stars and white flowers. *Journal of Physics-Condensed Matter*, 21:055009, 2009.

[120] Y. S. Chan, C. T. Chan, and Z. Y. Liu. Photonic band gaps in two dimensional photonic quasicrystals. *Physical Review Letters*, 80:956–959, 1998.

[121] M. Florescu, S. Torquato, and P. J. Steinhardt. Complete band gaps in two-dimensional photonic quasicrystals. *Physical Review B*, 80:–, 2009.

[122] H. Altug, D. Englund, and J. Vuckovic. Ultrafast photonic crystal nanocavity laser. *Nature Physics*, 2:484–488, 2006.

[123] M. Plihal and A. A. Maradudin. Photonic band-structure of 2-dimensional systems - the triangular lattice. *Physical Review B*, 44:8565–8571, 1991.

[124] Y. Roichman and D. G. Grier. Holographic assembly of quasicrystalline photonic heterostructures. *Optics Express*, 13:5434–5439, 2005.

[125] M. C. Guo, Z. D. Xu, and X. G. Wang. Photofabrication of two-dimensional quasi-crystal patterns on uv-curable molecular azo glass films. *Langmuir*, 24:2740–2745, 2008.

[126] A. Ledermann, L. Cademartiri, M. Hermatschweiler, C. Toninelli, G. A. Ozin, D. S. Wiersma, M. Wegener, and G. Von Freymann. Three-dimensional silicon inverse photonic quasicrystals for infrared wavelengths. *Nature Materials*, 5:942–945, 2006.